UNIVERSITY OF CALIFORNIA
SANTA CRUZ

INVESTIGATING REGULATORS OF FIDELITY DURING MEIOSIS AND MITOSIS

A dissertation submitted in partial satisfaction
of the requirements for the degree of

DOCTOR OF PHILOSOPHY

in

MOLECULAR, CELL AND DEVELOPMENTAL BIOLOGY

by

Anna E. Russo

March 2022

The Dissertation of Anna Russo is approved:

Professor Needhi Bhalla, chair

Professor Douglas Kellogg

Professor William Sullivan

Professor Jordan Ward

Peter Biehl
Vice Provost and Dean of Graduate Studies

Table of Contents:

List of Figures and Tables:

Abstract

INVESTIGATING REGULATORS OF FIDELITY DURING MEIOSIS AND MITOSIS

Anna Russo

All eukaryotic cells depend on faithful cell division to give rise to daughter cells that contain the correct number of chromosomes. Chromosome segregation errors during meiosis in germ cells can lead to aneuploid gametes, which can cause infertility, genetic disorders such as Down Syndrome and miscarriages. Additionally, chromosome segregation errors during mitosis can lead to aneuploid somatic cells, which are a hallmark of cancer. Despite the importance of tightly regulating these two types of cell division, the mechanisms that ensure fidelity during these processes remain active areas of investigation. Proteins that have been shown to be important regulators of fidelity during meiosis in *Caenorhabditis elegans (C. elegans)* include ZHP-3 and PCH-2. ZHP-3 is a putative SUMO or ubiquitin ligase required for crossover recombination, but whether or not ZHP-3 is regulated to promote recombination remains poorly understood. PCH-2 is a conserved AAA+ ATPase required for timely coordination of the meiotic prophase events pairing, synapsis and recombination, but the mechanism for how it accomplishes this coordination is currently unknown. Additionally, PCH-2 has been shown to be required for both silencing and activation of the spindle assembly checkpoint during mitosis, but how it regulates the checkpoint is still an active area of investigation. Here, I use *C. elegans* as a model system to investigate the molecular mechanisms of these two proteins

during meiotic and mitotic chromosome segregation. In Chapter 1, I investigate whether ZHP-3 is phosphorylated by a conserved DNA damage kinase, CHK-1, to determine if this phosphorylation event is required for ZHP-3's localization or function during meiosis. I find that while ZHP-3 is phosphorylated by CHK-1 kinase *in vitro*, mutation of these phosphorylation sites *in vivo* does not affect ZHP-3's localization to meiotic chromosomes, or its function in promoting crossover recombination. In Chapter 2, I investigate a different regulator of meiosis, PCH-2, to determine how it coordinates meiotic prophase events and whether it acts on meiotic HORMADS to accomplish this. I find that mutations in PCH-2 genetically interact with mutations in the meiotic HORMADS HTP-3 and HIM-3, suggesting that these proteins work together to coordinate meiotic prophase events. Additionally, I find that PCH-2 acts on HTP-3 to coordinate pairing and synapsis, but acts on HIM-3 during recombination, indicating that the meiotic HORMADS are cleanly delegated to regulate specific meiotic prophase events. Finally, in Chapter 3, I explore PCH-2's role during somatic cell division and investigate how PCH-2 regulates the strength of the spindle assembly checkpoint. I find that PCH-2 is more enriched in P1 cells compared to AB cells in the early *C. elegans* embryo, potentially explaining why cells that give rise to the germline have stronger checkpoints than somatic cells. Additionally, we find that this enrichment depends on cell fate factors and PCH-2's adaptor protein CMT-1. Taken together, these results contribute mechanistic insight for how these proteins promote fidelity during meiosis and mitosis by determining post-translational modifications of meiotic recombination factors (Chapter 1),

identifying potential substrates of meiotic prophase regulators (Chapter 2), and demonstrating how spindle checkpoint regulators are differentially inherited in specific cell types to give rise to differences in spindle checkpoint strength (Chapter 3).

Dedication and Acknowledgements

I would first like to thank Dr. Needhi Bhalla for advocating and supporting my scientific career since I was an undergrad. I would also like to thank her for her fantastic mentorship throughout graduate school and for her unwavering commitment toward my development as an independent scientist. I would like to thank the members of my thesis committee, Dr. Douglas Kellogg, Dr. William Sullivan, and Dr. Jordan Ward, for their insight and support throughout my graduate career. I would like to thank the Bhalla lab for their support, and would like to especially thank Dr. Alice Devigne, for not just being a labmate but also a great friend. I would also like to thank Dr. Christian Nelson and Dr. Lenaig Defachelles for their mentorship on the ZHP-3 and PCH-2 mitosis projects. I would like to thank my undergrads Valery Ortiz and Malaika Menon for all their hard work on the PCH-2 meiosis project and for helping me grow as a mentor. I would like to thank my lifelong friends Dr. Karen Ruiz and Dr. Miranda Stratton for their advice throughout graduate school and for being my role models. I would like to thank my graduate school friends, especially Dr. Apple Cortez Vollmers, Laura Chappell, Dr. Akshi Jasani, and Dr. Amanda Brambilla for being amazing friends and for all the fun memories outside of lab. I would like to thank my mom, dad, and my brothers Jon and Joe for always supporting my dreams and being there for me. Lastly, I want to thank my partner Brandt Warecki for his support, wisdom, advice, and for being my inspiration as a scientist.

The text of this dissertation includes reprints of the following previously published material: Russo A.E., Nelson C.R., Bhalla N. (2021). Mutating two putative phosphorylation sites on ZHP-3 does not affect its localization or function during meiotic chromosome segregation. microPublication Biology. doi: 10.17912/micropub.biology.000354 and Defachelles, L., Russo A.E., Nelson C.R., Bhalla N. (2020) The conserved AAA-ATPase PCH-2 ^{TRIP13} regulates spindle checkpoint strength. Mol Biol Cell. 2020 Sep 15;31(20):2219-2233. The co-author (Needhi Bhalla) listed in these publications directed and supervised the research which forms the basis for the dissertation.

CHAPTER 1: Mutating two putative phosphorylation sites on ZHP-3 does not affect its localization or function during meiotic chromosome segregation

Abstract

Meiotic chromosome segregation depends on crossover recombination to link homologous chromosomes together and promote accurate segregation in the first meiotic division. In *Caenorhabditis elegans*, a conserved RING finger protein, ZHP-3, is essential for meiotic recombination and localizes to sites of crossover formation. Whether ZHP-3 is regulated to promote recombination remains poorly understood. In vitro analysis identified two putative CHK-1 kinase phosphorylation sites on ZHP-3. However, mutation of the phosphorylation sites identified in vitro had no effect on meiotic recombination or localization of ZHP-3. Thus, these two phosphorylation sites appear to be dispensable for meiotic recombination or ZHP-3 function.

Introduction

Haploid sex cells such as sperm and eggs depend on a specialized form of cell division called meiosis. Throughout prophase of meiosis, homologous chromosomes pair, synapse, and recombine to form a physical link between them called a chiasma. Chiasmata are essential for proper segregation (Page and Hawley, 2003). Defects in meiotic recombination can lead to gametes that contain an incorrect number of chromosomes (aneuploidy), which can cause infertility, miscarriages, and genetic

disorders such as Down Syndrome. Therefore, identifying how recombination is regulated is crucial for understanding multiple aspects of human reproductive health.

Previous research in *C. elegans* has shown that several proteins called crossover factors localize to the designated crossover site to promote recombination (Bhalla et al., 2008) (Yokoo et al., 2012). One of these crossover factors, ZHP-3 (Zip homologous protein 3), is highly conserved, has a budding yeast counterpart that acts as a SUMO ligase (Cheng et al., 2006) and is essential for crossover formation (Jantsch et al., 2004). Therefore, when ZHP-3 is absent, chromosome pairs are not linked by chiasmata. Because sex determination in *C. elegans* is based on the number of X chromosomes, with hermaphrodites having two X chromosomes while males have one, a high incidence of male (HIM) phenotype is diagnostic for chromosome segregation errors. Loss of ZHP-3 results in a high rate of embryonic lethality and a HIM phenotype (Jantsch *et al.*, 2004), both indicating chromosome segregation errors. We've shown that ZHP-3's localization is dynamic throughout prophase: in mid-pachytene ZHP-3 is found all along the synaptonemal complex (SC) between synapsed homologous chromosomes. During late pachytene, it re-localizes and concentrates at the crossover site (Bhalla *et al.*, 2008). How ZHP-3 achieves this dynamic localization to promote meiotic recombination is currently unknown.

Meiotic proteins are phosphorylated to promote essential steps in meiotic prophase, including stabilizing the SC (Nadarajan et al., 2017), designating the short arm of chromosome pairs to promote two step cohesion loss (Sato-Carlton et al., 2018), and

activating negative feedback loops in response to defects in synapsis or crossover formation (Kim et al., 2015). CHK-1 (Checkpoint Kinase 1) localizes to early and mid-pachytene nuclei (Woglar et al., 2013), correlating with when ZHP-3 is present along the SC. Similar to SC proteins that are known to be phosphorylated (Nadarajan *et al.*, 2017) (Sato-Carlton *et al.*, 2018), ZHP-3 also contains an unstructured C-terminal tail containing multiple serine residues (Reynolds et al., 2013). Here we test whether CHK-1 is a potential regulator of ZHP-3's localization and if phosphorylation of two residues on ZHP-3 are required for its dynamic localization and/or to promote crossover formation.

Results

Mutating two putative phosphorylation sites on ZHP-3 does not affect its localization or function

To determine if ZHP-3 is post-translationally modified, we generated truncated versions of ZHP-3 protein, purified these from BL21 codon plus cells, and performed *in vitro* kinase assays with radiolabeled P^{32} and human Chk1 to determine if ZHP-3 is phosphorylated. We found that when ZHP-3 samples were incubated with human Chk1 and P^{32}, ZHP-3 is robustly phosphorylated on its C-terminus but not its N-terminus (Figure 1A). To identify the phosphorylated residues on ZHP-3, we sent samples for mass spectrometry and identified serine 308 and serine 366 as the phosphorylated residues (Figure 1A).

Figure 1. Mutating two putative phosphorylation sites on ZHP-3 does not affect its localization or function.

A. Top: Cartoon depicting the protein structure of ZHP-3 with phosphorylated residues indicated. RFM indicates the ring finger motif. Bottom: Gel stained with Coomassie blue and autoradiograph of *in vitro* kinase assays with N- and C-terminal regions of ZHP-3 and human Chk1. **B.** Mid pachytene nuclei stained with ZHP-3 (green) and SYP-1 (magenta) antibodies in wildtype germlines and *zhp-3(jf61)* null, *zhp-3*^{S308A}, *zhp-3*^{S366A}, and *zhp-3*$^{S308A, S366A}$ mutant germlines. **C.** Late pachytene nuclei stained with ZHP-3 (green) and SYP-1 (magenta) antibodies in wildtype germlines and *zhp-3(jf61)* null, *zhp-3*^{S308A}, *zhp-3*^{S366A}, and *zhp-3*$^{S308A, S366A}$ mutant germlines. **D.** Quantification of average number of DAPI bodies in wildtype oocytes and *zhp-3(jf61)* null, *zhp-3*^{S308A}, *zhp-3*^{S366A}, and *zhp-3*$^{S308A, S366A}$ oocytes. **E.** Bivalents stained with DAPI and antibodies against HTP-3 (magenta) and HTP-1 (green) in wildtype oocytes and *zhp-3(jf61)* null, *zhp-3*^{S308A}, *zhp-3*^{S366A}, and *zhp-3*$^{S308A, S366A}$ mutant oocytes. **F.** Quantification of embryonic viability and total number of male progeny in wildtype, *zhp-3(jf61)* null, *zhp-3*^{S308A}, *zhp-3*^{S366A}, and *zhp-3*$^{S308A, S366A}$ mutants. All scale bars indicate 5 microns. Significance was assessed using two sided Wilcoxon-Mann Whitney tests.

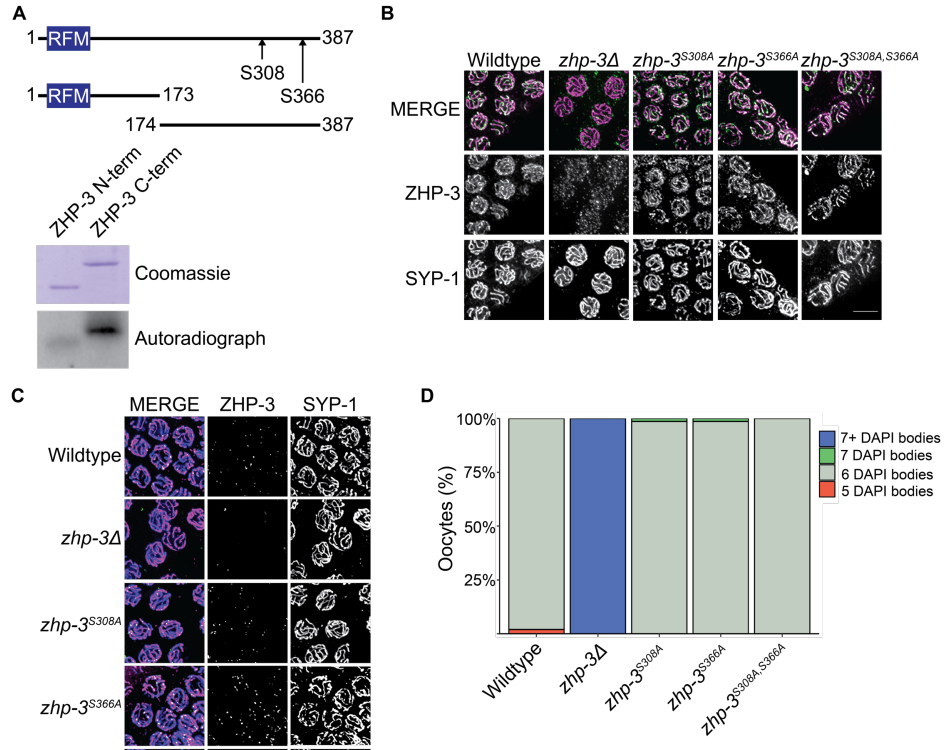

F

Genotype	Embryonic viability (total # progeny)	Percent males
Wildtype (N2)	100% (2685)	0.1%
zhp-3Δ	2.5% (2655)	47%
zhp-3^{S308A}	100% (2880)	0.03%
zhp-3^{S366A}	100% (2674)	0.2%
zhp-3^{S308A,S366A}	100% (3401)	0.1%

To determine the significance of these phosphorylation events on ZHP-3's function and meiotic recombination *in vivo*, we used CRISPR/Cas9 genome editing (Arribere et al., 2014) (Paix et al., 2015) to mutate serines 308 and 366 to alanines (*zhp-3*^{S308A} and *zhp-3*^{S366A}) so that they can no longer undergo phosphorylation. Along with generating the single phosphorylation mutant strains, we also created the double phosphorylation mutant (*zhp-3*^{S308A,S366A}) to test for redundancy between these two sites.

To determine if these mutations result in defects in ZHP-3's localization, we first stained mid-pachytene nuclei with antibodies against ZHP-3 and SYP-1 to determine if ZHP-3 phosphorylation mutants can still localize along the SC. In wildtype germlines, ZHP-3 is found all along the SC and colocalizes with SYP-1 (Bhalla *et al.*, 2008) (Figure 1B). We found that ZHP-3^{S308A}, ZHP-3^{S366A} and ZHP-3^{S308A,S366A} colocalized with SYP-1 on the SC (Figure 1B), similar to wildtype ZHP-3, indicating that these mutations do not affect ZHP-3's ability to localize to the SC.

To determine if ZHP-3's localization is affected in late pachytene, we tested whether ZHP-3^{S308A}, ZHP-3^{S366A}, and ZHP-3$^{S308A, S366A}$ can still properly localize to crossovers. We found that ZHP-3^{S308A}, ZHP-3^{S366A}, and ZHP-3$^{S308A, S366A}$ localized in distinct foci on chromosomes (Figure 1C), similar to wildtype ZHP-3, indicating that the single and double phosphorylation mutations do not affect ZHP-3's ability to localize to crossovers.

To determine if mutation of these phosphorylation sites results in defects in recombination or chromosome morphology, we quantified the number of DAPI stained bodies in oocytes. Wildtype oocytes contain 6 DAPI stained bodies, corresponding to 6 chromosome pairs (bivalents) held together by chiasmata (Dernburg et al., 1998). Recombination is lost in *zhp-3(jf61)* null mutants, resulting in 12 DAPI stained bodies corresponding to non-recombinant univalents (Jantsch *et al.*, 2004) (Figure 1D). In *zhp-3*^{S308A}, *zhp-3*^{S366A}, and *zhp-3*$^{S308A, S366A}$ mutants, oocytes had an average of 6 DAPI bodies (Figure 1D).

We also stained germlines with antibodies against HTP-3 and HTP-1, meiotic chromosomal proteins that preferentially localize to the long and short arms of bivalents (Martinez-Perez et al., 2008) to determine if there were defects in bivalent morphology. HTP-3 localizes to both the long and short arm of bivalents in a cruciform pattern, and HTP-1 localizes to the long arm on wildtype bivalents (Figure 1E) (Martinez-Perez *et al.*, 2008). In contrast, HTP-3 and HTP-1 are lost on the long arm in *zhp-3(jf61)* null mutants (Figure 1E). We found that HTP-3 localizes to both the long and short arm and HTP-1 localizes to the long arm properly in *zhp-3*^{S308A}, *zhp-3*^{S366A}, and *zhp-3*$^{S308A, S366A}$ mutants (Figure 1E), indicating that bivalent morphology is unaffected in *zhp-3* phosphorylation mutants.

Finally, we tested whether mutation of these sites results in chromosome missegregation by assessing the number of viable and male progeny for each phosphorylation mutant strain. Males are found in ~1/1000 progeny in wildtype

strains, while *zhp-3(jf61)* null mutants have reported 1.3% viable progeny and ~30% males (Bhalla *et al.*, 2008). We found that both single phosphorylation mutants and double phosphorylation site mutants had 100% viable progeny and 0.03%, 0.2%, and 0.1% male progeny respectively (Figure 1F), illustrating that mutation of these sites does not cause general defects in meiosis.

Discussion

Regulation of meiotic recombination is essential for proper development of gametes and preventing aneuploidy. While ZHP-3 is essential for meiotic recombination in *C. elegans*, whether and how it is regulated to promote recombination remains an active area of investigation. While we found that ZHP-3 is phosphorylated on its C-terminus at S308 and S366 *in vitro*, mutation of these phosphorylation sites *in vivo* does not result in defects in ZHP-3's localization (Figures 1B and 1C), bivalent formation (Figures 1D and 1E), or chromosome segregation (Figure 1F).

We conclude that ZHP-3 is either not regulated by these phosphorylation sites or that there is potential redundancy for ZHP-3 regulation by phosphorylation. Whether ZHP-3 is modified at other residues by phosphorylation or other post-translational modifications remain open questions in the field. It has also been recently discovered that there are additional ZHP proteins that play a role in crossover formation in *C. elegans* (Nguyen et al., 2018; Zhang et al., 2018). How these proteins coordinate to promote recombination and whether they require protein modifications are interesting

questions for determining how crossover formation is regulated to promote meiotic chromosome segregation.

Materials and Methods

C. elegans strains and genetics

The Bristol N2 *C. elegans* strain (Brenner, 1974) was used as the wildtype control for all experiments and as the parent strain for the single phosphorylation mutant CRISPR/Cas9 genome editing experiments. The *zhp-3* ^{S366A} strain was used as the background to create the *zhp-3* ^{S308A,S366A} double phosphorylation mutant.
Strains were maintained at 20°C under standard conditions for all immunostaining experiments and maintained at 15°C for all CRISPR/Cas9 genome editing experiments.

ZHP-3 protein expression

Two fragments of ZHP-3, the N-terminus (aa 1-173) and the C-terminus (aa 174-387), were first amplified from cDNA, and then inserted into pDONR221 via BP reaction and shuttled into pDEST15, which contains an N-terminal GST tag, via LR reactions using the Gateway Cloning System (Invitrogen). GST-tagged ZHP-3 fragments were expressed in BL21 codon plus cells (Agilent) overnight at 18ºC (14-16 hours) to maintain solubility after induction with 0.2 mM IPTG. Cells were lysed in a coffee grinder, resuspended in cold lysis buffer (1X PBS, 0.5% Tween-20, 1M NaCl, 10 mM DTT) with protease inhibitor (1 mM PMSF), sonicated, and then spun for 1 hour at 35k to clarify lysate. A glutathione agarose column (Sigma) was equilibrated in lysis buffer, the lysate was loaded, the column washed (1X PBS, 0.05% Tween-20, 0.5 mM DTT, 0.25 M KCl), washed a second time in the same

buffer omitting detergent (Tween-20). Protein then was eluted from the column (50 mM Tris pH8, 0.25 M KCl, 5 mM reduced glutathione) in 1 mL fractions. The fractions containing protein (Bradford Assay, Bio-Rad) were combined and dialyzed overnight (50 mM Hepes-KOH pH7.4, 0.25 M KCl, 30% glycerol) and then aliquoted and stored at -80 ºC.

In vitro Kinase Assays

Kinase assays were performed at 30ºC in 20 µL reactions with 1X kinase buffer (50 mM Tris pH7.4, 1 mM DTT, 25 mM beta-glycerophosphate, 5 mM MgCl2 ,10 mM ATP) for 30 minutes. Reactions included 0.5 µL ^{32}P- γ-ATP (Perkin Elmer), 0.5ul of activated Chk1 (Sigma), and 2 µg of substrate. Reactions were quenched by adding 20 µL 2X sample buffer and boiling for 5 minutes. Reactions were run out in duplicate on two 10% SDS-PAGE gels, one was stained with Coomassie to verify equivalent amounts of substrate were utilized, and one was dried and then exposed to a phosphor screen (GE Life Sciences) for analysis of phosphorylation.

Mass Spectrometric Analysis

In vitro assays were performed as above without radiolabeled ATP. Samples were frozen in liquid nitrogen and sent to the QB3/Chemistry Mass Spectrometry Facility at University of California, Berkeley, which performed the desalting and trypsin digest prior to mass spectrometry. Mass spectrometry produced multiple peptides of

the protein sequence of the C-terminus and GST tag, indicating good coverage, and identified S308 and S366 as the *in vitro* phosphorylated residues

Generating phosphorylation mutant strains using CRISPR/Cas9 genome editing

The *zhp-3*^{S308A}, *zhp-3*^{S366A}, and *zhp-3*$^{S308A, S366A}$ phosphorylation mutant strains were all generated using a CRISPR/Cas9 ribonucleoprotein (RNP) approach (Paix *et al.*, 2015) combined with the co-conversion genome editing method (Arribere *et al.*, 2014).

N2 young adults were injected with a mix that included a *zhp-3* specific crRNA (IDT-Alt-R™, 100µM stock), the *dpy-10* co-conversion crRNA (IDT-Alt-R™, 100µM stock) , tracrRNA (IDT-Alt-R™, 100µM stock) a *zhp-3* specific repair oligo (IDT, 50µM stock) the *dpy-10* co-conversion repair oligo (IDT, 50µM stock), and purified Cas9 protein (40µM stock). F1 *roller* and *dpy* progeny from injected P0's were isolated to individual plates, and non-rolling non *dpy* siblings from jackpot plates (> 10 transformed worms) were grouped 3-5 F1's per plate. After F2 progeny were generated, F1's were screened for the respective phosphorylation mutant allele via PCR and restriction digest. F2's from a F1 plate that had the confirmed mutant allele were singled to identify homozygotes for each phosphorylation mutation. All phosphorylation mutant strains were confirmed via sequencing. Phosphorylation mutant strains were outcrossed to N2 worms 1-2 times prior to analysis.

For creating the *zhp-3*^{S308A} strain, the following sgRNA was used: 5'-GGA CAA AAC UAG UAU GUC ACG UUU UAG AGC UAU rGrCrU-3'. The following single stranded oligo was used for the S308A mutation repair template: 5'-GGA CAA AAC TAG TAT GTC ACT CGA AAA TTG GAG GCA AAA TAG AGC GAA TGC ATT CGG AGT GCA TGA TAT GTG AGA TAT TTT CAA AGT ATC TGT GAT TCC TAA TTC-3'.

For creating the *zhp-3*^{S366A} strain, the following sgRNA was used: 5'– AAA AGA GUG AAU GAC AGA CCG UUU UAG AGC UAU rGrCrU –3'. The following single stranded oligo was used for the S366A mutation repair template: 5 – GTG CAG CTG GAT TCG ACC GTC AGC AGA TAC AAG AAA TGC GTC GAA TCT CAG CTC AAC CTG GTC TGT CAC CCA CTC TTT TAT TCC TCA ATT TCC CTC GAC CCT CTC ATC –3'.

For creating the *zhp-3*$^{S308,\ S366A}$ strain, the same S308A sgRNA and oligo repair template above were used to create the S308A mutation in the *zhp-3*^{S366A} mutant background.

DAPI staining and Immunostaining

Adult hermaphrodites were fixed and stained 24-26 hours post-L4 larval stage as in (Bhalla and Dernburg, 2005). For visualizing bivalents in mature oocytes for quantification, adult hermaphrodites were fixed and stained 48 hours post L4 stage.

For assessing ZHP-3 localization, the following primary antibodies were used: guinea pig anti-ZHP-3 (1:250) (Bhalla *et al.*, 2008), rabbit anti-SYP-1 (1:250) (MacQueen et al., 2002), chicken anti-HTP-3 (1:500) (MacQueen et al., 2005). All secondary antibodies were used at a 1:500 dilution and included: Alexa 488 anti-guinea pig (Invitrogen), Cy3 anti-rabbit (Jackson Immunochemicals), and Cy5 anti-chicken (Jackson Immunochemicals).

For assessing bivalent formation, the following primary antibodies were used: rabbit anti-HTP-1 (1:400) (Martinez-Perez *et al.*, 2008) and chicken anti-HTP-3 (1:500) (MacQueen *et al.*, 2005). All secondary antibodies were used at a 1:500 dilution and included: Alexa 488 anti-rabbit (Invitrogen) and Cy3 anti-chicken (Jackson Immunochemicals).

DAPI in 1X PBST was used at a concentration of 1:5000 for all experiments.

Images of immunostaining experiments were obtained using a DeltaVision Personal DV system (Applied Precision) equipped with a 100× N.A. 1.40 oil-immersion objective (Olympus), resulting in an effective XY pixel spacing of 0.064 or 0.040 μm. Z-stacks were collected at 0.2-μm *Z*-spacing and processed by constrained, iterative deconvolution. Imaging, image scaling, and analysis were performed using functions in the softWoRx software package. Projections were calculated by a maximum intensity algorithm. Composite images from immunostaining experiments were processed and some false coloring was performed using Fiji.

Quantification of bivalents

Bivalent quantification was performed on worms 48 hours post L4 larval stage. Each genotype included at least 3 germlines for quantification.

Viability assay and male counts

N2, *zhp-3(jf61)*, *zhp-3*^{S308A}, *zhp-3*^{S366A}, and *zhp-3*$^{S308A, S366A}$ late L4 stage worms were isolated to plates and maintained at 20 degrees. F1 embryos and oocytes were scored at 24, 48 and 72 hours post L4 larval stage. Once F1's reached the late L4 stage, viable and male progeny were scored. The total brood size, percent viability and percent HIM phenotype were calculated for each strain. A Wilcoxon-Mann Whitney test was performed to assess statistical significance.

Figures and statistics

Figures were assembled using Adobe Illustrator. All histograms and statistics were performed using R (R core team) with the ggplot2 package (Wickham, 2016). For bivalent quantification, viability assay and male counts, a two sided-Wilcoxon-Mann Whitney test was used to determine statistical significance.

CHAPTER 2: PCH-2 delegates its regulation of meiotic prophase events through different meiotic HORMADS

Abstract

During meiotic prophase, the essential events of pairing, synapsis and recombination are coordinated to promote fidelity and prevent aneuploidy. The conserved AAA+ ATPase, PCH-2 remodels a family of proteins that have conserved HORMA domains (HORMADs) to control a variety of meiotic chromosome behaviors, including coordinating and proofreading pairing, synapsis and recombination between homologous chromosomes to guarantee crossover assurance and accurate chromosome segregation. However, how PCH-2 remodels meiotic HORMADS to accomplish this coordination is poorly understood. Here we show that PCH-2 regulates pairing, synapsis and recombination in *C. elegans* by remodeling meiotic HORMADS from a closed active conformation to an unlocked inactive conformation. Further, PCH-2 coordinates these events by distributing its regulation to different meiotic HORMADS: PCH-2 acts on HTP-3 to regulate pairing and synapsis, and on HIM-3 to promote crossover assurance. This work provides support for the hypothesis that delegating non-redundant roles for meiotic HORMADS explains the evolutionary expansion of this protein family as a general feature of meiosis. Taken together, our work illustrates a novel mechanism for how PCH-2 coordinates these meiotic prophase events in order to promote fidelity and prevent aneuploidy.

Introduction

All sexually reproducing organisms depend on the specialized cell division called meiosis, which produces haploid gametes such as sperm, eggs and pollen. During meiosis, cells combine one round of DNA replication with two rounds of chromosome segregation, all of which is tightly regulated to ensure that gametes inherit the correct number of chromosomes. Errors in meiosis can lead to aneuploid gametes that cause infertility, birth defects and miscarriages. (Hassold and Hunt, 2001). Therefore, understanding how meiotic events are coordinated has important implications for reproductive health.

During prophase I of meiosis, chromosome pairs or homologs undergo a series of events known as pairing, synapsis, and crossover recombination. First, homologs find each other and pair within the nucleus. Next, a molecular structure called the synaptonemal complex (SC) assembles between homologs and stabilizes homolog pairing in a process called synapsis. Finally, homologs undergo crossover recombination, which serves two important purposes. First, it shuffles alleles to create new genetic combinations that can be acted upon by natural selection. Second, it physically links homolog pairs, which is required for homologs to properly remodel, orient on the spindle, and segregate correctly during the first meiotic division.

Despite being described as a linear pathway, the processes of pairing, synapsis and recombination between homologous chromosomes are highly dynamic and can even temporally overlap, requiring active coordination (Dernburg *et al.*, 1998) (McKim et al., 1998). Further, these events can also initiate inappropriately between non-homologous chromosomes and therefore need to be corrected. We have shown that the highly conserved AAA+ ATPase, PCH-2, contributes to both this coordination and correction (Deshong et al., 2014) (Giacopazzi et al., 2020). However, how it carries out these roles is currently unclear.

Pachytene checkpoint 2 (PCH-2) has been shown to structurally remodel a family of proteins that contain a HORMA domain (HORMAD proteins) to regulate a variety of chromosome behavior, including meiotic interhomolog interactions. HORMADS were named after the first proteins in this family to be discovered in budding yeast: Hop1, Rev7, and Mad2 (Aravind and Koonin, 1998). Despite having essential roles in meiotic prophase, meiotic HORMADS differ greatly across eukaryotes in the number of family members they contain. *S. cerevisiae* has one meiotic HORMAD (Hollingsworth et al., 1990) (Lorenz et al., 2004), mice and *Arabidopsis* have two (Fukuda et al., 2010) (Caryl et al., 2000) (Wojtasz et al., 2009) and *C. elegans* has four (Zetka et al., 1999) (Couteau and Zetka, 2005) (Goodyer et al., 2008; Martinez-Perez and Villeneuve, 2005). HORMAD proteins have a characteristic N-terminal HORMA domain that allows HORMADS to adopt two different conformations: a closed active conformation and an open/unlocked inactive conformation. Biochemical

and structural studies show that PCH-2 is directly responsible for this conversion event for at least some HORMADS. For example, PCH-2 has been shown to convert the spindle checkpoint HORMAD, Mad2, from a closed to open conformation (Alfieri et al., 2018) (Brulotte et al., 2017; Ye et al., 2015), allowing Mad2's disassembly from the mitotic checkpoint complex, silencing of the spindle checkpoint, and anaphase onset (Alfieri *et al.*, 2018) (Brulotte *et al.*, 2017) (Eytan et al., 2014; Miniowitz-Shemtov et al., 2015; Wang et al., 2014) (Ye *et al.*, 2015). Additionally, this conversion event has also been demonstrated to be required for spindle checkpoint activation (Ma and Poon, 2016; Nelson et al., 2015; Yost et al., 2017) (Ma and Poon, 2018).

While this provides a powerful framework to imagine PCH-2's molecular mechanism during meiotic prophase, its specific role has been challenging to elucidate. Closed versions of meiotic HORMADs assemble on meiotic chromosomes to drive pairing, synapsis and recombination (Kim et al., 2014) (Kim *et al.*, 2015) and in plants, PCH2 is essential to remodel its meiotic HORMAD, ASY1, in the cytoplasm to ensure its transit into meiotic prophase nuclei and assembly on chromosomes (Ye *et al.*, 2015). Pch2/PCH2/TRIP13 has been shown to interact with meiotic HORMADs (Chen et al., 2014), and removes or redistributes meiotic HORMADS from chromosome axes in budding yeast (Börner et al., 2008) (Joshi et al., 2009), *Arabidopsis* (Lambing et al., 2015) and mice (Wojtasz *et al.*, 2009), promoting meiotic progression (Raina and

Vader, 2020). However, whether unlocked meiotic HORMADS play additional roles during meiotic prophase is unclear.

Here we demonstrate that PCH-2 acts on the meiotic HORMADS to coordinate pairing, synapsis and crossover recombination during meiosis in *C. elegans*. We show that a missense mutation in the HORMA domain of HTP-3 suppresses pairing and synapsis defects in *pch-2* mutants but exacerbates its recombination defects, indicating these two proteins cooperate to promote pairing and synapsis but regulate recombination independently. We also show that a corresponding mutation in *him-3* suppresses recombination defects in *pch-2* mutants, suggesting that PCH-2 acts on HIM-3 specifically to promote crossover recombination. Finally, we show that corresponding mutations in the meiotic HORMAD HTP-1 cause a delay in meiotic progression, suggesting that PCH-2 potentially acts on HTP-1 to promote meiotic progression. Taken together, our work shows that PCH-2 delegates its regulation of different meiotic prophase events to different meiotic HORMADs, offering new insight into how PCH-2 mechanistically coordinates the events of pairing, synapsis and recombination and providing a potential explanation for why this family of meiotic HORMADS has dramatically expanded in *C. elegans*.

Results

htp-3 H96Y suppresses the acceleration of pairing and synapsis in *pch-2* mutants

htp-3(vc75) is a missense mutation that replaces histidine 96 with a tyrosine in the HORMA domain (H96Y). HTP-3^{H96Y} properly localizes to meiotic chromosomes (Couteau and Zetka, 2011) and does not appear to affect pairing, synapsis and crossover recombination (Couteau and Zetka, 2011) (Bohr et al., 2018). However, we and others previously showed that this mutation in *htp-3* abolished meiotic checkpoint responses in *C. elegans* (Couteau and Zetka, 2011) (Bohr *et al.*, 2018). Because of this phenotype, we analyzed HTP-3's relationship with PCH-2. To test whether PCH-2 genetically interacts with HTP-3 to regulate pairing, we generated *pch-2;syp-1*, *htp-3^{H96Y};syp-1,* and *pch-2;htp-3 H96Y;syp-1* mutants and assessed pairing when compared with *syp-1* single mutants. SYP-1 is a central element protein of the synaptonemal complex (SC) (MacQueen *et al.*, 2002). *syp*-1 null mutants successfully undergo pairing despite the failure in loading SC components, particularly at specific loci called Pairing Centers (PCs). Therefore, this allows direct analysis of pairing in the absence of synapsis. We performed immunofluorescence against the HIM-8 protein, which localizes to PCs on the X chromosome (Phillips et al., 2005), to assess pairing at this locus throughout the germline: two HIM-8 foci indicate the X-chromosomes are unpaired while a single HIM-8 focus indicates paired X-chromosomes. Because meiotic nuclei are arranged in spatiotemporal gradient in germlines, we divided the germline into six equivalently sized zones to

perform a meiotic time-course and determined the percentage of nuclei with a single HIM-8 focus in each zone (Fig. 2A and 2B). Similar to previous work, we found that there is an increase in percentage of nuclei with paired X chromosomes in zone 2 for *pch-2;syp-1* mutants (76%, Fig. 2C) compared to *syp-1* controls (49%, Fig. 2C), showing that the rate of pairing is accelerated in the absence of *pch-2. htp-3* ^{H96Y}*;syp-1* mutants have a similar rate of pairing compared to *syp-1* controls (46%, Fig. 2C), demonstrating that this mutation does not affect pairing. Interestingly, we found that *pch-2;htp-3* ^{H96Y}*;syp-1* triple mutants have a similar rate of pairing compared to *syp-1* and *htp-3* ^{H96Y}*;syp-1* double mutants (49%, Fig. 2C), illustrating that *htp-3*^{H96Y} suppresses the acceleration of pairing observed in *pch-2* mutants. Since this mutation is in the HORMA domain of HTP-3, these data suggest that PCH-2 acts on HTP-3 through HTP-3's HORMA domain to regulate the progression of pairing.

Next, we tested HTP-3's effect on synapsis. We analyzed synapsis in germlines from control, *pch-2*, *htp-3* ^{H96Y}, and *pch-2;htp-3* ^{H96Y} mutant worms by performing immunofluorescence against the axial element HTP-3 and the central element SYP-1. We then determined the fraction of nuclei with complete synapsis in each zone. Complete synapsis is visible as full co-localization of HTP-3 and SYP-1, whereas nuclei with incomplete synapsis have stretches of HTP-3 without SYP-1 signal (arrowheads, Fig. 2D). Similar to previous data, we report that *pch-2* null mutants have an accelerated rate of synapsis (61%, Fig. 2E) compared to wildtype controls (33%, Fig. 2E) in zone 2 and a delay in desynapsis in zone 6 (Deshong *et al.*, 2014)

Figure 2. *htp-3 H96Y* suppresses the acceleration of pairing and synapsis in *pch-2* mutants.

A. Cartoon depicting zones for quantification in the *C. elegans* germline. **B.** Meiotic nuclei stained with DAPI (magenta) and HIM-8 (green). Scalebar indicates 5 microns. **C.** Quantification of percent nuclei paired in zones 1-6 for *syp-1* (blue), *pch-2;syp-1* (red), *htp-3;syp-1* (green) and *pch-2;htp-3;syp*-1 (purple) mutant strains. ** indicates p value <0.01. **D.** Meiotic nuclei stained with SYP-1(magenta) and HTP-3 (green). Arrows indicates unsynapsed chromosomes. Scalebar indicates 5 microns. **E.** Quantification of percent nuclei synapsed in zones 1-6 for wildtype (blue), *pch-2* (red), *htp-3* (green) and *pch-2;htp-3* (purple) mutant strains. ** indicates p value <0.01. **F.** Quantification of percent nuclei synapsed in zones 1-6 for *meDf2*/+ (blue), *pch-2;meDf2*/+ (red), *htp-3;meDf2*/+ (green) and *pch-2;htp-3;meDf2*/+ (purple) mutant strains. Significance was assessed using two-tailed Fisher's exact tests.

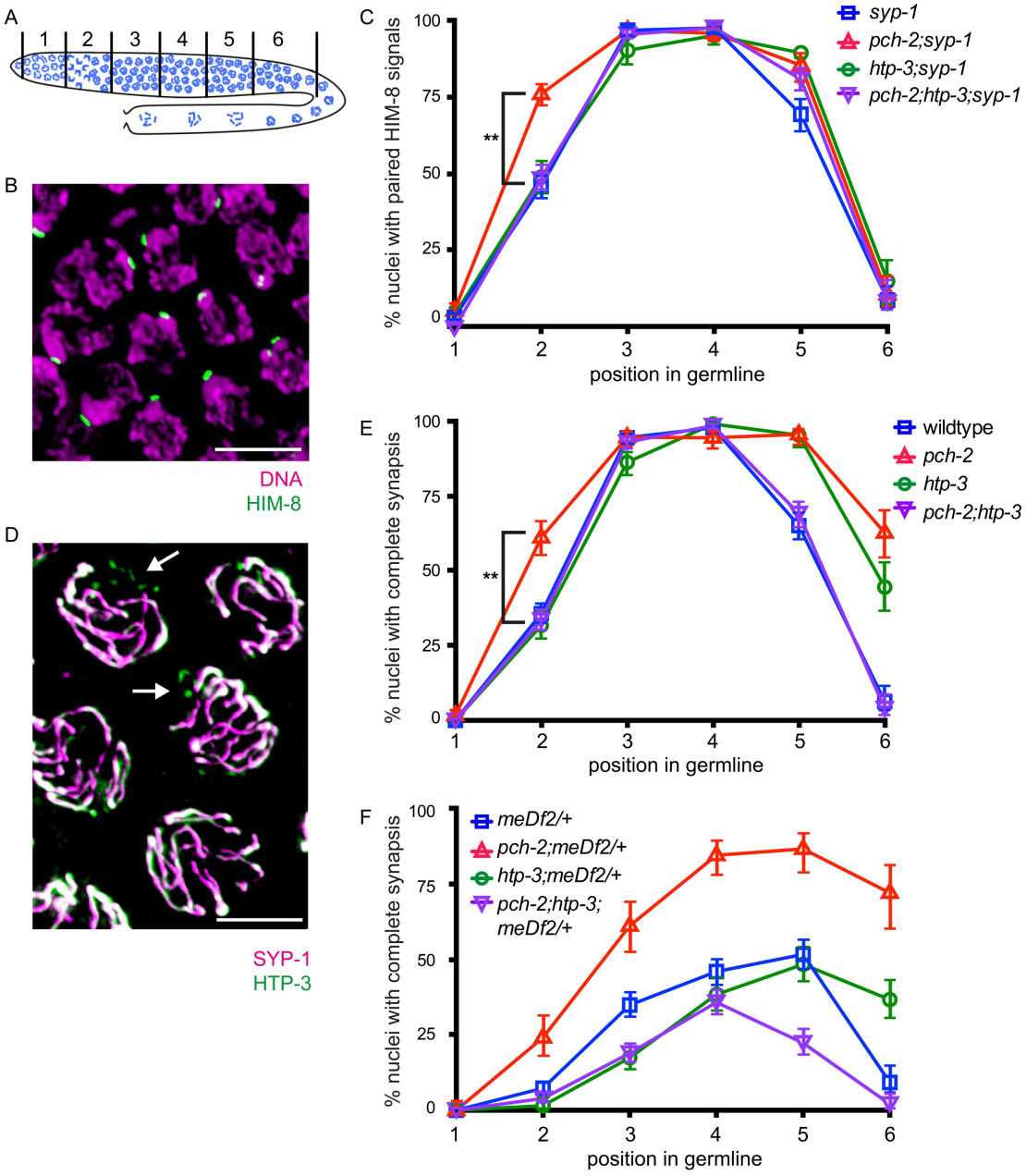
A
1
2
3
4
5
6
B
DNA
HIM-8
D
SYP-1
HTP-3
C
% nuclei with paired HIM-8 signals
100
75
50
25
0
**
1
2
3
4
5
6
position in germline
syp-1
pch-2;syp-1
htp-3;syp-1
pch-2;htp-3;syp-1
E
% nuclei with complete synapsis
100
75
50
25
0
**
1
2
3
4
5
6
position in germline
wildtype
pch-2
htp-3
pch-2;htp-3
F
% nuclei with complete synapsis
100
75
50
25
0
1
2
3
4
5
6
position in germline
meDf2/+
pch-2;meDf2/+
htp-3;meDf2/+
pch-2;htp-3;
meDf2/+

(Giacopazzi *et al.*, 2020) (Fig. 2E). *htp-3* ^{H96Y} mutants have a similar rate of synapsis compared to wildtype controls (36%, Fig. 2E), suggesting that the rate of synapsis is unaffected in this background. Similar to our pairing results, we found that *pch-2;htp-3* ^{H96Y} double mutants have a similar rate of synapsis compared to wildtype and *htp-3* ^{H96Y} controls (34%, Fig. 2E), indicating that *htp-3*^{H96Y} suppresses the acceleration of synapsis in *pch-2* mutants. These data are consistent with a model in which PCH-2 acts on HTP-3's HORMA domain to regulate the rate of synapsis.

To further solidify that PCH-2 acts on HTP-3 to regulate synapsis, we analyzed synapsis in *meDf2* heterozygotes (*meDf2*/+). *meDf2* is a mutation where PC regions are deleted from the X chromosome. Since PCs are essential for pairing and synapsis (MacQueen *et al.*, 2002), *meDf2* homozygotes fail to pair and synapse X chromosomes while *meDf2* heterozygotes behave like a partial loss of function mutation: ~50% of nuclei complete synapsis of X chromosomes while the remaining 50% have unsynapsed X chromosomes (MacQueen *et al.*, 2002). In *pch-2;meDf2*/+ worms, ~85% of nuclei complete synapsis, demonstrating that PCH-2 inhibits synapsis when PC function is compromised.

We generated *pch-2;htp-3* ^{H96Y}*;meDf2*/+ triple mutants and analyzed the rate of synapsis, comparing it to controls. Similar to previous results, we found that 87% of nuclei in *pch-2;meDf2*/+ mutants achieve complete synapsis in zone 5 compared to 48% complete synapsis for *meDf2*/+ worms (Fig. 2F). *htp-3* ^{H96Y}*;meDf2*/+ worms

have 52% of nuclei with complete synapsis in zone 5, similar to *meDf2/+* single mutants (Fig. 2F). In contrast to *pch-2;meDf2/+* mutants, *pch-2;htp-3 ^{H96Y};meDf2/+* triple mutants show reduced levels of synapsis in zone 5 (22%, Fig. 2F), more similar to *htp-3 ^{R96Y};meDf2/+* double and *meDf2/+* single mutants. These data indicate that PCH-2 inhibits synapsis when PC function is compromised through the HORMA domain of HTP-3, similar to its effect when PCs are fully functional. Taken together, these results indicate that PCH-2 acts on the meiotic HORMAD HTP-3 to regulate pairing and synapsis.

htp-3 ^{H96Y} exacerbates defects in DNA repair and crossover formation in *pch-2* mutants

We next tested whether PCH-2 regulates recombination through HTP-3 by assaying DNA repair and crossover formation in *pch-2;htp-3 ^{H96Y}* double mutants. The rate of DNA repair is assessed by quantifying the number of RAD-51 foci per nucleus throughout the germline (Fig. 3A). The appearance of RAD-51 foci on meiotic chromosomes is associated with the introduction of double-strand breaks and their disappearance is associated with the entry of double-strand breaks into repair pathways. RAD-51 numbers peak in zone 4 in wildtype animals, increasing to an average of 2 per nuclei, and decrease as RAD-51 is removed during DNA repair. *pch-2* mutants have a lower average of RAD-51 foci per nucleus in zones 4-6 (Fig. 3B),

Figure 3. *htp-3 ^{H96Y}* exacerbates defects in DNA repair and crossover formation in *pch-2* mutants.

A. Meiotic nuclei stained with DAPI (magenta) and RAD-51 (green). Scalebar indicates 5 microns. **B.** Quantification of number of RAD-51 foci in zones 1-6 for wildtype (blue), *pch-2* (red), *htp-3* (green) and *pch-2;htp-3* (purple) mutant strains. **C.** Meiotic nuclei stained with DNA (magenta) and GFP::COSA-1 (green). Left indicates representative nuclei with 6 GFP::COSA-1 foci. Right indicates representative nuclei with less than 6 GFP::COSA-1 foci. Scalebar indicates 5 microns. **D.** Quantification of percent nuclei with less than 6 GFP::COSA-1 foci for wildtype, *pch-2*, *htp-3*, and *pch-2;htp-3* mutant strains. ** indicates p value <0.01. **E.** Oocytes stained with DAPI. Left indicates representative oocyte with zero univalents. Right indicates representative oocyte with univalents (arrows). Scalebar indicates 5 microns. **F.** Quantification of percent oocytes with univalents for wildtype, *pch-2*, *htp-3*, and *pch-2;htp-3* mutant strains. ** indicates p value <0.01. Significance was assessed using two-tailed student t-tests.

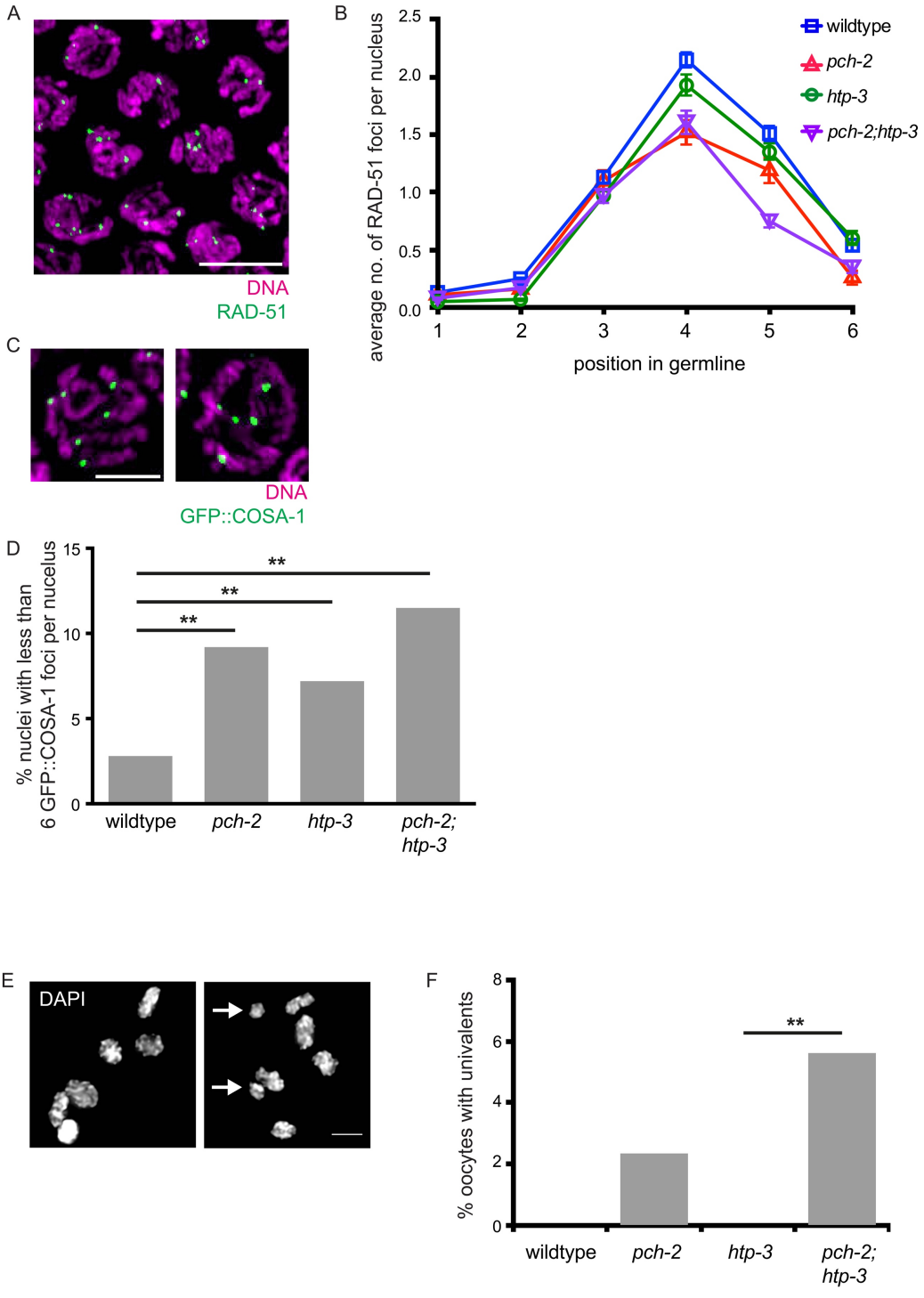
A
DNA
RAD-51
B
average no. of RAD-51 foci per nucleus
position in germline
wildtype
pch-2
htp-3
pch-2;htp-3
C
DNA
GFP::COSA-1
D
% nuclei with less than 6 GFP::COSA-1 foci per nucelus
wildtype
pch-2
htp-3
pch-2; htp-3
E
DAPI
F
% oocytes with univalents
wildtype
pch-2
htp-3
pch-2; htp-3

consistent with previous findings that that *pch-2* mutants exhibit a faster rate of DNA repair compared to wildtype controls. *htp-3* ^{H96Y} mutants show a similar rate of DNA repair as wildtype germlines (Fig. 3B), although the average number of RAD-51 foci is slightly lower than wildtype (Couteau and Zetka, 2011). By contrast, *pch-2;htp-3* ^{H96Y} double mutants not only show an accelerated rate of DNA repair, similar to *pch-2* single mutants, they have a reduced average number of RAD-51 foci in zone 5 (0.75 foci, Fig. 3B), showing that mutation of *htp-3* exacerbates the acceleration of DNA repair in *pch-2* mutants. Because *htp-3(vc75)* and *pch-2* mutants do not have reduced numbers of double-stranded breaks (Couteau and Zetka, 2011) (Deshong *et al.*, 2014), these results rather reflect changes in the rate of DNA repair. Further, this indicates that in contrast to our findings for pairing and synapsis, PCH-2 does not act on HTP-3 to regulate the rate of DNA repair but rather both proteins regulate DNA repair independently.

To determine if PCH-2 acts on HTP-3 to regulate crossover formation, we quantified the number of GFP::COSA-1 foci for each meiotic nucleus. COSA-1 is a cyclin like protein that localizes specifically to presumptive crossovers, serving as a cytological marker for crossover formation (Yokoo *et al.*, 2012). Because *C. elegans* contain 6 pairs of chromosomes and exhibit strong crossover interference, wildtype nuclei have an average of 6 GFP::COSA-1 foci per nucleus (Fig. 3C) (Yokoo *et al.*, 2012). Our findings also reflect this, where we report only 3% of nuclei having less than 6 GFP::COSA-1 foci (Fig. 2D). We also found that the incidence of nuclei with less

than 6 GFP::COSA-1 foci increases to 9% of nuclei in *pch-2* mutants (Fig. 3D), recapitulating previous findings that *pch-2* mutants exhibit a loss of crossover assurance (Deshong *et al.*, 2014) (Giacopazzi *et al.*, 2020) *htp-3* ^{H96Y} single mutants also show an increase in the number of nuclei with less than 6 GFP::COSA-1 crossovers compared to wildtype (7%, Fig. 3D), consistent with their checkpoint role (Couteau and Zetka, 2011). Consistent with our analysis of DNA repair, the number of nuclei with less than 6 GFP::COSA-1 foci in *pch-2;htp-3* ^{H96Y} double mutants increases to 11% percent (Fig. 3D), suggesting that there is an additive effect for crossover defects. These data illustrate that PCH-2 and HTP-3 work independently to regulate crossover formation.

We further tested whether PCH-2 acts on HTP-3 to regulate crossover recombination by visualizing chromosome pairs held together by chiasmata. Wildtype *C. elegans* oocytes contain 6 pairs of chromosomes or bivalents, and these can be visualized as 6 "DAPI stained bodies" (Fig. 3E). Defects in recombination produce homologs without chiasmata, or univalents, in oocytes (arrows, Fig. 3E). In our analysis of wildtype oocytes, we did not observe any univalents (Figure 3F). Similar to previous data, we found that the incidence of univalents in *pch-2* mutants increases to 2% compared to wildtype controls (Fig. 3F). *htp-3* mutants resembled control worms in that we did not observe any univalents (Fig. 3F). The incidence of univalents for *pch-2;htp-3* ^{H96Y} double mutants is significantly increased to 6% compared to both *pch-2*

and *htp-3* single mutants (Fig. 3F), providing additional evidence that PCH-2 does not act on HTP-3 regulate crossover recombination.

Overall, these data indicate that in contrast to PCH-2 acting on HTP-3 to regulate both pairing and synapsis, PCH-2 does not regulate DNA repair or crossover recombination by acting on HTP-3.

htp-3 ^{H96Y} does not affect meiotic progression

In budding yeast, Pch2's remodeling of the meiotic HORMAD, Hop1, contributes to meiotic progression. Since we've shown that *htp-3*^{H96Y} mutants genetically interact with *pch-2* mutants in *C. elegans*, we tested whether *htp-3* ^{H96Y} mutants affected meiotic progression. We assessed meiotic progression by performing immunofluorescence against a factor required for double-strand break formation, DSB-1. DSB-1 localizes to meiotic chromosomes to facilitate double-strand break formation. In response to meiotic defects, DSB-1 persists on chromosomes to maintain a period of competency for double-strand break formation to promote crossover assurance. We quantified the fraction of meiotic nuclei that were positive for DSB-1 and could not detect any difference between control and *htp-3* ^{R96Y} mutant germlines (Fig. 4A), illustrating that this mutation does not affect meiotic progression.

Figure 4. *htp-3 ^{H96Y}* does not affect meiotic progression.

A. Quantification of DSB-1 positive meiotic nuclei for wildtype and *htp-3 ^{H96Y}* mutant strains. NS indicates non-significant. **B.** Quantification of DSB-1 positive meiotic nuclei for syp-1 and *htp-3 ^{H96Y};syp-1* mutants. NS indicates non-significant. Statistical significance was assessed using two-tailed Fisher's exact tests.

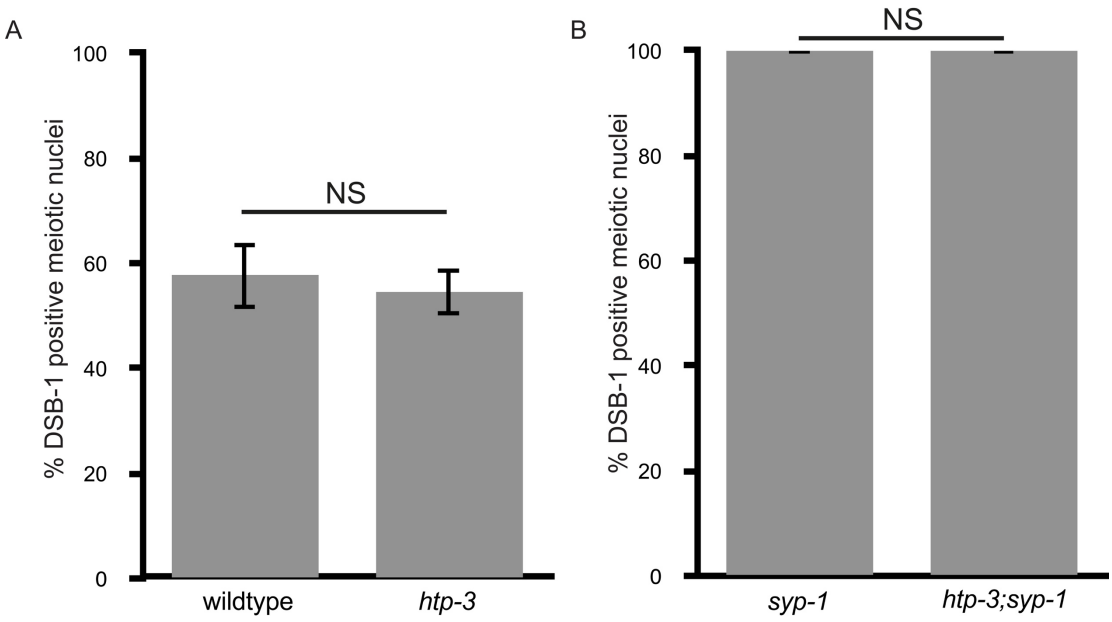

A null mutation in *htp-3* abolishes the delay in meiotic progression observed when there are defects in synapsis, such as in *syp-1* mutants. To determine whether *htp-3* ^{H96Y} affected meiotic progression in *syp-1* mutants, we quantified the fraction of DSB-1 positive meiotic nuclei in both *syp-1* and *syp-1;htp-3* ^{H96Y} mutants and could not observe any difference between these genotypes (Fig. 4B), indicating that *htp-3* ^{H96Y} does not disrupt the extension of meiotic progression observed when there are meiotic defects.

him-3^{R93Y} does not suppress the acceleration of pairing or synapsis in *pch-2* mutants

Our findings that PCH-2 acts on HTP-3 to promote pairing and synapsis, but not recombination indicates that PCH-2 regulates recombination through an HTP-3 independent mechanism. Additionally, it allows us to hypothesize two potential models. One possibility is that meiotic HORMADS are cleanly delegated to regulate specific meiotic prophase events, where HTP-3 is delegated to regulate pairing and synapsis and a different meiotic HORMAD regulates recombination. Alternatively, there may be redundancy between the meiotic HORMADS. Given that there are two other HORMADS essential for meiosis in *C. elegans*, we next tested whether PCH-2 acts on either HIM-3 or HTP-1 to promote pairing, synapsis or recombination, providing an opportunity to differentiate between these two scenarios.

Using CRISPR/Cas9 gene editing, we made an analogous missense mutation to the *htp-3*^{H96Y} allele in *him*-3, where arginine 93 was replaced with a tyrosine (*him-3*^{R93Y}).

Both of these residues are positioned similarly within the HORMA domain, suggesting that mutation of this residue in HIM-3 would have a similar effect on protein function as the *htp-3*^{H96Y} allele on HTP-3. First we analyzed pairing in *syp-1*, *pch-2;syp-1*, *him-3*^{R93Y}*;syp-1*, and *pch-2; him-3*^{R93Y}*; syp-1* mutants by performing immunofluorescence against HIM-8 (Fig. 5A and 5B). Similar to our analysis of *htp-3*^{H96Y} allele, we found that *pch-2;syp-1* mutants have an increase in the number of nuclei that completed pairing (61%, Fig. 5C) in zone 2 compared to *syp-1* controls (45%, Fig. 5C). *him-3*^{R93Y}*; syp-1* mutants similarly show 44% of nuclei completed pairing in zone 2, demonstrating that this mutation does not affect pairing (Fig. 5B). Surprisingly, we found that *pch-2; him-3*^{R93Y}*; syp-1* triple mutants also show an accelerated rate of pairing phenotype (63%, Fig. 5C) suggesting that the *pch-2* phenotype is not suppressed by the *him-3*^{R93Y} mutation. These data indicate that PCH-2 does not act on HIM-3 through HIM-3's HORMA domain to regulate the progression of pairing.

Next, we assessed the rate of synapsis in wildtype, *pch-2*, *him-3*^{R93Y}, and *pch-2; him-3*^{R93Y} germlines by performing immunofluorescence against SYP-1 and HTP-3 (Fig. 5D). Similar to our results for the *htp-3*^{H96Y} allele, we found that *pch-2* mutants have an accelerated rate of synapsis in zone 2 (13%, Fig. 5E) compared to wildtype controls (3%, Fig. 5E). In *him-3*^{R93Y} mutants, we found that there was also an increase in the number of nuclei that completed synapsis in zone 2 (13%, Fig. 5E), suggesting that synapsis is also accelerated in this mutant. However, we found that *pch-2; him-*

Figure 5. *him-3*^{R93Y} does not suppress the acceleration of pairing or synapsis in *pch-2* mutants

A. Cartoon depicting zones for quantification in the *C. elegans* germline. **B.** Meiotic nuclei stained with DAPI (magenta) and HIM-8 (green). Arrows indicate paired nuclei. Scalebar indicates 5 microns. **C.** Quantification of percent nuclei paired in zones 1-6 for *syp-1* (blue), *pch-2;syp-1* (red), *him-3;syp-1* (green) and *pch-2;him-3;syp*-1 (purple) mutant strains. ** indicates p value <0.01. **D.** Meiotic nuclei stained with SYP-1(magenta) and HTP-3 (green). Arrow indicates unsynapsed chromosomes. Scalebar indicates 5 microns. **E.** Quantification of percent nuclei synapsed in zones 1-6 for wildtype (blue), *pch-2* (red), *him-3* (green) and *pch-2;him-3* (purple) mutant strains. ** indicates p value <0.01. **F.** Quantification of percent nuclei synapsed in zones 1-6 for *meDf2/+* (blue), *pch-2;meDf2/+* (red), *him-3;meDf2/+* (green) and *pch-2;him-3;meDf2/+* (purple) mutant strains. Significance was assessed using two-tailed Fisher's exact tests.

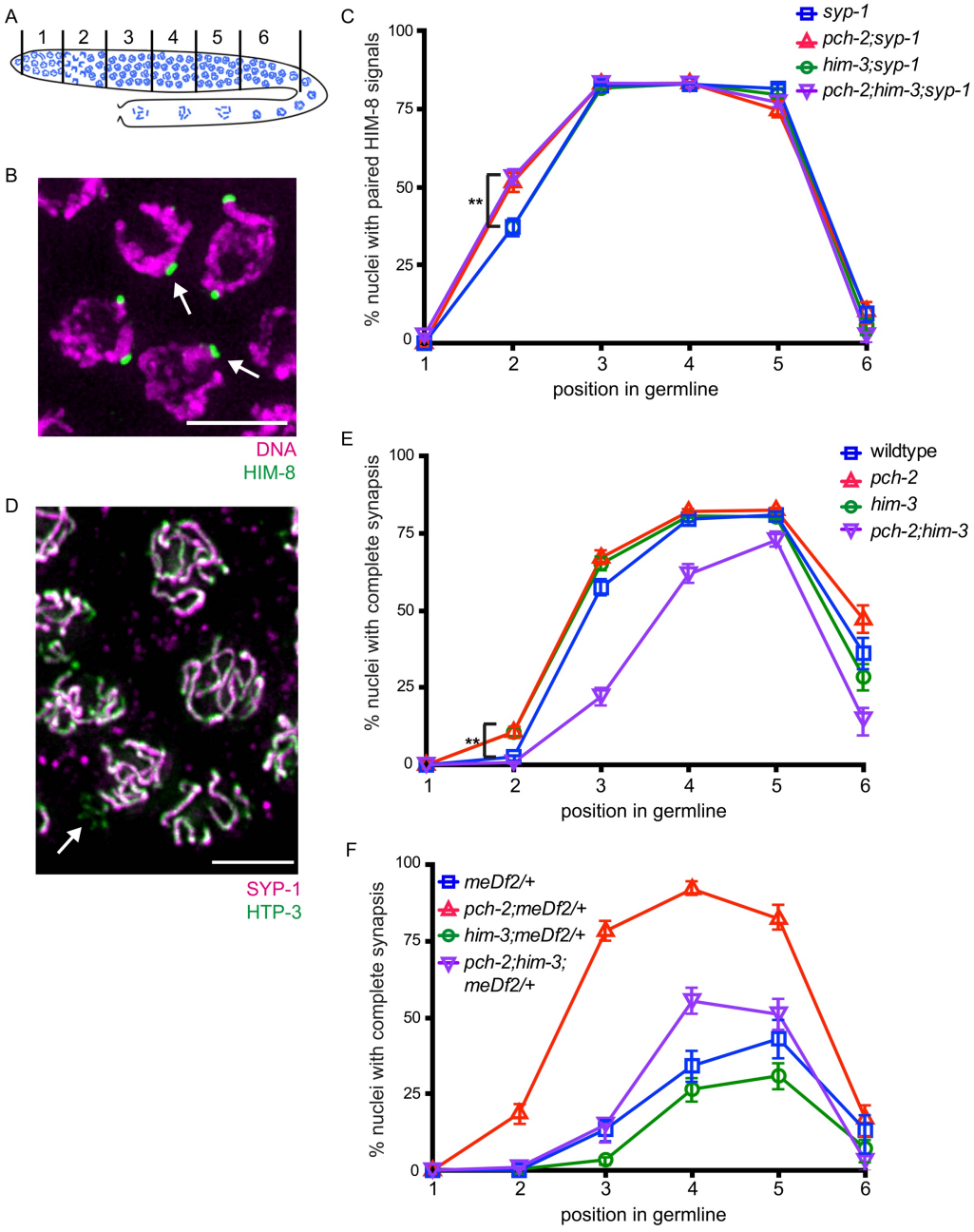
A
1
2
3
4
5
6
B
DNA
HIM-8
D
SYP-1
HTP-3
C
syp-1
pch-2;syp-1
him-3;syp-1
pch-2;him-3;syp-1
% nuclei with paired HIM-8 signals
position in germline
**
E
wildtype
pch-2
him-3
pch-2;him-3
% nuclei with complete synapsis
position in germline
**
F
meDf2/+
pch-2;meDf2/+
him-3;meDf2/+
pch-2;him-3;
meDf2/+
% nuclei with complete synapsis
position in germline

3^{R93Y} double mutants display more severe synapsis defects, where the rate of synapsis is delayed throughout zones 2-5 and these mutants reach only 87% complete synapsis throughout the germline (Fig. 5E). These results demonstrate that PCH-2 and HIM-3 regulate the progression of synapsis independently of each other.

Finally, we further assessed synapsis in *him-3^{R93Y}*, *and pch-2; him-3^{R93Y}* mutants by scoring synapsis in *meDf2* heterozygotes (*meDf2*/+). Similar to our analysis of *htp-3^{H96Y}* mutants, we found that *pch-2;meDf2*/+ double mutants reach 82% complete synapsis in zone 5 compared to 43% for *meDf2*/+ controls (Fig. 5F), suggesting that *pch-2* mutants limit synapsis when PC's are non-functional. *him-3^{R93Y};meDf2*/+ mutants show a reduced level of complete synapsis to 31% in zone 5 (Fig. 5F). Surprisingly, we found that *pch-2; him-3^{R93Y}*;*meDf2*/+ worms triple mutants show a reduced level of synapsis (55%, Fig. 5F) in zone 5 compared to *pch-2;meDf2*/+ double mutants (82%), but the overall level of synapsis is higher compared to *pch-2;htp-3 ^{H96Y};meDf2*/+ triple mutants (22%, Fig. 5F). This provides further support that PCH-2 and HIM-3 both regulate synapsis but accomplish this through independent mechanisms.

Taken together, this indicates that PCH-2 does not act on HIM-3 to regulate pairing or synapsis and suggests that redundancy between these two proteins is unlikely for PCH-2's regulation of these meiotic events.

him-3^{R93Y} does not suppress DNA repair defects in *pch-2* mutants

We next tested whether PCH-2 acts on HIM-3 to regulate DNA repair by scoring RAD-51 foci in N2, *pch-2*, *him-3*^{R93Y} and *pch-2; him-3*^{R93Y} mutants. Similar to our previous results, we found that the average number of RAD-51 foci is lower in *pch-2* mutants (1.96 foci, Fig. 6A) compared to wildtype controls (2.68 foci, Fig. 6A) suggesting that the rate of DNA repair is accelerated in *pch-2* mutants. In *him-3*^{R93Y} single mutants, we found that the average number of RAD-51 foci to be 2.39 foci (Fig. 4B). For *pch-2*;*him-3*^{R93Y} worms, we found that the average number of RAD-51 foci in zone 4 to be 2.18 (Fig. 6A), suggesting that the accelerated rate of DNA repair observed in *pch-2* mutants is not suppressed by the *him-3*^{R93Y} mutation. Overall, this suggests that PCH-2 does not act on HIM-3 to promote DNA repair.

him-3^{R93Y} suppresses crossover recombination defects in *pch-2* mutants

To test whether *pch-2* acts on *him-3* to promote crossover recombination, we scored GFP::COSA-1 foci in wildtype, *pch-2, him-3*^{R93Y} and *pch-2; him-3*^{R93Y} mutant strains. Similar to our previous findings for our HTP-3 experiments (Fig. 6B), we found that *pch-2* mutants had an increase in the number of nuclei with less than 6 GFP::COSA-1 foci (~10%, Fig. 6B) compared to wildtype controls (~3%, Fig. 6B), suggesting a loss of crossover assurance in *pch-2* mutants. Similarly to *pch-2* mutants, we found that there was also an increase of nuclei with less than 6 GFP::COSA-1 foci in *him-3*^{R93Y} mutants compared to wildtype controls (9%, Fig. 6B), suggesting that mutation of this residue in HIM-3 causes a loss of crossover assurance. Surprisingly, we found that

Figure 6. *him-3*^{R93Y} does not suppress DNA repair defects but suppresses crossover defects in *pch-2* mutants

A. Quantification of number of RAD-51 foci in zones 1-6 for wildtype (blue), *pch-2* (red), *him-3* (green) and *pch-2;him-3* (purple) mutant strains. **B.** Quantification of percent nuclei with less than 6 GFP::COSA-1 foci for wildtype, *pch-2*, *him-3*, and *pch-2;him-3* mutant strains. * indicates p value <0.05. ** indicates p value <0.01. **C.** Quantification of percent oocytes with univalents for wildtype, *pch-2*, *him-3*, and *pch-2;him-3* mutant strains. Significance was assessed using Student T-tests.

A

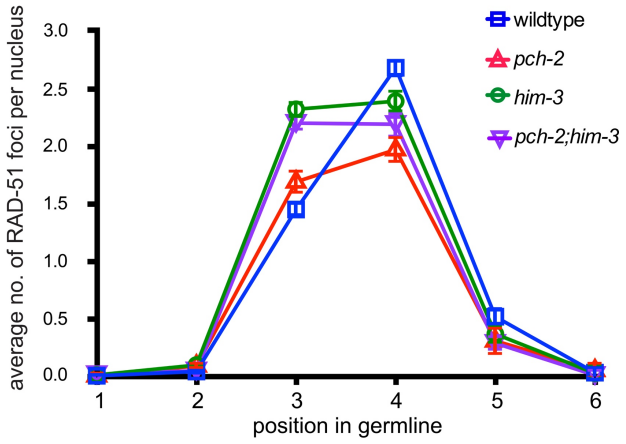
average no. of RAD-51 foci per nucleus
3.0
2.5
2.0
1.5
1.0
0.5
0.0
1
2
3
4
5
6
position in germline
wildtype
pch-2
him-3
pch-2;him-3

B

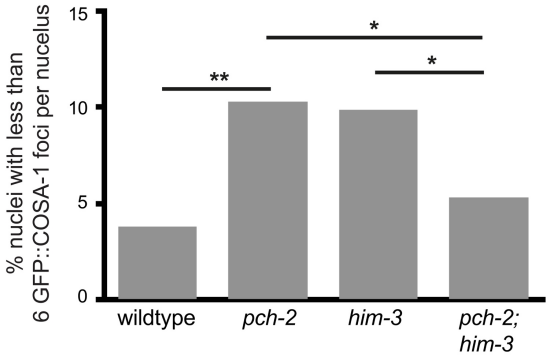
% nuclei with less than 6 GFP::COSA-1 foci per nucelus
15
10
5
0
**
*
*
wildtype
pch-2
him-3
pch-2; him-3

C

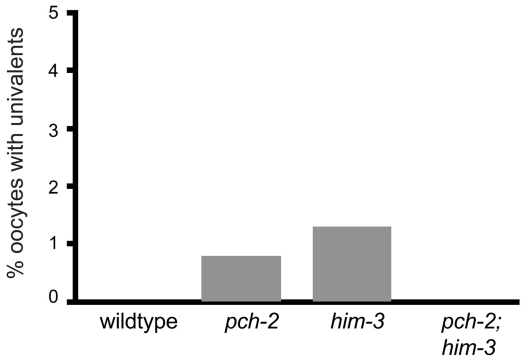
% oocytes with univalents
5
4
3
2
1
0
wildtype
pch-2
him-3
pch-2; him-3

unlike *pch-2;htp-3* ^{H96Y} mutants where the number of nuclei with less than 6 foci is exacerbated (Fig. 3D), *pch-2;him-3*^{R93Y} double mutants have similar levels of nuclei will less than 6 foci to wildtype controls (5%, Fig. 6B). This result illustrates that *him-3*^{R93Y} suppresses *pch-2* mutant crossover recombination defects.

To further test whether PCH-2 acts on HIM-3 to promote crossover recombination, we scored the number of nuclei with univalents in oocytes for each strain. Similar to our previous findings, we found that there was an increase in the percent of nuclei with univalents in *pch-2* mutants compared to wildtype controls (0.8%, Fig. 6C), further suggesting a loss of crossover assurance leading to unlinked homolog pairs. *him-3*^{R93Y} mutants also have an increase in the number of oocytes containing univalents (1.3%, Fig. 6C), supporting our GFP::COSA-1 findings that *him-3*^{R93Y} mutants observe a loss of crossover assurance. For *pch-2; him-3*^{R93Y} double mutants, we found that the increase in univalents observed for either *pch-2* or *him-3*^{R93Y} single mutants is suppressed, where there are no instances of univalents (Fig. 6C).

Taken together, these results are consistent with a model where PCH-2 acts on HIM-3 to promote crossover recombination.

him-3 ^{R93Y} does not affect meiotic progression

We next tested whether *him-3*^{R93Y} mutants affect meiotic progression by performing immunofluorescence against DSB-1 and quantifying the fraction that were DSB-1 positive in wildtype and *him-3*^{R93Y}mutant strains. We found that there was not a significant difference between the number of DSB-1 positive nuclei between wildtype and *him-3*^{R93Y} mutant strains (Fig. 7A), suggesting that this mutation does not affect meiotic progression.

We further tested whether the *him-3*^{R93Y} mutation affected meiotic progression by quantifying the fraction of DSB-1 positive nuclei in *syp-1* and *him-3*^{R93Y}*; syp-1* mutant strains. Similar to our findings for *htp-3*^{H96Y}*,* we found that there was not a significant difference in the number of DSB-1 positive nuclei between *syp-1* and *him-3*^{R93Y}*; syp-1* (Fig. 7B). This result further demonstrates that *him-3* ^{R93Y} does not affect meiotic progression.

htp-1^{G97S} and *htp-1*^{G9TT} both cause a delay in meiotic progression

Our findings suggest that PCH-2 acts on HTP-3 to promote pairing and synapsis, and on HIM-3 to promote crossover formation. We next wanted to test whether PCH-2 acts on the third essential meiotic HORMAD, HTP-1.

Figure 7. *him-3*^{R93Y} does not affect meiotic progression.

A. Quantification of DSB-1 positive meiotic nuclei for wildtype and *him-3*^{R93Y} mutant strains. NS indicates non-significant. **B.** Quantification of DSB-1 positive meiotic nuclei for syp-1 and *him-3*^{R93Y}*;syp-1* mutants. NS indicates non-significant. Statistical significance was assessed using two-tailed Fisher's exact tests.

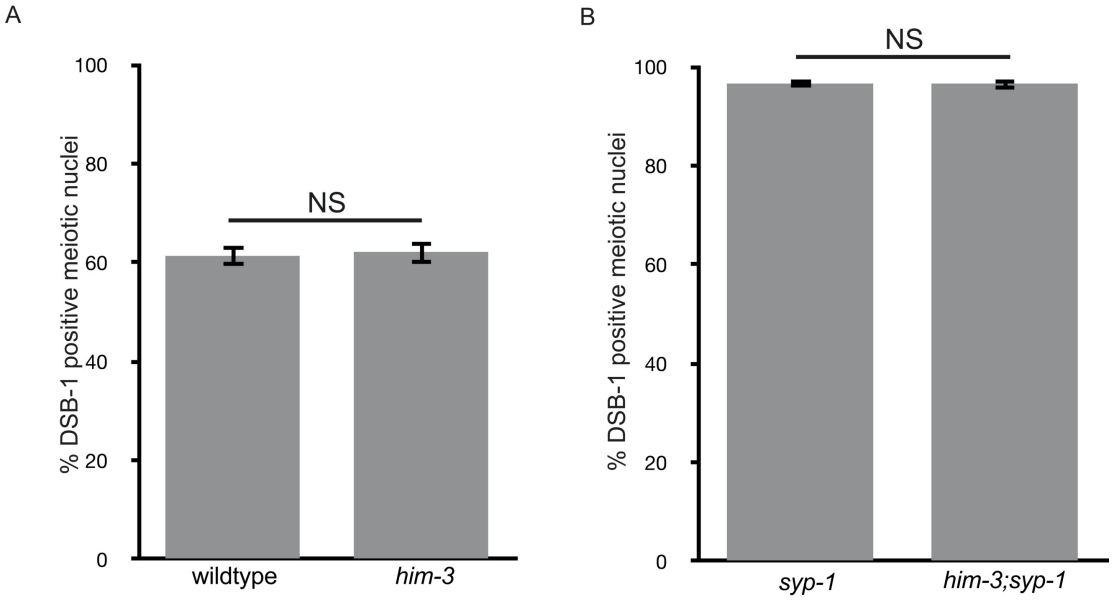

Using CRISPR/Cas9 gene editing, we made an analogous mutation in HTP-1 at glycine 97 and replaced the glycine with a tyrosine (*htp-1*^{G97Y}). However, uponexamining this mutant, we observed a high level of embryonic inevitability and a high incidence of male (HIM) phenotype (data not shown), suggesting that this mutation behaves similarly to a null mutation in *htp-1* where pairing, synapsis and/or recombination are compromised (Silva et al., 2014).

To identify a mutation that would behave similarly in severity to the *htp-3*^{H96Y} and *him-3*^{R93Y} alleles and allow analysis of pairing, synapsis, recombination, and meiotic progression, we performed an allelic series using CRISPR/Cas9 by substituting glycine 27 with amino acids that progressively add steric hindrance at this position (*htp-1*^{G97A}, *htp-1*$^{G97S,\ and}$ *htp-1*^{G97T}). Upon examining these strains, there was a higher incidence of male phenotype associated with each strain (data not shown), suggesting that these mutations cause meiotic defects due to non-disjunction of the X chromosome.

Previous work has shown that mutations within the HORMA domain of HTP-1 cause a delay in meiotic progression (Silva *et al.*, 2014). We then tested whether these mutations similarly cause defects in meiotic progression by performing immunostaining against DSB-1. We quantified the fraction of DSB-1 positive meiotic nuclei in wildtype, *htp-1*^{G97A}, *htp-1*$^{G97S,\ and}$ *htp-1*^{G97T} mutant germlines. Similar to our analysis of DSB-1 in *htp-3*^{H96Y} and *him-3*^{R93Y} mutants, wildtype worms have

~60% of meiotic nuclei that are DSB-1 positive (58%, Fig. 8A). We found that there was not a statistically significant difference in the fraction of DSB-1 positive nuclei between wildtype and *htp-1*^{G97A} mutants (61% Fig. 8A), suggesting that a glycine to alanine substitution at this residue does not cause a defect in meiotic progression. Surprisingly, we found that substituting glycine with either a serine (63%, Fig.8A) or threonine (81%, Fig. 8A) causes a statistically significant increase in the fraction of DSB-1 positive nuclei, suggesting that both of these mutations cause delays in meiotic progression. Overall, this suggests that remodeling of HTP-1 through its HORMA domain potentially contributes to its role in regulating meiotic progression.

Discussion

Meiotic prophase events are tightly coordinated to ensure proper chromosome segregation and prevent aneuploidy, but how these events are temporally coordinated to maintain fidelity throughout meiotic prophase has remained poorly understood. Additionally, the specific mechanism for how PCH-2 regulates fidelity during meiotic prophase remains enigmatic. Here we show genetic evidence to support a model where PCH-2 acts on the meiotic HORMADS to regulate pairing, synapsis and recombination. We find that a mutation in the HORMA domain of HTP-3 (*htp-3*^{H96Y}) suppresses the acceleration of pairing and synapsis that occurs in *pch-2* mutants (Fig. 2C, 2E, 2F), but exacerbates recombination defects (Fig. 3B, 3D and 3F). This provides support for a model where PCH-2 acts on HTP-3 specifically to regulate

Figure 8. *htp-1*^{G97S} and *htp-1*^{G97T} cause defects in meiotic progression.

A. Quantification of DSB-1 positive meiotic nuclei for wildtype, *htp-1*^{G97A}, *htp-1*^{G97S}, and *htp-1*^{G97T} mutant strains. NS indicates non-significant. *** indicates p value <0.001 and **** indicates p value <0.0001 Statistical significance was assessed using two-tailed Fisher's exact tests.

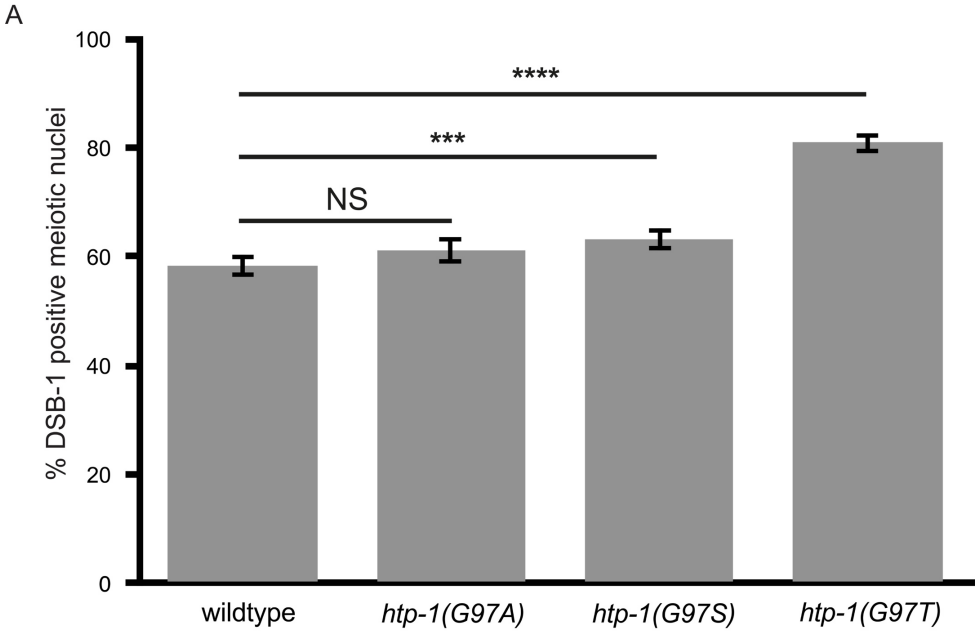

pairing and synapsis but acts independently of HTP-3 to regulate crossover recombination.

Unlike our analysis of *htp-3*^{H96Y} mutants, we find that a corresponding mutation in the HORMA domain of HIM-3 (*him-3*^{R93Y}*)* does not suppress the acceleration of pairing and synapsis associated with *pch-2* mutants. Pairing remains accelerated in *pch-2;him-3* double mutants (Fig. 5B) and severe synapsis defects are also observed in the double mutant background (Fig. 5D), demonstrating that *pch-2* and *him-3*^{R93Y} both regulate synapsis, but potentially accomplish this independently.

We were surprised to find that *him-3*^{R93Y} single mutants undergo an acceleration in synapsis similar to *pch-2* mutants (Fig. 5D). We also observe an initial increase in the number of RAD-51 foci in zone 3 for this strain compared to wildtype worms followed by a rapid decrease in zones 4-6 (Fig. 6A), suggesting *him-3*^{R93Y} mutants also have accelerated DNA repair. These results potentially reflect a role for HIM-3 in regulating the rate of meiotic progression. Whether HIM-3 plays a direct or indirect role in regulating meiotic progression remains an open question.

In contrast to our findings for pairing and synapsis, *him-3*^{R93Y} mutants suppress defects in crossover recombination that are associated with *pch-2* mutants. The number of nuclei with less than 6 GFP::COSA-1 foci is significantly reduced

compared to *pch-2* and *him-3*^{R93Y} single mutants (Fig. 6B) and unlike for either single mutant, univalent are not observed in *pch-2; him-3*^{R93Y} double mutants (Fig. 6C). These results provide support for a model where PCH-2 does not act on HIM-3 to regulate pairing and synapsis but does act on HIM-3 to regulate recombination.

Finally, we show that analogous mutations in the HORMA domain of HTP-1 cause an increase in the number of DSB-1 positive nuclei, suggesting that meiotic progression is delayed due to potential errors in pairing, synapsis and/or recombination. Specifically, a significant delay in meiotic progression was not observed for *htp-1*^{G97A} mutants, but was for *htp-1*^{G97S}*, and htp-1*^{G97T} mutants (Fig. 8A). Substitutions that increase steric hindrance at this residue could potentially disrupt either proper folding of the HORMA domain, or HTP-1's ability to convert between open and closed conformations. Because the *pch-2* null mutation genetically interacts with corresponding mutations made within the same region of HTP-3 and HIM-3, one remaining question would be to test whether mutations in *pch-2* suppress *htp-1*^{G97S} and/or *htp-1*^{G97T}, implicating that PCH-2 and HTP-1 regulate meiotic progression through the same mechanism. While *pch-2* mutations do not cause direct effects on meiotic progression despite having accelerated pairing, synapsis and recombination (Deshong *et al.*, 2014), genetic interactions between *pch-2* and either *htp-1*^{G97S} or *htp-1*^{G97T} mutants could indicate whether or not *pch-2* plays an indirect role in regulating meiotic progression.

Another remaining question is whether or not *htp-1*^{G97S} or *htp-1*^{G97T} mutants cause defects in pairing, synapsis and recombination. While null mutations in HTP-1 cause indirect effects on meiotic prophase events due to misregulation of meiotic progression, missense mutations within the HORMA domain have been shown to cause an increase in non-homologous synapsis (Silva *et al.*, 2014). Whether or not *htp-1*^{G97S} or *htp-1*^{G97T} also cause direct effects on pairing, synapsis or recombination could potentially test whether there is redundancy between HTP-1 and either HTP-3 or HIM-3 to regulate these events.

We propose a model where PCH-2 delegates different meiotic HORMADS to regulate different steps of meiotic prophase. Specifically, we propose that PCH-2 acts on HTP-3 to regulate the rate of pairing and synapsis and acts on HIM-3 to specifically regulate recombination. Because *htp-3*^{H96Y} and *him-3*^{R93Y} mutants do not cause defects in meiotic progression (Fig. 4 and Fig. 7), whether or not PCH-2 delegates HTP-1 to specifically regulate meiotic progression remains an interesting unanswered question.

This model could potentially address why this family of HORMADS has drastically expanded in *C. elegans*, but also why expansion of the HORMADs is observed to be a general feature of meiosis. *Arabidopsis* and mammals have two meiotic HORMADS compared to budding yeast that has a single meiotic HORMAD. HORMADS in plants and mammals play non-redundant roles during meiotic

prophase, so there may be additional evolutionary pressure to create new HORMADS to carry out specific roles throughout meiotic prophase. In contrast to mice, yeast and *Arabidopsis*, synapsis and recombination are not mechanistically linked in *C. elegans* and both events can initiate independently (Dernburg *et al.*, 1998). Designating additional meiotic HORMADS to regulate both initiation of synapsis and recombination could explain why this family has undergone additional gene duplication events in *C. elegans* and why all three meiotic HORMADS remain essential. Therefore, HORMADS as a whole may have evolved to carry out non-redundant roles during meiotic prophase in order to satisfy species specific differences in sexual reproduction.

Finally, whether or not PCH-2 acts directly on meiotic HORMADS remains an important unanswered question. PCH-2 may directly bind meiotic HORMADS on chromosomes to disassemble inappropriate homolog interactions, similar to its molecular mechanism of directly acting on Mad2 for spindle assembly checkpoint regulation. Additional biochemical experiments that investigate how PCH-2 mechanistically interacts with the meiotic HORMADS could offer more insight into how it promotes fidelity during meiosis.

Materials and Methods

Genetics, Worm strains

The C. *elegans* Bristol N2 strain was used as the wildtype strain throughout this study.

The *him-3*^{R93Y}, *htp-1*^{G97A}, *htp-1*^{G97S}, *htp-1*^{G97T}, and *htp-1* ^{G97T}*htp-2* alleles were generated by CRISPR-Cas9 genome editing supplemented with the *dpy-10* co-conversion method (Arribere *et al.*, 2014).

The following guide RNA sequences were used:

dpy-10 sgRNA: 5'GCU ACC AUA GGC ACC ACG AGG UUU UAG AGC UAU GCU 3'

him-3 sgRNA: 5'CGU GUG UCU UCA ACA UUC GAG UUU UAG AGC UAU GCU 3'

htp-1 sgRNA: 5' UCA ACU ACU UCG AAA UGC UGG UUU UAG AGC UAU GCU 3'

The following DNA repair oligonucleotide sequences were used:

dpy-10: 5' CAC TTG AAC TTC AAT ACG GCA AGA TGA GAA TGA CTG GAA ACC GTA CCG CAT GCG GTG CCT ATG GTA GCG GAG CTT CAC ATG GCT TCA GAC CAA CAG CCT AT 3'

him-3^{R93Y}: 5’ GCA TTC CAG AGC AGT GTT CCT GCC GCA AAG CGT GTG TCT TCA ACA TTT GAC GGA TTG TAC GAT GCG ATT CAA CAA GGC TAT TTG CGA GAG TTC GCA ATC GTG TTC TAC AAG 3’

htp-1^{G97A}: 5’ GCT TCA GAA ACC CAC GGT CTA ACC AAA TCG CTC AAC TAC TTC GAA ATG CTG CTG ATG CAA CAA AGG ATG GGT TTC TGA AAG AAG TCT CCC TCG TGA TCA CAA ATA ATG 3’

htp-1^{G97S}: 5’ GCT TCA GAA ACC CAC GGT CTA ACC AAA TCG CTC AAC TAC TTC GAA ATG CTT CAG ATG CAA CAA AGG ATG GGT TTC TGA AAG AAG TCT CCC TCG TGA TCA CAA ATA ATG 3’

htp-1 ^{G97T}: 5’ 5’ GCT TCA GAA ACC CAC GGT CTA ACC AAA TCG CTC AAC TAC TTC GAA ATG CTA CAG ATG CAA CAA AGG ATG GGT TTC TGA AAG AAG TCT CCC TCG TGA TCA CAA ATA ATG 3’

For CRISPR/Cs9 gene editing, all mutations were made in the N2 wildtype strain, with the exception of *htp-1* ^{G97T}*htp-2* that was made in the *htp-2* null mutant background. Injection mixes contained either *htp-1* or *him-3* sgRNA (100 µM final), *dpy-10* sgRNA (100 µM final, (Arribere *et al.*, 2014)), tracrRNA (100 µM final, IDT), purified Cas9 protein (40 µM final), *htp-3* or *him-3* DNA repair oligo (50 µM final, IDT) and *dpy-10* repair oligo (50 µM final, IDT, (Arribere *et al.*, 2014)). Young

adults were injected, recovered and stored at either 15 or 20 degrees. Roller or *dpy* F1's were singled to individual plates seeded with OP50 and screened for presence of the mutant allele by PCR and BspHI restriction digest (*htp-1)* or RsaI restriction digest (*him-3*). Individual F2's were then isolated from F1 plates that contained the allele to identify a homozygous strain.

All mutations were verified by sequencing and strains were backcrossed against wildtype worms three times, with the exception of *htp-1* ^{G97T}*htp-2* that was backcrossed to *htp-2* mutants three times.

Immunofluorescence, Antibodies and Microscopy

Day 1 adult hermaphrodites were dissected 24-28 hours post-late L4 stage and immunostaining and DAPI staining were performed similarly to (Bhalla and Dernburg, 2005). For analyzing bivalents, hermaphrodites were dissected and DAPI stained 48 hours post late L4 stage.

The following primary antibodies were used for this study: rat anti-HIM-8 1:500 (Phillips *et al.*, 2005), guinea pig anti-HTP-3 1:250 (MacQueen *et al.*, 2005), chicken anti-HTP-3 1:250 (MacQueen *et al.*, 2005), rabbit anti-SYP-1 1:500 (MacQueen *et al.*, 2002), rabbit anti-HTP-1 1:400 (Martinez-Perez *et al.*, 2008), rabbit anti-RAD-51 1:250 (Novus Biologicals), guinea pig anti-DSB-1 1:250 (Stamper et al., 2013), mouse anti-GFP 1:100 (Invitrogen).

The following secondaries were used for this study: Alexa 488 anti-guinea pig (Invitrogen), Alexa 488 anti-rabbit (Invitrogen), Alexa 488 anti-mouse (Invitrogen), Cy3 anti-rabbit (Jackson Immunochemicals), Cy3 anti-rat (Jackson Immunochemicals), Cy3 anti-guinea pig (Jackson Immunochemicals), and Cy5 anti-chicken (Jackson Immunochemicals). All secondary antibodies were used at a 1:500 dilution.

To visualize meiotic nuclei and bivalents, DAPI was used at a dilution of 1:10,000.

All images were acquired using a DeltaVision Personal DV system (Applied Precision) equipped with a 100X N.A. 1.40 oil-immersion objective (Olympus), resulting in an effective XY pixel spacing of 0.064 or 0.040 μm. Three-dimensional image stacks were collected at 0.2-μm Z-spacing and processed by constrained, iterative deconvolution. Image scaling and analysis were performed using functions in the softWoRx software package. Projections were calculated by a maximum intensity algorithm. Composite images were assembled and some false coloring was performed with ImageJ.

Quantification of pairing, synapsis, RAD-51 foci, GFP::COSA-1 foci, and DSB-1 positive nuclei was performed as in (Giacopazzi *et al.*, 2020) with a minimum of three germlines per genotype. To determine statistical significance, student T-tests were performed.

CHAPTER 3: The conserved AAA-ATPase PCH-2^{TRIP13} regulates spindle checkpoint strength

Abstract

Spindle checkpoint strength is dictated by the number of unattached kinetochores, cell volume and cell fate. We show that the conserved AAA-ATPase, PCH-2/TRIP13, which remodels the checkpoint effector Mad2 from an active conformation to an inactive one, controls checkpoint strength in *C. elegans*. Having previously established that this function is required for spindle checkpoint activation, we demonstrate that in cells genetically manipulated to decrease in cell volume, PCH-2 is no longer required for the spindle checkpoint or recruitment of Mad2 at unattached kinetochores. This role is not limited to large cells: the stronger checkpoint in germline precursor cells also depends on PCH-2. PCH-2 is enriched in germline precursor cells and this enrichment relies on conserved factors that induce asymmetry in the early embryo. Finally, the stronger checkpoint in germline precursor cells is regulated by CMT-1, the ortholog of p31^{comet}, which is required for both PCH-2's localization to unattached kinetochores and its enrichment in germline precursor cells. Thus, PCH-2, likely by regulating the availability of inactive Mad2 at and near unattached kinetochores, governs checkpoint strength. This requirement may be particularly relevant in oocytes and early embryos enlarged for developmental competence, cells that divide in syncytial tissues and immortal germline cells**.**

Introduction

To prevent the missegregation of chromosomes and the production of daughter cells with an incorrect number of chromosomes, the spindle checkpoint (also called the spindle assembly checkpoint or the mitotic checkpoint) monitors whether chromosomes are attached to the spindle via kinetochores. If kinetochores fail to attach properly, this checkpoint delays the cell cycle to promote error correction and prevent aneuploidy. Despite its critical role, the duration of the cell cycle delay, defined as the strength of the spindle checkpoint, can be highly variable. This variability can be controlled by the number of unattached kinetochores (Collin et al., 2013), cell volume (Galli and Morgan, 2016; Kyogoku and Kitajima, 2017), and cell fate (Galli and Morgan, 2016; Gerhold et al., 2018).

The spindle checkpoint response initiates with the recruitment of Mad1 and Mad2 at unattached kinetochores (Chen et al., 1998; Chen et al., 1996; Li and Benezra, 1996; Sironi et al., 2001), which catalyzes the production of a Mitotic Checkpoint Complex (MCC). The MCC enforces a checkpoint arrest by inhibiting the Anaphase Promoting Complex/Cyclosome (APC/C) and preventing cell cycle progression (Sudakin et al., 2001). Formation of the MCC is driven by conformational changes in Mad2, which can exist in an open conformation (O-Mad2) or a closed conformation (C-Mad2) (Luo et al., 2002; Luo et al., 2004; Sironi et al., 2002). Mad2 is in the closed conformation in the Mad1/Mad2 tetramer recruited to unattached kinetochores. C-Mad2 in the tetramer acts as a template to convert additional soluble O-Mad2 to C-

Mad2, which can be assembled into the MCC (De Antoni et al., 2005; Fava et al., 2011; Simonetta et al., 2009; Sironi *et al.*, 2001). Thus, unattached kinetochores act as a platform for MCC assembly. This soluble signal generated by unattached kinetochores effectively tunes the spindle checkpoint response: the length of the cell cycle delay imposed by the checkpoint is governed by the ratio of unattached kinetochores producing MCC, and its ability to inhibit the APC, to cytoplasmic volume (Collin *et al.*, 2013; Dick and Gerlich, 2013; Galli and Morgan, 2016; Kyogoku and Kitajima, 2017).

PCH-2/TRIP13 is a hexameric AAA+ ATPase that remodels HORMA domain-containing proteins, a group that includes Mad2 (Aravind and Koonin, 1998; Rosenberg and Corbett, 2015; Vader, 2015). Biochemical and structural studies have shown that PCH-2 converts C-Mad2 to O-Mad2 (Alfieri *et al.*, 2018; Brulotte *et al.*, 2017; Ye *et al.*, 2015). TRIP13 works with the adaptor protein $p31^{comet}$ to extract C-Mad2 from the MCC and promote its disassembly, permitting the activation of the APC/C and silencing the checkpoint (Alfieri *et al.*, 2018; Brulotte *et al.*, 2017; Eytan *et al.*, 2014; Miniowitz-Shemtov *et al.*, 2015; Wang *et al.*, 2014; Ye *et al.*, 2015). In addition to this role, we and others have shown that PCH-2/TRIP13 is essential for spindle checkpoint activation in *C. elegans* and human cells (Ma and Poon, 2016; Ma and Poon, 2018; Nelson *et al.*, 2015; Yost *et al.*, 2017). PCH-2 is present at unattached kinetochores (Nelson *et al.*, 2015; Tipton et al., 2012; Wang *et al.*, 2014) and is required to robustly localize Mad2, but not Mad1, to unattached kinetochores

(Nelson *et al.*, 2015; Yost *et al.*, 2017). A major implication of this work is that O-Mad2 can be limiting during checkpoint activation and PCH-2/TRIP13 plays a central role in ensuring its availability (Ma and Poon, 2018).

Based on a genetic interaction between the *C. elegans* ortholog of p31^{comet}, CMT-1, and PCH-2, we had previously proposed that PCH-2 disassembles a CMT-1/Mad2 complex to promote checkpoint signaling, similar to its role during checkpoint silencing (Nelson *et al.*, 2015). However, recent data from mammalian systems, in which loss of p31^{comet} does not suppress the requirement for TRIP13 (Ma and Poon, 2016; Ma and Poon, 2018; Nelson *et al.*, 2015; Yost *et al.*, 2017) and TRIP13's function becomes essential for checkpoint activity only when O-Mad2 becomes limiting (Ma and Poon, 2018), suggest elaborations to this model in *C. elegans*. Given that p31^{comet} binds Mad2, specifically C-Mad2, throughout the cell cycle (Date et al., 2014; Xia et al., 2004) and that CMT-1 is required to maintain Mad2 protein levels (Nelson *et al.*, 2015), we hypothesize that CMT-1's binding of Mad2 plays two roles in *C. elegans*: to stabilize Mad2 and sequester it until required for checkpoint function. In the absence of CMT-1, more O-Mad2 is available despite the reduction in total protein levels, thus making PCH-2 partially dispensable and explaining the genetic suppression. This model differs from our understanding of TRIP13 and p31^{comet} in cultured human cells (see Table 1), potentially because of the rapidity of embryonic cell cycles, the fact that relative levels of C and O-Mad2 may vary between systems and the observation that most Mad2 in cultured human cells is

present as O-Mad2 (Luo *et al.*, 2004). Further, it highlights the importance of studying spindle checkpoint function in developmentally-relevant model organisms.

This model, however, raises another question: if the primary role of PCH-2/TRIP13 is to guarantee enough O-Mad2 is available for checkpoint activation and this role can be dispensable when enough O-Mad2 is available, is there a reason for PCH-2/TRIP13 to localize to unattached kinetochores (Nelson *et al.*, 2015; Tipton *et al.*, 2012; Wang *et al.*, 2014)? One possible answer comes from our analysis of *cmt-1* mutant worms. In addition to its role as a PCH-2 adapter (Ye *et al.*, 2015) and stabilizing Mad2 protein levels (Nelson *et al.*, 2015), CMT-1 is also required to localize PCH-2 to unattached kinetochores during the spindle checkpoint response and generate a robust spindle checkpoint response in AB cells (Nelson *et al.*, 2015). Overexpressing Mad2 does not suppress the partial defect in spindle checkpoint activation in *cmt-1* mutants (Nelson *et al.*, 2015), suggesting that the defect in spindle checkpoint strength is not because of reduced Mad2 protein levels but the inability to localize PCH-2 to unattached kinetochores.

Here, we test this possibility and show that PCH-2 controls spindle checkpoint strength in *C. elegans*. Despite being essential for the spindle checkpoint in the large somatic, or AB, cell of the 2-cell embryo (Nelson *et al.*, 2015), PCH-2 becomes dispensable for the spindle checkpoint and partially dispensable for Mad2 recruitment at unattached kinetochores as AB cells are genetically manipulated to become

smaller. The requirement for PCH-2 in promoting spindle checkpoint strength is also observed as cells decrease in size during embryogenesis and in germline precursor, or P_1 cells, which have a stronger checkpoint than their similarly sized somatic counterparts. PCH-2 is enriched in P_1 cells and this enrichment depends on conserved regulators of embryonic polarity, PAR-1 and PAR-6. Further, the stronger checkpoint in P_1 cells also relies on the *C. elegans* ortholog of $p31^{comet}$, CMT-1, indicating that CMT-1's ability to enrich PCH-2 in P_1 cells, in addition to its role in localizing PCH-2 to unattached kinetochores, contributes to a stronger checkpoint. We propose that PCH-2, and its mammalian ortholog TRIP13, ensure a robust spindle checkpoint response and proper chromosome segregation by regulating the availability of O-Mad2 at and near unattached kinetochores. This role may be specifically relevant in scenarios where maintaining genomic stability is particularly challenging, such as in oocytes and early embryos enlarged for developmental competence, cells that divide in a syncytium and germline cells that maintain immortality.

Results

PCH-2 becomes dispensable for the spindle checkpoint response in somatic cells experimentally reduced in size

In the large somatic, or AB, cell of the *C. elegans* 2-cell embryo, PCH-2 is essential for spindle checkpoint activation (Nelson *et al.*, 2015). To further assess the requirements for PCH-2 function, we manipulated the cell volume of embryos, and

thus AB cells, experimentally by performing RNA interference (RNAi) against *ani-2*. *ani-2* encodes a germline specific anillin whose depletion generates oocytes and, after fertilization, embryos, of varying size (Maddox et al., 2005) (Figure 9A). We monitored the length of mitosis in these AB cells, using the time between nuclear envelope breakdown (NEBD) to the onset of cortical contractility (OCC) as markers for the entry into and exit from mitosis, respectively (Essex et al., 2009). We then correlated the length of mitosis to cytoplasmic volume. RNAi of *ani-2* did not affect normal cell cycle progression in control, *pch-2*, or *mad-1* mutants (Figure 10A), indicating that reducing cytoplasmic volume did not affect mitotic timing in AB cells. (In *C. elegans*, the genes that encode Mad1 and Mad2 are *mdf-1* and *mdf-2*, respectively. To avoid confusion, we will use *mad-1* and *mad-2*).

We performed double depletion of *ani-2* and *zyg-1* to induce the spindle checkpoint response in control embryos, *pch-2*, and *mad-1* mutants. ZYG-1 is essential for centrosome duplication and after the first embryonic division, its depletion generates monopolar spindles (O'Connell et al., 2001) and unattached kinetochores (Essex *et al.*, 2009) (Figure 9B). Consistent with previous reports, as AB cells decreased in cell volume the length of the cell cycle delay, an indicator of spindle checkpoint strength, increased in control embryos (Galli and Morgan, 2016; Gerhold *et al.*, 2018) (Figure 9C, Videos 1 and 2). Surprisingly, as *pch-2* mutants decreased in size, the spindle checkpoint response more closely resembled that of control AB cells than *mad-1*

Figure 9: PCH-2 becomes dispensable for the spindle checkpoint response in somatic cells experimentally reduced in size

(A) Images of wildtype-sized and small ani-2RNAi 2-cell embryos. Scale bar indicates 5 μm. (B) Cartoon of wildtype-sized and small ani-2RNAi 2-cell embryos treated with zyg-1RNAi. (C) Mitotic timing, as measured from nuclear envelope breakdown (NEBD) to the onset of cortical contractility (OCC), in AB cells of control, pch-2 and mad-1 mutant embryos plotted against cell volume. Lines represent least-squares regression models with 95% confidence intervals (gray shaded areas) for each set of data. Equations and p values indicating whether slopes are significantly non-zero for each model are: ani-2RNAi;zyg-1RNAi (blue): $y=-1.117x+11.15$ and $p < 0.0001$; pch-2;ani-2RNAi;zyg-1RNAi (red): $y=-1.264x+10.50$ and $p < 0.0001$; mad-1;ani-2RNAi;zyg-1RNAi (green): $y=-0.1709x+4.468$ and $p = 0.4197$. (D) Data from (C) partitioned into three categories: wild-type sized embryos (more than 5 x 103 μm3), medium sized embryos (between 3.3 x 103 μm3 and 5 x 103 μm3) and small embryos (less than 3.3 x 103 μm3). Error bars are 95% confidence intervals. In all graphs, a * indicates a p value < 0.05, ** indicates a p value < 0.01 and *** a p value < 0.0001.

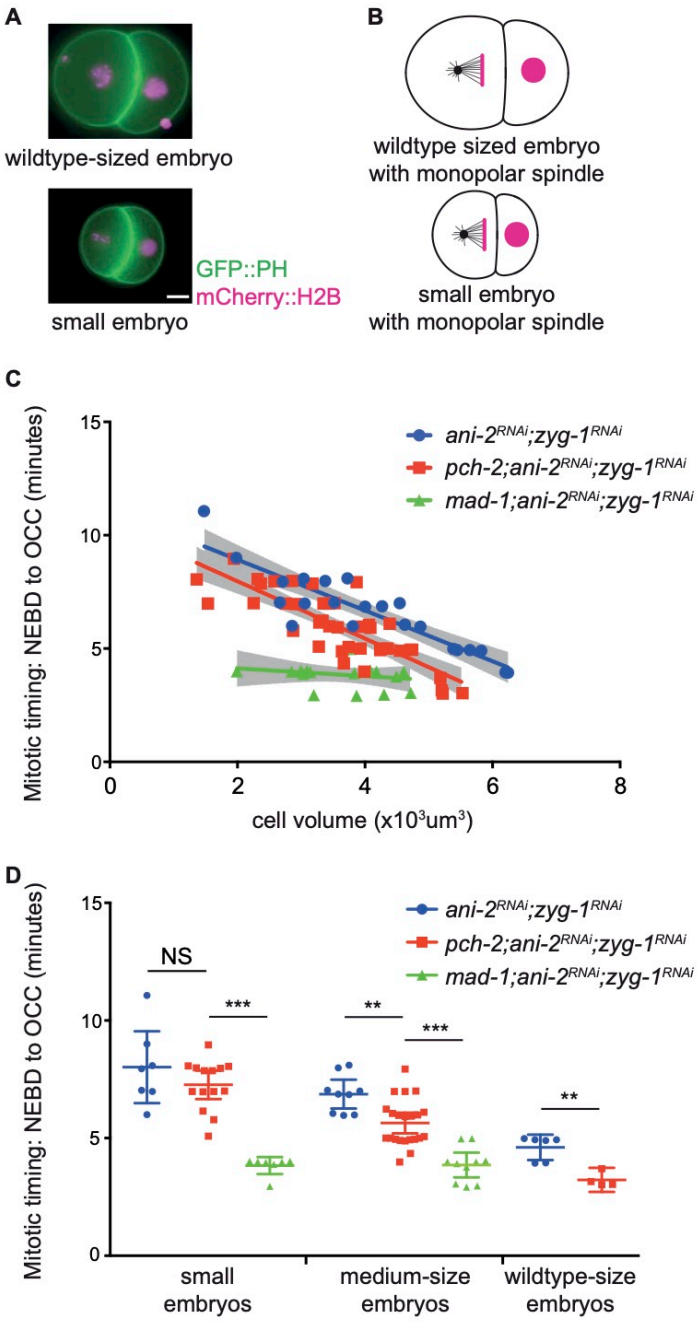
A
wildtype-sized embryo
GFP::PH
mCherry::H2B
small embryo
B
wildtype sized embryo
with monopolar spindle
small embryo
with monopolar spindle
C
Mitotic timing: NEBD to OCC (minutes)
cell volume (x10³um³)
ani-2RNAi;zyg-1RNAi
pch-2;ani-2RNAi;zyg-1RNAi
mad-1;ani-2RNAi;zyg-1RNAi
D
Mitotic timing: NEBD to OCC (minutes)
NS
***
**
***
**
small embryos
medium-size embryos
wildtype-size embryos

Figure 10: The mitotic delay observed in pch-2;ani-2RNAi;zyg-1RNAi small cells is a spindle checkpoint response.

Cartoon of control and ani-2RNAi 2-cell embryos (A) and an ani-2RNAi;zyg-1RNAi 2-cell embryo (B). Mitotic timing in AB cells plotted against cell volume, during unperturbed mitosis (C) and in the presence of monopolar spindles. (D). Lines represent least-squares regression models for each set of data. For (C) equations and p values indicating whether slopes are significantly non-zero for each model are: ani-2RNAi (blue): y=-9.744x10-3x+3.001 and p = 0.6073; pch-2;ani-2RNAi (red): y=-0.1315x+3.503 and p = 0.0483; mad-1;ani-2RNAi (green): y=-0.2944x+4.247 and p = 0.0251. In (D), 95% confidence intervals are indicated by gray shaded areas and equations and p values indicating whether slopes are significantly non-zero for each model are: san-1;ani- 2RNAi;zyg-1RNAi P1 (blue): y=-0.4136x+5.535 and p = 0.1885; san-1;pch-2;ani-2RNAi;zyg-1RNAi P1 (red): y=-0.3541x+5.647 and p = 0.0643. The regression model of pch-2;ani-2RNAi;zyg-1RNAi embryos from Figure 1C is indicated by the opaque red line in (D) for comparison.

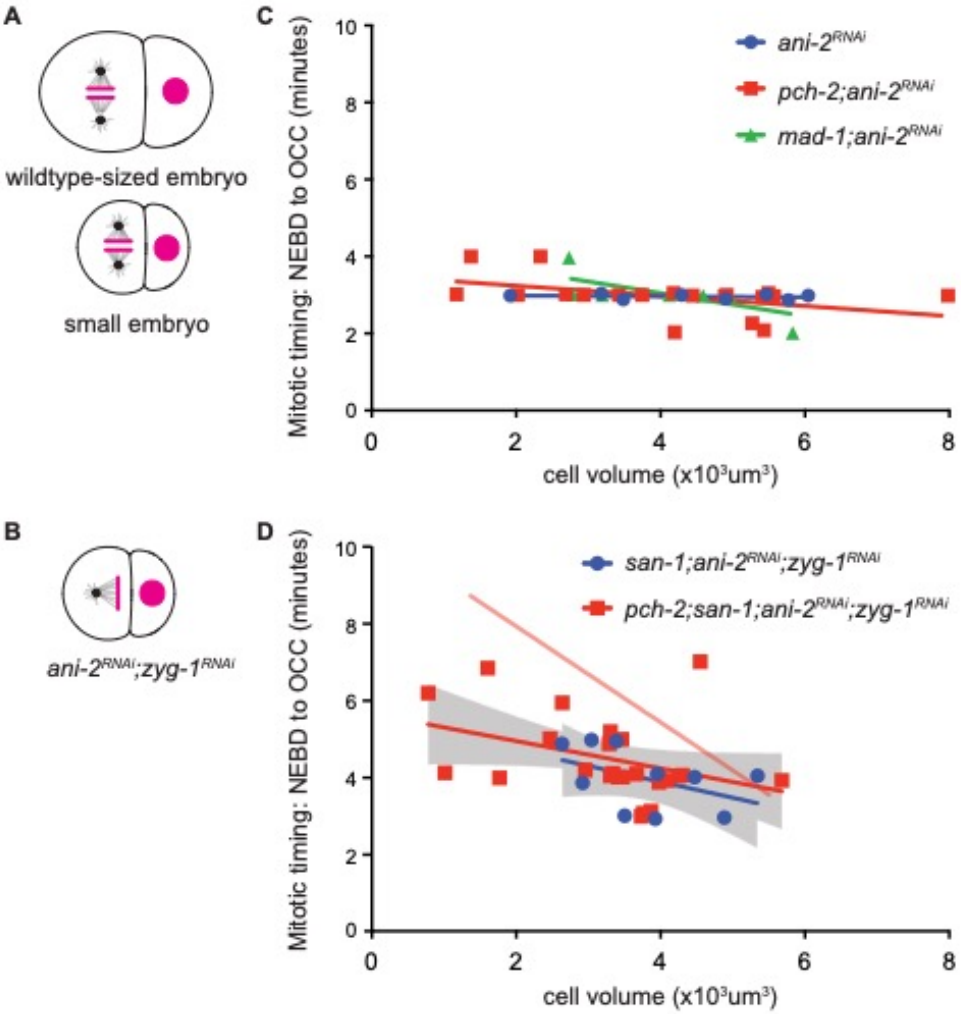
A
wildtype-sized embryo
small embryo
B
ani-2RNAi;zyg-1RNAi
C
Mitotic timing: NEBD to OCC (minutes)
cell volume (x10³um³)
ani-2RNAi
pch-2;ani-2RNAi
mad-1;ani-2RNAi
D
Mitotic timing: NEBD to OCC (minutes)
cell volume (x10³um³)
san-1;ani-2RNAi;zyg-1RNAi
pch-2;san-1;ani-2RNAi;zyg-1RNAi

mutants (Figure 9C, Videos 3 and 4). *mad-1* mutant embryos appear more sensitive to *ani-2* RNAi treatment and we had difficulty recovering any wild-type sized *mad-1* embryos. There was no significant difference between the slopes of the regression analysis of control and *pch-2* mutant data (p value = 0.4664), while the slopes between the regression analysis of *pch-2* and *mad-1* mutant data were significantly different (p value = 0.0007).

To make these comparisons more clear, we binned our data. By our measurements, control AB cells ranged from 5 to 6 x 10^3 μm^3. Therefore, we classified AB cells greater than 5 x 10^3 μm^3 as wildtype sized. *ani-2^{RNAi};zyg-1^{RNAi}* AB cells that were wildtype sized exhibited mitotic delays while similarly sized *ani-2^{RNAi};zyg-1^{RNAi};pch-2* mutants produced no checkpoint response (Figure 9D). These data are consistent with what we have reported previously and report here for *zyg-1^{RNAi}* and *zyg-1^{RNAi};pch-2* AB cells (Nelson *et al.*, 2015) and Figure 16). The remaining cells, which ranged from 1.5 x 10^3 μm^3 to 5 x 10^3 μm^3 were partitioned equally into two classes: medium sized embryos were between 3.3 x 10^3 μm^3 and 5 x 10^3 μm^3 and small embryos were between 1.5 x 10^3 μm^3 and 3.3 x 10^3 μm^3. When partitioned into these two classes, medium-sized cells in *pch-2* mutants produced a checkpoint response intermediate between similarly sized control and *mad-1* mutant cells while small *pch-2* cells had a robust checkpoint, when compared to control and *mad-1* mutant cells (Figure 9D).

We verified that the mitotic delay observed in *pch-2* AB cells was a legitimate spindle checkpoint response by monitoring mitotic timing after performing double depletion of *ani-2* and *zyg-1* in *san-1* and *pch-2;san-1* mutant embryos. SAN-1 is the *C. elegans* ortholog of the essential spindle checkpoint factor, Mad3 (Nystul et al., 2003) (Figure 10B). There was no significant difference between the slopes of the regression analysis of *san-1* and *pch-2;san-1* data (p value = 0.8813) and the slopes of each model were not statistically different than zero (Figure 10B). However, we observed a slight increase in the length of the cell cycle as cells got smaller in *san-1* mutants, potentially reflecting that the spindle checkpoint in *C. elegans* is composed of two independent branches (Essex *et al.*, 2009). Altogether, these data allow us to draw two important conclusions: First, the requirement for PCH-2 during spindle checkpoint activation is proportional to cell volume in AB cells with monopolar spindles. And second, since we observe similar mitotic timing in small *pch-2* mutant AB cells as in small control cells (Figure 9D), PCH-2 does not appear to affect spindle checkpoint silencing in *C. elegans*.

MAD-2 recruitment is partially restored to unattached kinetochores in *pch-2* somatic cells experimentally reduced in size

We showed that PCH-2 is required for robust recruitment of Mad2 at unattached kinetochores during spindle checkpoint activation in AB cells of 2-cell embryos (Nelson *et al.*, 2015). Therefore, we tested whether the checkpoint induced delay we

observed in small *ani-2*^{RNAi}*;zyg-1*^{RNAi}*;pch-2* AB cells was accompanied by increased recruitment of GFP::MAD-2 at unattached kinetochores. We quantified GFP::MAD-2 recruitment at unattached kinetochores in pseudo-metaphase in control animals and *pch-2* mutants treated with *ani-2* and *zyg-1* RNAi (Figure 11A) and plotted GFP::MAD-2 fluorescence against cell volume (Figure 11B). Surprisingly, the regression analysis for control AB cells had a positive slope, suggesting that less GFP::MAD-2 is required at unattached kinetochores for spindle checkpoint function as these cells became smaller (Figure 11B). This was despite similar levels of soluble GFP::MAD2 around mitotic chromosomes after NEBD in both genetic backgrounds (Figures 12A and 12B). We observed that the regression analysis of GFP::MAD-2 fluorescence at unattached kinetochores in *pch-2;ani-2*^{RNAi}*;zyg-1*^{RNAi} AB cells exhibited a negative slope, showing improved GFP::MAD-2 recruitment to unattached kinetochores as cells got smaller. However, the amount of GFP::MAD-2 was typically lower in fluorescence intensity than *ani-2*^{RNAi}*;zyg-1*^{RNAi} control cells (Figure 11B). Therefore, our experiments demonstrate that MAD-2 recruitment is partially restored to unattached kinetochores in *pch-2* mutant somatic cells experimentally reduced in size.

Figure 11: MAD-2 recruitment is partially restored to unattached kinetochores in pch-2 mutant somatic cells experimentally reduced in size

(A) Cartoon and images of GFP::MAD-2 recruitment to unattached kinetochores in AB cells of control and pch-2 AB cells treated with ani-2 and zyg-1 RNAi. Scale bar indicates 1 μm. (B) Quantification of kinetochore bound GFP::MAD-2 in control and pch-2 AB cells plotted against cell volume. Lines represent least-squares regression models with 95% confidence intervals (gray shaded areas) for each set of data. Equations and p values indicating whether slopes are significantly non-zero for each model are: ani-2RNAi;zyg-1RNAi (blue): y=1.531x+5.024 and p = 0.0115; pch-2;ani-2RNAi;zyg-1RNAi (red): y=-1.384x+7.911 and p = 0.0384.

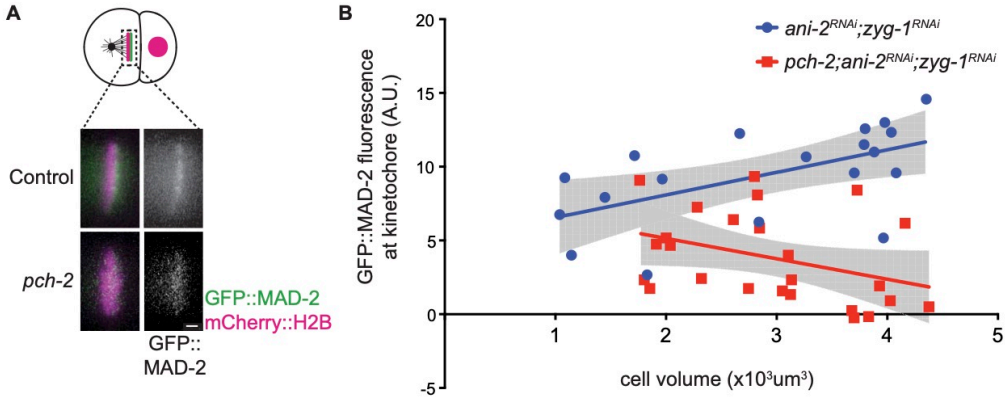

Figure 12: There is no difference in GFP::MAD-2 fluorescence around mitotic chromosomes in ani-2RNAi;zyg-1RNAi embryos and pch-2;ani-2RNAi;zyg-1RNAi AB cells.

(A) Images of MAD-2::GFP in AB cells of control ani-2RNAi;zyg-1RNAi embryos or pch-2;ani- 2RNAi;zyg-1RNAi embryos after NEBD. Scale bar indicates 5 μm. (B) Quantification of GFP::MAD- 2 fluorescence around mitotic chromosomes in AB cells of control and pch-2 embryos plotted against cell volume.

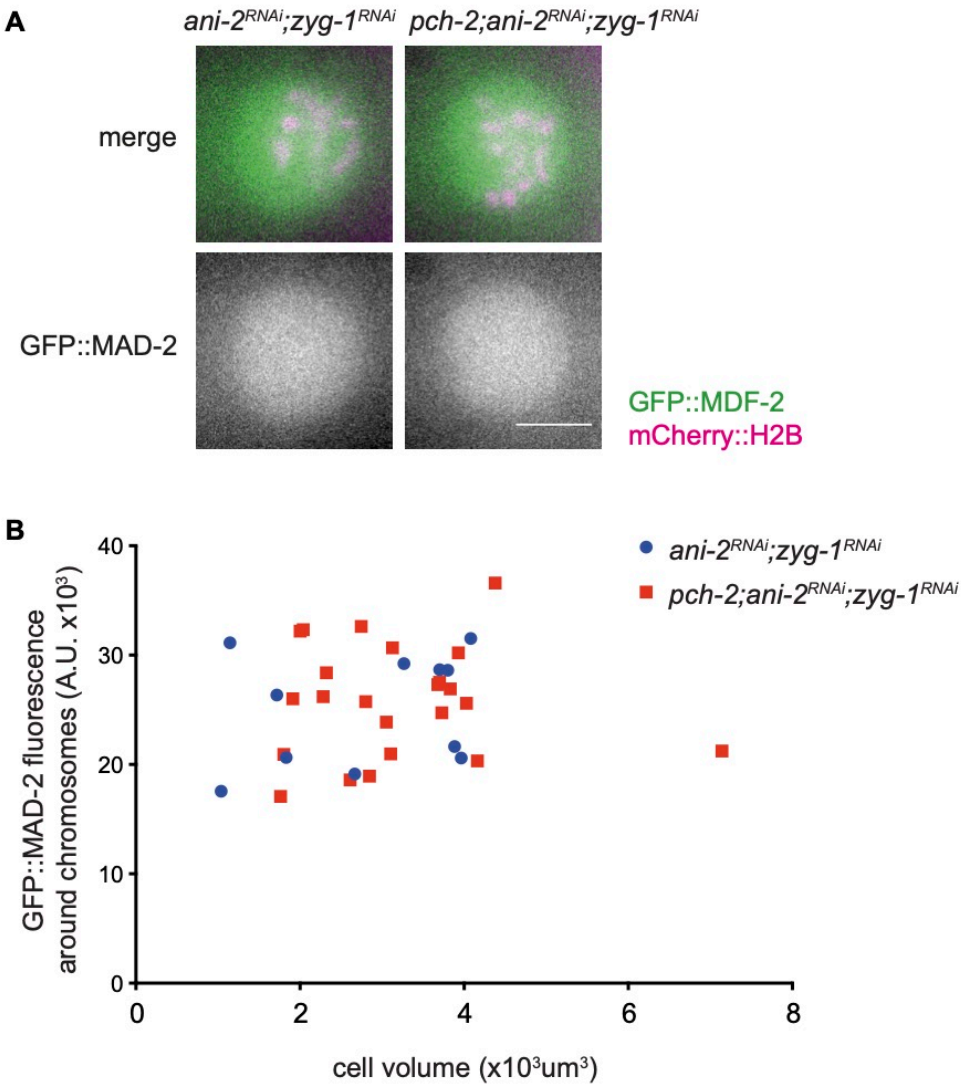
A
ani-2RNAi;zyg-1RNAi
pch-2;ani-2RNAi;zyg-1RNAi
merge
GFP::MAD-2
GFP::MDF-2
mCherry::H2B
B
ani-2RNAi;zyg-1RNAi
pch-2;ani-2RNAi;zyg-1RNAi
GFP::MAD-2 fluorescence around chromosomes (A.U. x10³)
cell volume (x10³um³)
0
10
20
30
40
0
2
4
6
8

MAD-2 dosage controls checkpoint strength

C. elegans meiotic nuclei in the germline exist in a syncytium and cellularize after completing meiotic prophase. Knockdown of *ani-2* affects this cellularization event, resulting in a loss of cytoplasmic volume after nuclei are fully formed (Maddox *et al.*, 2005). MAD-2 is localized to the nucleus and nuclear envelope in these oocytes (Bohr et al., 2015; Lawrence et al., 2015) (Figure 13A). Since embryonic nuclear size is not affected by *ani-2* RNAi (Figure 14), we reasoned that as cells are genetically manipulated to decrease in cell volume, the absolute amount of Mad2 protein is likely to remain constant but its concentration increases. Given that TRIP13 function is dispensable for checkpoint activation when O-Mad2 is readily available in human cells (Ma and Poon, 2018), we reasoned that something similar might be happening in *C. elegans* embryos. Specifically, we hypothesized that an increase in concentration of Mad2, and O-Mad2 in particular, may explain the reduced requirement for PCH-2 in *ani-2*^{RNAi};*zyg-1*^{RNAi} small AB cells (Figure 13B).

To test this possibility, we initially attempted to directly visualize O-Mad2 in *C. elegans* embryos. Unfortunately, we were unable to perform this experiment with a commercial antibody (data not shown). Further, we could not directly probe total Mad2 concentration as cells decrease in volume upon treatment with *ani-2* RNAi because GFP::MAD-2 does not localize to the nucleus and instead localizes in the cytoplasm until NEBD (Essex *et al.*, 2009; Nelson *et al.*, 2015), making it an inaccurate reporter for this assay. Instead, we tested whether reducing Mad2 dosage

Figure 13: MAD-2 dosage controls checkpoint strength

(A) Immunostaining of MAD-2 and nuclear pore complex components (NPCs) shows MAD-2 localized in the nucleus and at the nuclear envelope during interphase. Scale bar indicates 5 µm. (B) Model depicting how a decrease in cell volume might result in an increase in the local concentration of O-Mad2 in ani-2RNAi;zyg-1RNAi embryos, in contrast to zyg-1RNAi embryos. (C) Mitotic timing, as measured from nuclear envelope breakdown (NEBD) to the onset of cortical contractility (OCC), in AB cells of control and mad-2/+ mutant embryos plotted against cell volume. Lines represent least-squares regression models with 95% confidence intervals (gray shaded areas) for each set of data. Equations and p values indicating whether slopes are significantly non-zero for each model are: control (dark purple): y=-1.302x+8.477 and p = 0.0002; mad-2/+ (light purple): y=-0.3171x+4.402 and p = 0.0395.

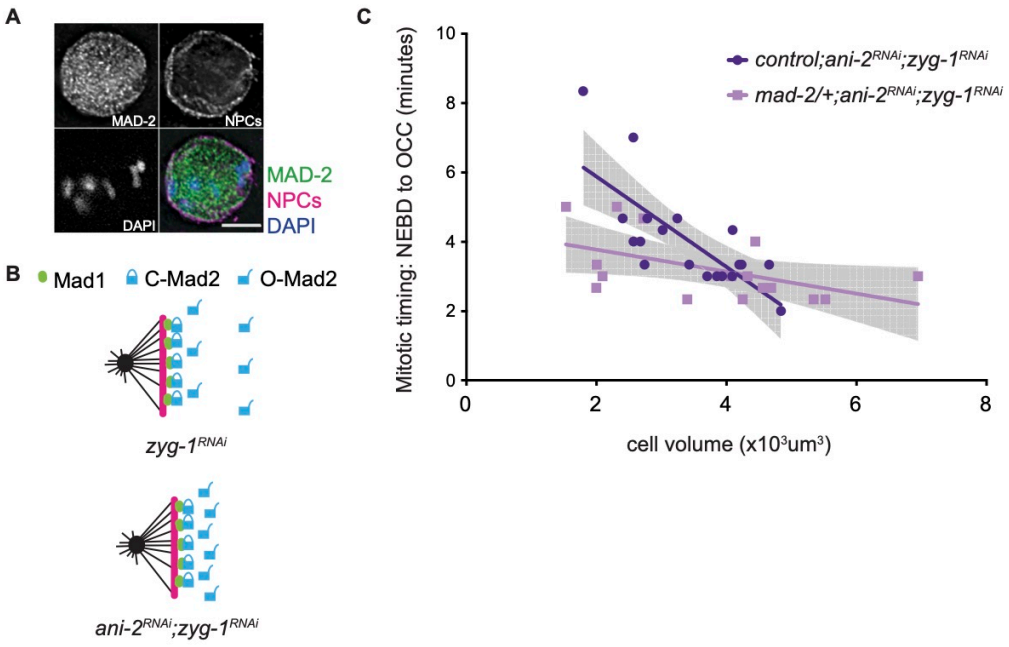

Figure 14: Nuclear volume does not scale with cell volume in ani- 2RNAi 2-cell embryos.

(A) Images of a large (top) and small (bottom) AB cell of ani-2RNAi embryos. The nuclear area is indicated with a dashed yellow line. Scale bar indicates 5 μm. (B) Nuclear area plotted against cell volume.

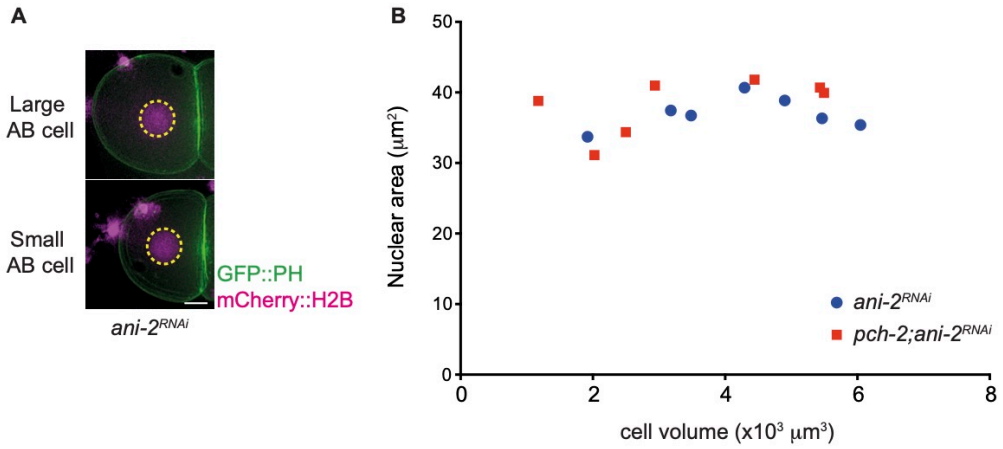

affected checkpoint strength. We hypothesized that if Mad2 concentration influences checkpoint strength, reducing it by half should attenuate checkpoint strength in comparison to control animals. We performed double depletion of *ani-2* and *zyg-1* by RNAi in *mad-2* heterozygotes. Indeed, *mad-2* heterozygotes exhibited stronger spindle checkpoint strength as cells became smaller. However, the increase in spindle checkpoint strength was less robust than control cells (Figure 13C). The slopes of the linear regressions for both control and *mad-2* heterozygotes were significantly non-zero, unlike similar experiments with *mad-1* and *san-1* homozygotes (Figures 9B and 10D). Therefore, spindle checkpoint strength depends on MAD-2 dosage.

We wondered whether the decrease in Mad2 protein levels might restore the reliance on PCH-2 in small embryos. However, *pch-2;mad-2/+* double mutants exhibited a substantial decrease in the production and viability of embryos, preventing us from performing these experiments: *pch-2;mad-2/+* double mutants produced broods that were 14% of control animals and only 1% of these embryos were viable. Further, *pch-2;mad-2* double mutants could not be recovered from *pch-2;mad-2/+* mothers, a genetic interaction that we did not observe when we generated *pch-2;mad-1* double mutants (Bohr *et al.*, 2015) or *pch-2;san-1* double mutants (Figure 10B). Worms with mutations in some spindle checkpoint mutants often display defects in fertility, viability and development (Kitagawa and Rose, 1999; Lara-Gonzalez et al., 2019; Stein et al., 2007). Thus, in addition to MAD-2 dosage controlling checkpoint strength, it collaborates with PCH-2 to promote *C. elegans* fertility and viability.

PCH-2 affects spindle checkpoint strength during embryogenesis

During embryogenesis, cell volume decreases and spindle checkpoint strength increases (Galli and Morgan, 2016; Gerhold *et al.*, 2018). Given that the requirement for PCH-2 is proportional to cell volume in 2-cell embryos treated with *ani-2* RNAi, we assessed the role for PCH-2 in spindle checkpoint activation as cells decreased in size during normal embryogenesis.

We initially performed these experiments in embryos treated with nocodazole, which depolymerizes microtubules and induces spindle checkpoint activation in a manner similar to when cells have monopolar spindles (Galli and Morgan, 2016; Gerhold *et al.*, 2018). We permeabilized embryos by performing *perm-1* RNAi (Carvalho et al., 2011) and treated these embryos with nocodazole. Since we could not reliably visualize OCC in these dividing embryos, we measured mitotic timing from nuclear envelope break down (NEBD) to decondensation of chromosomes (DECON) in cells of the AB lineage. These cells in control embryos exhibited a longer mitotic delay in 16-cell than in 4-cell embryos (Figure 15A), verifying that the spindle checkpoint increases in strength as cells decrease in volume during embryogenesis (Galli and Morgan, 2016; Gerhold *et al.*, 2018). As a control, we performed the same experiment in *san-1* mutants and did not detect a mitotic delay when these embryos were treated with nocodazole (Figure 15A). Cells in 4-cell *pch-2* mutant embryos treated with nocodazole showed greater variability in cell cycle timing than *san-1* mutants but the average was not significantly different (Figure 15A). However, cells

Figure 15: PCH-2 regulates spindle checkpoint strength during embryogenesis

(A) Mitotic timing, as measured from nuclear envelope breakdown (NEBD) to decondensation of chromatin (DECON), in control, pch-2 and san-1 mutant embryos treated with perm-1 RNAi and DMSO or nocodazole at different developmental stages (4- and 16-cell embryos). (B) Mitotic timing in control and pch-2 mutant embryos overexpressing GFP::MAD-2 and treated with perm-1 RNAi and either DMSO or nocodazole at different developmental stages (4- and 16-cell embryos). (C) Mitotic timing in zyg-1ts and pch-2;zyg-1ts mutant embryos at different developmental stages (2-, 4- and 8-cell embryos). All error bars are 95% confidence intervals.

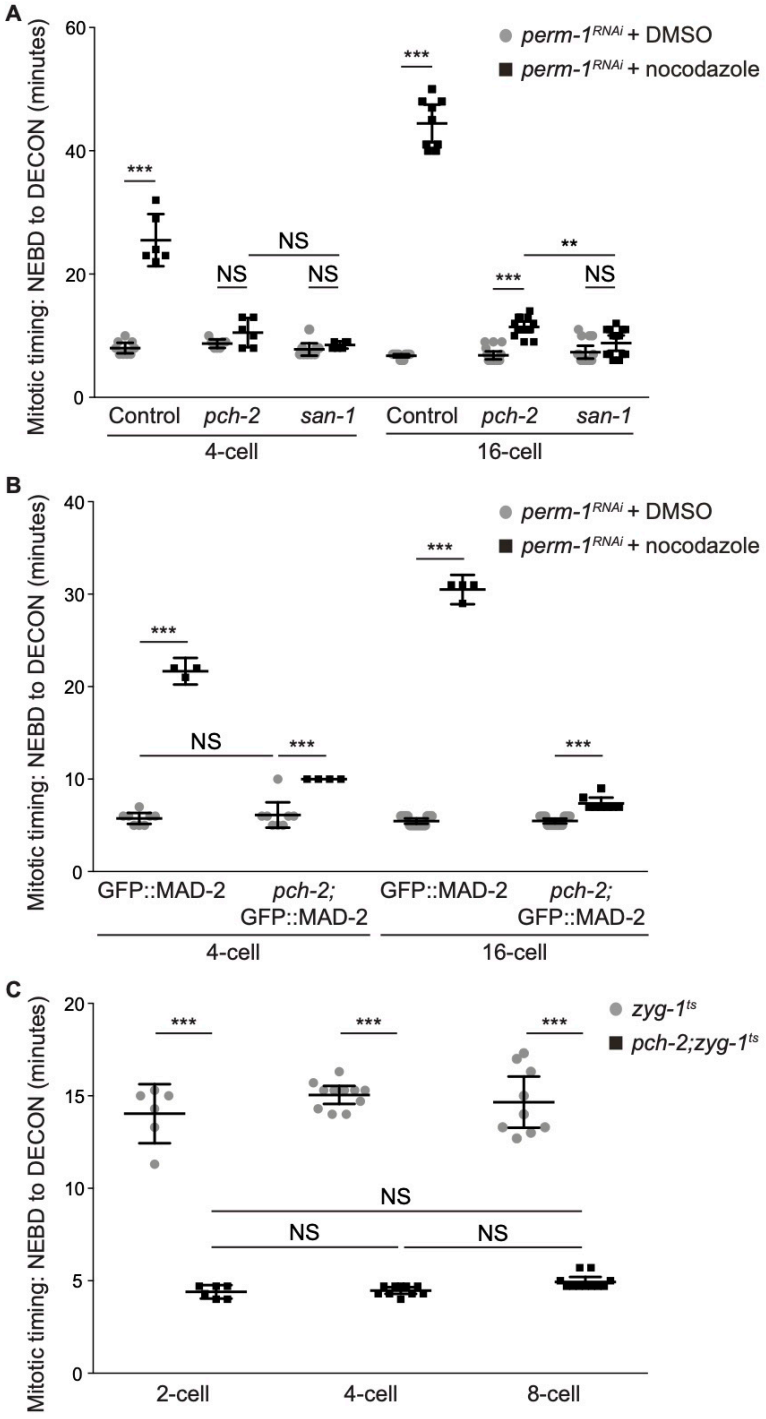
A
Mitotic timing: NEBD to DECON (minutes)
perm-1RNAi + DMSO
perm-1RNAi + nocodazole
***
***
NS
NS
NS
***
**
NS
Control
pch-2
san-1
Control
pch-2
san-1
4-cell
16-cell
B
Mitotic timing: NEBD to DECON (minutes)
perm-1RNAi + DMSO
perm-1RNAi + nocodazole
***
***
NS
***
***
GFP::MAD-2
pch-2; GFP::MAD-2
GFP::MAD-2
pch-2; GFP::MAD-2
4-cell
16-cell
C
Mitotic timing: NEBD to DECON (minutes)
zyg-1ts
pch-2;zyg-1ts
***
***
***
NS
NS
NS
2-cell
4-cell
8-cell

in the AB lineage in 16-cell *pch-2* mutant embryos treated with nocodazole exhibited a slight but significant cell cycle delay when compared to similar cells in *pch-2* mutants treated with DMSO and *san-1* mutants treated with nocodazole. Thus, as cells of the AB lineage naturally decrease in cell size to 16 cell embryos, *pch-2* mutants treated with nocodazole exhibit some delay of the cell cycle, albeit not as prolonged as control embryos, consistent with a defect in spindle checkpoint strength.

Given our hypothesis that Mad2 dosage might contribute to spindle checkpoint strength, particularly in *pch-2* mutants, we tested if a subtle increase in MAD-2 protein levels would suppress the defect in spindle checkpoint function or strength in *pch-2* mutant embryos. The presence of a GFP::MAD-2 transgene, in addition to endogenous MAD-2, results in about 2.5 times more MAD-2 in worms. This slight overexpression generates a normal spindle checkpoint response in control AB cells and can bypass the requirement for checkpoint components MAD-3 or BUB-3 (Essex et al., 2009), but not PCH-2 (Nelson et al., 2015) in AB cells of 2-cell embryos with monopolar spindles. Overexpression of MAD-2 did not affect the checkpoint response in 16-cell *pch-2* embryos (Figure 15B). However, in contrast to our results in 4-cell *pch-2* mutant embryos treated with nocodazole (Figure 15A), we found that overexpression of MAD-2 in cells of the AB lineage of 4-cell *pch-2* embryos produced cell cycle delays when compared to the same cells in embryos treated with DMSO. Again, these delays were not as dramatic as control cells overexpressing GFP::MAD-2 (Figure 15B) but were significant, allowing us to conclude that slight

overexpression of Mad2 partially restores checkpoint function to *pch-2* mutants as cells of the AB lineage decrease in size during embryogenesis, at least in 4-cell embryos.

Given that we activated the spindle checkpoint in *ani-2*^{RNAi} embryos by generating monopolar spindles (Figures 9C and 13C), we also formally tested whether *pch-2* mutant embryos with monopolar spindles exhibited defects in checkpoint strength, particularly in very early embryogenesis. We used a fast acting temperature sensitive allele of *zyg-1* (*zyg-1*^{ts}) (O'Rourke et al., 2011) to activate the spindle checkpoint in developing embryos with 2, 4 and 8 cells. We shifted embryos at different stages of development, verified the appearance of monopolar spindles and measured mitotic timing from NEBD to DECON. In control *zyg-1*^{ts} mutant embryos, we observed a delay in mitotic timing in cells from the AB lineage and this delay only became marginally longer as embryos had more cells (Figure 15C), similar to previous reports (Gerhold *et al.*, 2018). In stark contrast to our *ani-2*^{RNAi} experiments, the mitotic timing observed in *pch-2;zyg-1*^{ts} mutant embryos was the same in AB cells of 2-cell, 4-cell and 8-cell embryos and significantly reduced in comparison to *zyg-1*^{ts} embryos. Thus, similar to our results with 4-cell *pch-2* mutant embryos treated with nocodazole, *pch-2* mutants exhibit no cell cycle delay in the presence of monopolar spindles in AB cells in 2-cell, 4-cell and 8-cell embryos. However, additional considerations may make direct comparisons between our *ani-2*^{RNAi}*;zyg-1*^{RNAi} experiments and *zyg-1*^{ts} embryos difficult (see Discussion).

PCH-2 is responsible for the stronger spindle checkpoint in the germline lineage

Cell fate is another important determinant of spindle checkpoint strength. In *C. elegans* embryos, the spindle checkpoint is stronger in germline precursor cells than similarly sized somatic counterparts (Galli and Morgan, 2016; Gerhold *et al.*, 2018). However, as we observed with AB cells (Nelson *et al.*, 2015), PCH-2 is essential for the spindle checkpoint in wildtype-sized P_1 cells (Figure 16). Therefore, having established that PCH-2 becomes dispensable for the spindle checkpoint as 2-cell embryos are genetically manipulated to become smaller (Figures 9C and D), we tested whether PCH-2 contributed to the stronger spindle checkpoint in P_1 cells of 2-cell embryos treated with *ani-2* RNAi (Figures 16 and 17). Consistent with other reports (Galli and Morgan, 2016; Gerhold *et al.*, 2018), when we performed double depletion of *ani-2* and *zyg-1* in control embryos and monitored mitotic timing, we observed P_1 cells with similar volumes as AB cells exhibiting a longer cell cycle delay (Figures 17A and 16B, Videos 5 and 6). Further, the regression analysis that best fit control P_1 data is significantly different and steeper than that of control AB cells (p value < 0.0001), indicating that variables in addition to cell volume contribute to the spindle checkpoint strength in germline precursor cells. When we knocked down both *ani-2* and *zyg-1* in *pch-2* mutant embryos, we no longer observed a significant difference (p value $= 0.9096$) between the slopes of the regression analysis of P_1 and AB cells (Figures 17B and 16B, Videos 7 and 8), indicating that PCH-2 is responsible for the stronger checkpoint in P_1 cells.

Figure 16: PCH-2 is required for the spindle checkpoint in the germline lineage.

(A) Mitotic timing of control and pch-2 mutant embryos during unperturbed divisions or in the presence of monopolar spindles. Data for control embryos is the same as Figure 7B. Error bars indicate 95% confidence intervals.

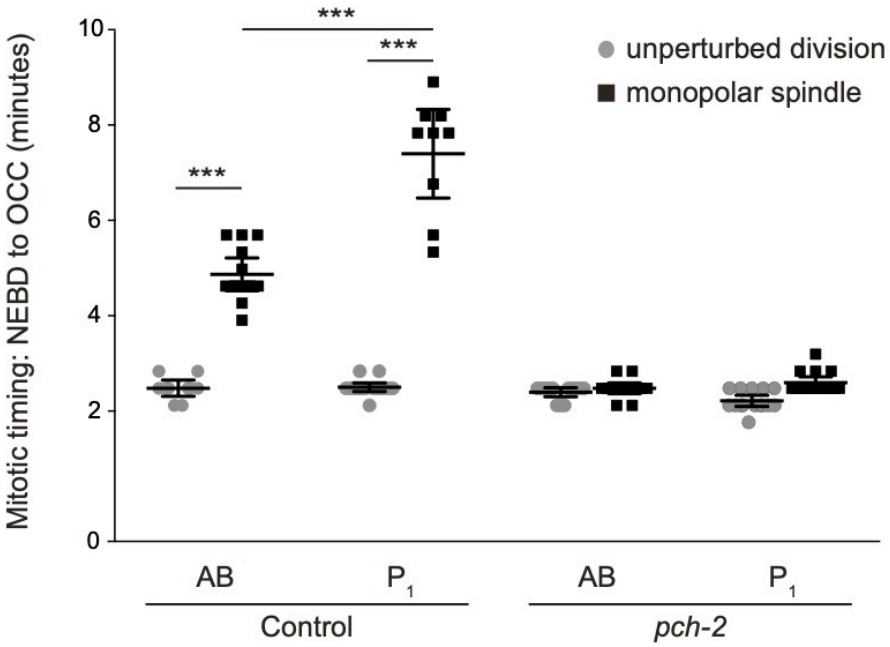

Figure 17: PCH-2 is responsible for the stronger spindle checkpoint in the germline lineage

Mitotic timing, as measured from nuclear envelope breakdown (NEBD) to the onset of cortical contractility (OCC), in AB and P1 cells plotted against cell volume in control ani-2RNAi;zyg-1RNAi embryos (A) or pch-2;ani-2RNAi;zyg-1RNAi (B) embryos. Lines represent least-squares regression models with 95% confidence intervals (gray shaded areas) for each set of data. Equations and p values indicating whether slopes are significantly non-zero for each model are: ani-2RNAi;zyg-1RNAi AB (dark blue): $y=-1.117x+11.15$ and $p < 0.0001$; ani-2RNAi;zyg-1RNAi P1 (light blue): $y=-8.047x+32.27$ and $p = 0.0021$; pch-2;ani-2RNAi;zyg-1RNAi AB (red): $y=-1.264x+10.50$ and $p < 0.0001$; pch-2;ani-2RNAi;zyg-1RNAi P1 (pink): $y=-1.218x+7.75$ and $p = 0.0125$. Data for AB cells in both control and pch-2 mutants is the same as in Figure 1C. (C) Mitotic timing of AB and P1 cells in control, pch-2 and mad-1 mutants during unperturbed divisions. Error bars are 95% confidence intervals.

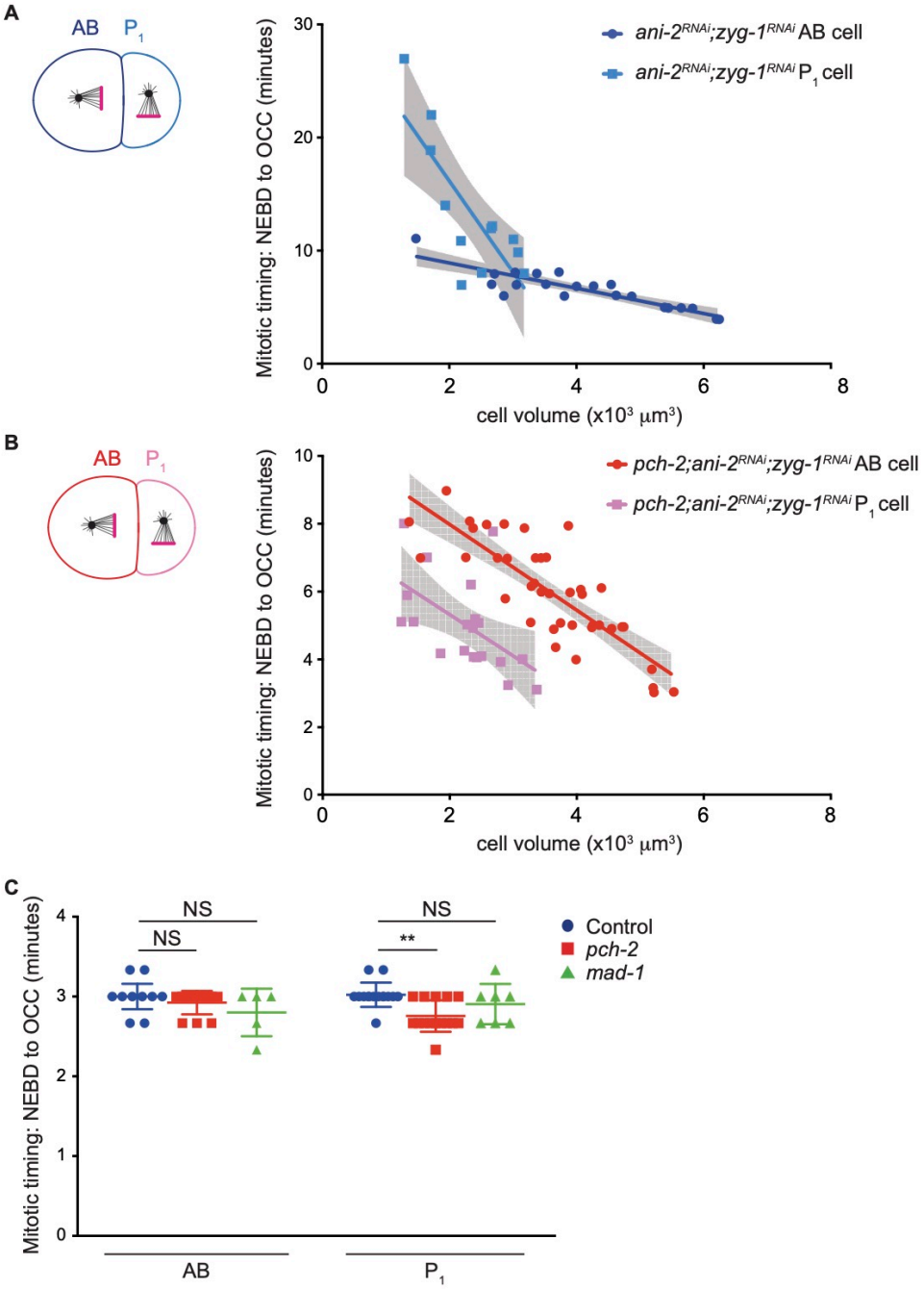
A
AB
P1
Mitotic timing: NEBD to OCC (minutes)
cell volume (x10³ μm³)
ani-2RNAi;zyg-1RNAi AB cell
ani-2RNAi;zyg-1RNAi P1 cell
B
AB
P1
Mitotic timing: NEBD to OCC (minutes)
cell volume (x10³ μm³)
pch-2;ani-2RNAi;zyg-1RNAi AB cell
pch-2;ani-2RNAi;zyg-1RNAi P1 cell
C
Mitotic timing: NEBD to OCC (minutes)
NS
NS
NS
**
Control
pch-2
mad-1
AB
P1

We observed that cell cycle timing was faster in *pch-2* mutant P_1 cells than similarly sized *pch-2* mutant AB cells after treatment with *ani-2* and *zyg-1* RNAi (Figures 17B and 16B). We wondered if embryonic germline precursor cells might rely on some spindle checkpoint proteins for normal mitotic timing, analogous to mitotically dividing stem cells in the *C. elegans* germline (Gerhold et al., 2015) and similar to mammalian cultured cells (Ma and Poon, 2016; Meraldi et al., 2004; Rodriguez-Bravo et al., 2014). To address this, we measured normal mitotic timing in AB and P_1 cells of both control and *pch-2* mutant embryos. We found that while normal mitotic timing is unaffected by mutation of *pch-2* in AB cells, *pch-2* mutant P_1 cells go through mitosis significantly faster than control P_1 cells (Figure 17C), thus providing an explanation for the faster cell cycle timing in *pch-2* mutant P_1 cells with the same cell volume as *pch-2* mutant AB cells after treatment with *ani-2* and *zyg-1* RNAi. We saw a decrease in the cell cycle timing of P_1 cells in *mad-1* mutants but this was not significantly different than control P_1 cells (Figure 17C).

PCH-2's enrichment in P_1 cells depends on PAR-1 and PAR-6

Cell fate is driven by the asymmetric distribution of various determinants between somatic and germline lineages during early divisions of the *C. elegans* embryo (Rose and Gonczy, 2014). Since we found that PCH-2 promoted the spindle checkpoint strength in both AB and P_1 cells, but even more dramatically in P_1 cells, we asked if PCH-2 was regulated differently between these cells. First, we tested whether PCH-

2::GFP could also support the stronger checkpoint in P_1 cells. We treated embryos expressing PCH-2::GFP with *zyg-1* RNAi and evaluated mitotic timing in both AB and P_1 cells using chromosome decondensation as a marker for mitotic exit. P_1 cells expressing PCH-2::GFP had full checkpoint function, exhibiting a mitotic delay longer than AB cells also expressing PCH-2::GFP and not significantly different than control P_1 cells treated with *zyg-1* RNAi (Figure 18A).

Previous transcriptome analysis of PCH-2 did not reveal asymmetric enrichment of PCH-2 mRNA between AB and P_1 cells (Tintori et al., 2016). We tested whether PCH-2::GFP exhibited differences in protein levels between AB and P_1 cells. First, we assessed whether PCH-2::GFP was more enriched in pseudo-metaphase at unattached kinetochores in P_1 than AB cells. We quantified PCH-2::GFP fluorescence at unattached kinetochores in both AB and P_1 cells of embryos treated with *zyg-1* RNAi but did not detect any difference between the two cell types (Figures 19A and B). Similarly, we did not detect any difference in GFP::MAD-2 recruitment at unattached kinetochores between AB and P_1 cells in *zyg-1*^{RNAi} embryos (Figures 19C and D).

Checkpoint factors, including MAD-2 and PCH-2, form a diffuse "cloud" around mitotic chromosomes after NEBD, even during normal cell cycles (Essex *et al.*, 2009; Nelson *et al.*, 2015). We wondered if PCH-2::GFP fluorescence in this cloud might

Figure 18: PCH-2's enrichment around mitotic chromosomes in P1 cells depends on PAR-1

(A) Mitotic timing of control embryos and embryos expressing PCH-2::GFP during unperturbed divisions or in the presence of monopolar spindles. (B) Cartoon and images of PCH-2::GFP localization around mitotic chromosomes in AB and P1 cells of 2-cell embryos. Scale bar indicates 5 μm. (C) Quantification of PCH-2::GFP fluorescence in AB and P1 cells. (D) Cartoon and images of PCH-2::GFP localization around mitotic chromosomes in AB and P1 cells of control RNAi and par-1RNAi 2-cell embryos. (E) Quantification of PCH-2::GFP fluorescence in AB and P1 cells of par-1RNAi embryos. All error bars are 95% confidence intervals. NS indicates not significant.

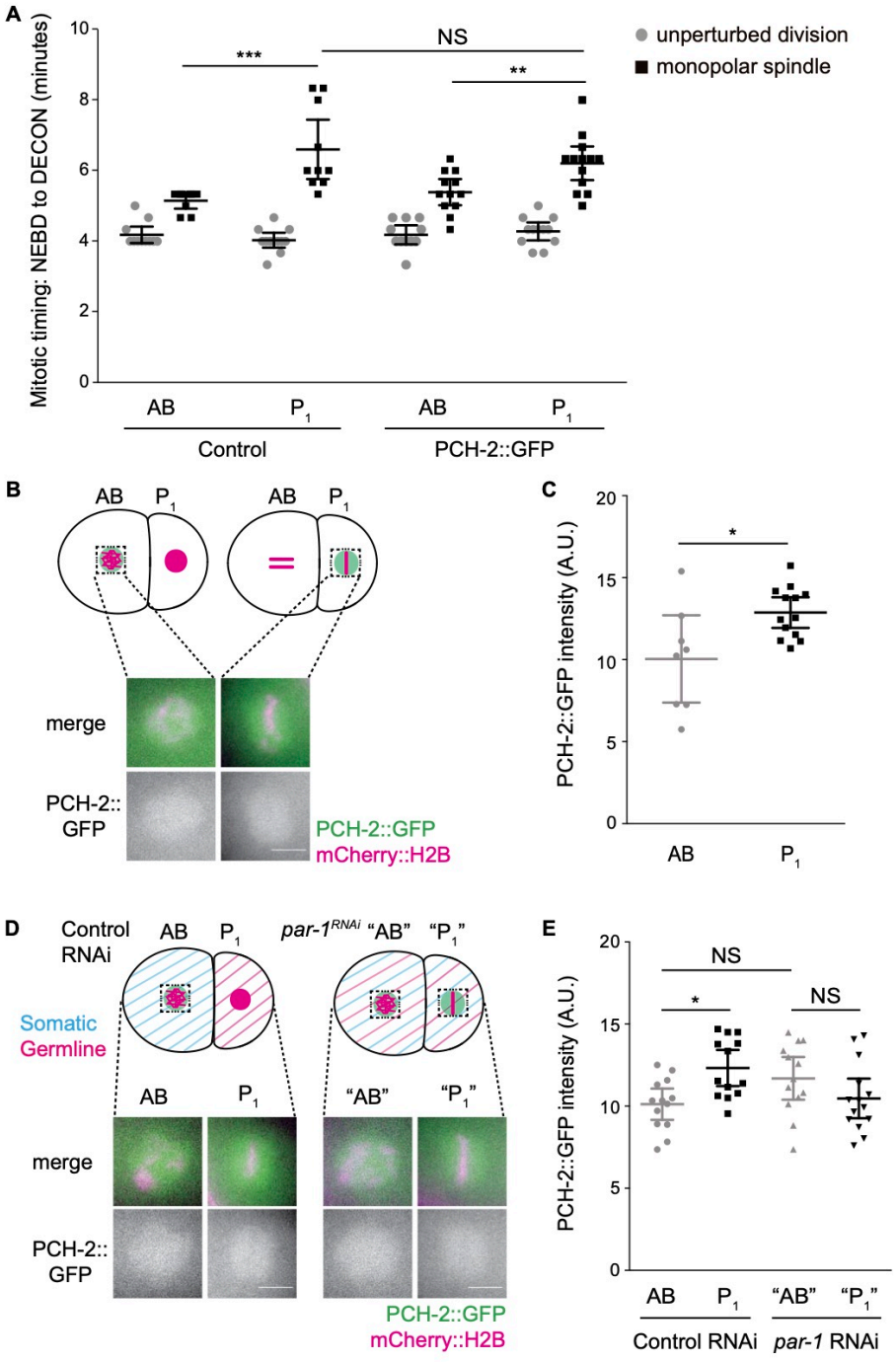
A
Mitotic timing: NEBD to DECON (minutes)
10
8
6
4
2
0
***
NS
**
unperturbed division
monopolar spindle
AB
P1
AB
P1
Control
PCH-2::GFP
B
AB
P1
AB
P1
merge
PCH-2::
GFP
PCH-2::GFP
mCherry::H2B
C
PCH-2::GFP intensity (A.U.)
20
15
10
5
0
*
AB
P1
D
Control
RNAi
AB
P1
par-1RNAi
"AB"
"P1"
Somatic
Germline
AB
P1
"AB"
"P1"
merge
PCH-2::
GFP
PCH-2::GFP
mCherry::H2B
E
PCH-2::GFP intensity (A.U.)
20
15
10
5
0
NS
*
NS
AB
P1
"AB"
"P1"
Control RNAi
par-1 RNAi

Figure 19: There is no difference in the amount of PCH-2::GFP or GFP::MAD-2 recruited to unattached kinetochores in AB and P_1 cells.

(A) Cartoon and images of PCH-2::GFP recruitment to unattached kinetochores in AB and P_1 cells of 2-cell embryos. Scale bar indicates 1 μm. (B) Quantification of PCH-2::GFP recruitment at unattached kinetochores in AB and P_1 cells. (C) Cartoon and images of GFP::MAD-2 recruitment to unattached kinetochores in AB and P_1 cells of 2-cell embryos. Scale bar indicates 1 μm. (D) Quantification of GFP::MAD-2 fluorescence at unattached kinetochores in AB and P_1 cells. All error bars are 95% confidence intervals. NS indicates not significant.

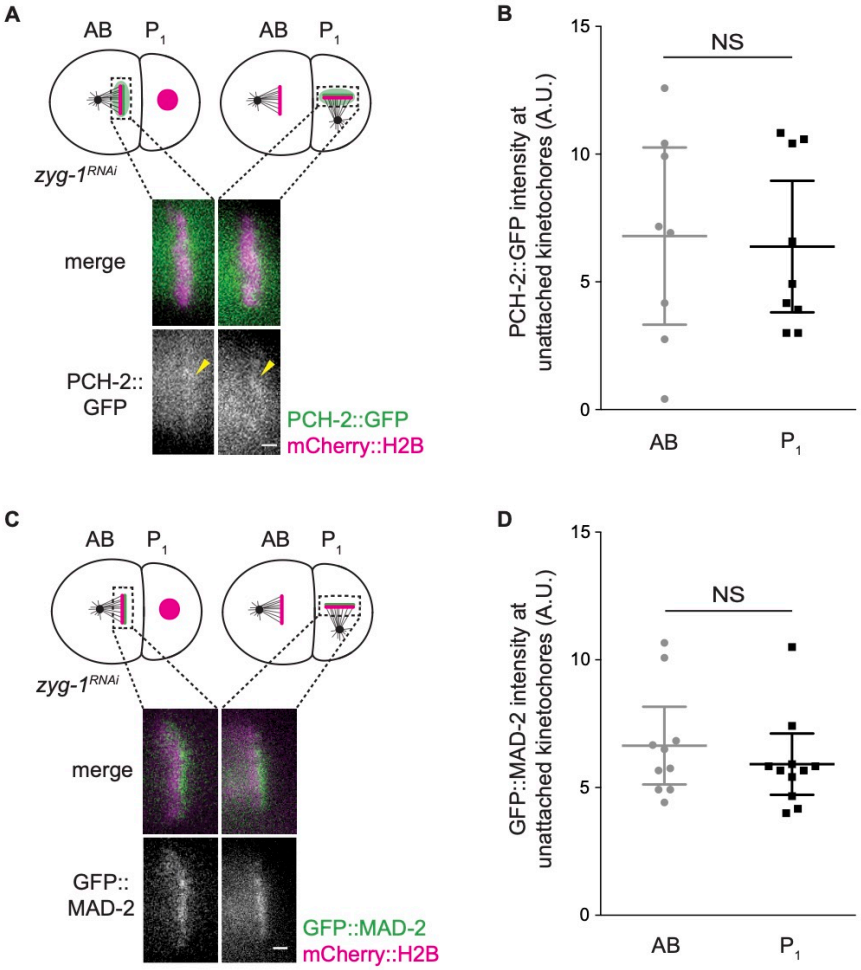
A
AB
P1
AB
P1
zyg-1RNAi
merge
PCH-2::
GFP
PCH-2::GFP
mCherry::H2B
B
NS
PCH-2::GFP intensity at
unattached kinetochores (A.U.)
15
10
5
0
AB
P1
C
AB
P1
AB
P1
zyg-1RNAi
merge
GFP::
MAD-2
GFP::MAD-2
mCherry::H2B
D
NS
GFP::MAD-2 intensity at
unattached kinetochores (A.U.)
15
10
5
0
AB
P1

be different between AB and P_1 cells. First, we verified that PCH-2::GFP fluorescence around mitotic chromosomes was similar between AB cells during unperturbed (control) or monopolar mitosis (*zyg-1*^{RNAi}) (Figure 20). PCH-2::GFP fluorescence around chromosomes was significantly higher in *zyg-1*^{RNAi} AB cells than control AB cells (Figure 20B). However, we noticed that the area occupied by PCH-2::GFP in control AB cells was significantly larger than that of *zyg-1*^{RNAi} AB cells (yellow dashed circle in Figure 20A and quantified in Figure 20C). When we factored this larger area of PCH-2::GFP fluorescence into our analysis, we observed a similar amount of PCH-2::GFP around mitotic chromosomes in both control and *zyg-1*^{RNAi} AB cells (Figure 20D).

Having established that AB cells had similar amounts of PCH-2::GFP whether the checkpoint was active or not, we quantified PCH-2::GFP fluorescence in the area around mitotic chromosomes in AB and P_1 cells during unperturbed cell cycles. Similar to AB cells (Nelson *et al.*, 2015) and Figure 20A), we observed PCH-2::GFP enriched in the area around the chromosomes in prometaphase in P_1 cells (Figure 19B). When we quantified the fluorescence of PCH-2::GFP in this area surrounding chromosomes after NEBD in both AB and P_1 cells, we detected a statistically significant enrichment of PCH-2::GFP in the area surrounding chromosomes in P_1 cells (Figure 19C) but not in the cytoplasm of P_1 cells (Figures 21A and B). Although this enrichment is limited to a "cloud" around mitotic chromosomes (see Figure 21B), we verified that this enrichment was not the indirect consequence of the smaller

Figure 20: There is no difference in the amount of PCH-2::GFP around mitotic chromosomes in AB cells with bipolar or monopolar spindles.

(A) Cartoon and images of PCH-2::GFP localization around mitotic chromosomes in AB cells of 2-cell embryos. Scale bar indicates 5 µm. Yellow dashed circle indicates area of PCH-2::GFP fluorescence. (B) Quantification of PCH-2::GFP fluorescence in AB cells with bipolar spindles (control) or monopolar spindles (zyg-1RNAi). (C) Quantification of area of PCH-2::GFP fluorescence in AB cells with bipolar spindles or monopolar spindles. (D) Quantification of integrated density of PCH-2::GFP fluorescence in AB cells with bipolar spindles or monopolar spindles. All error bars are 95% confidence intervals. NS indicates not significant.

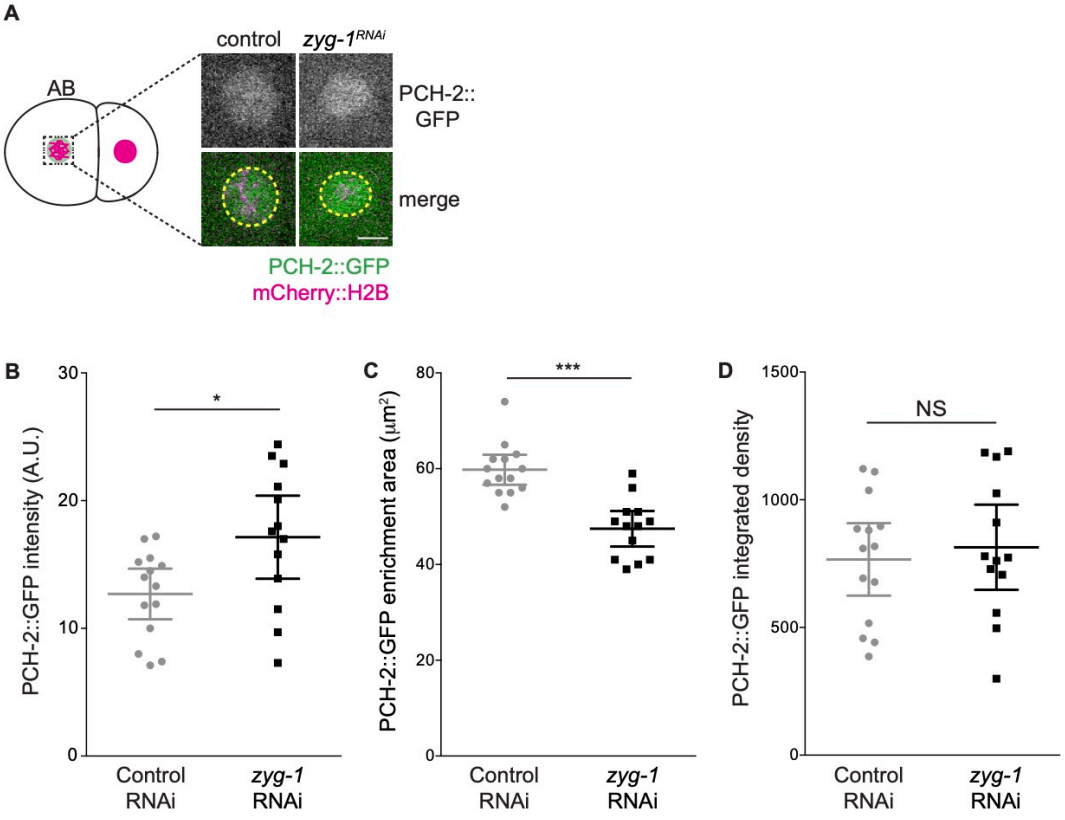

Figure 21: PCH-2's enrichment in P1 cells is around chromosomes and does not depend on GPR-1/2.

(A) Quantification of PCH-2::GFP fluorescence in the cytoplasm of AB and P1 cells. (B) Images of AB (left) and P1 (right) cells after NEBD. Scale bar indicate 5 μm. (C) Quantification of cell area in AB and P1 cells of control RNAi and gpr-1/2RNAi 2-cell embryos. Red symbols indicate cells in which PCH-2::GFP fluorescence was quantified in (D). (D) Quantification of PCH-2::GFP fluorescence in AB and P1 cells of control RNAi and gpr-1/2RNAi embryos. (E) Cartoon and images of PCH-2::GFP localization around mitotic chromosomes in AB and P1 cells of control RNAi and gpr-1/2RNAi 2-cell embryos. Scale bars indicate 5 μm. Error bars are 95% confidence intervals. NS indicates not significant.

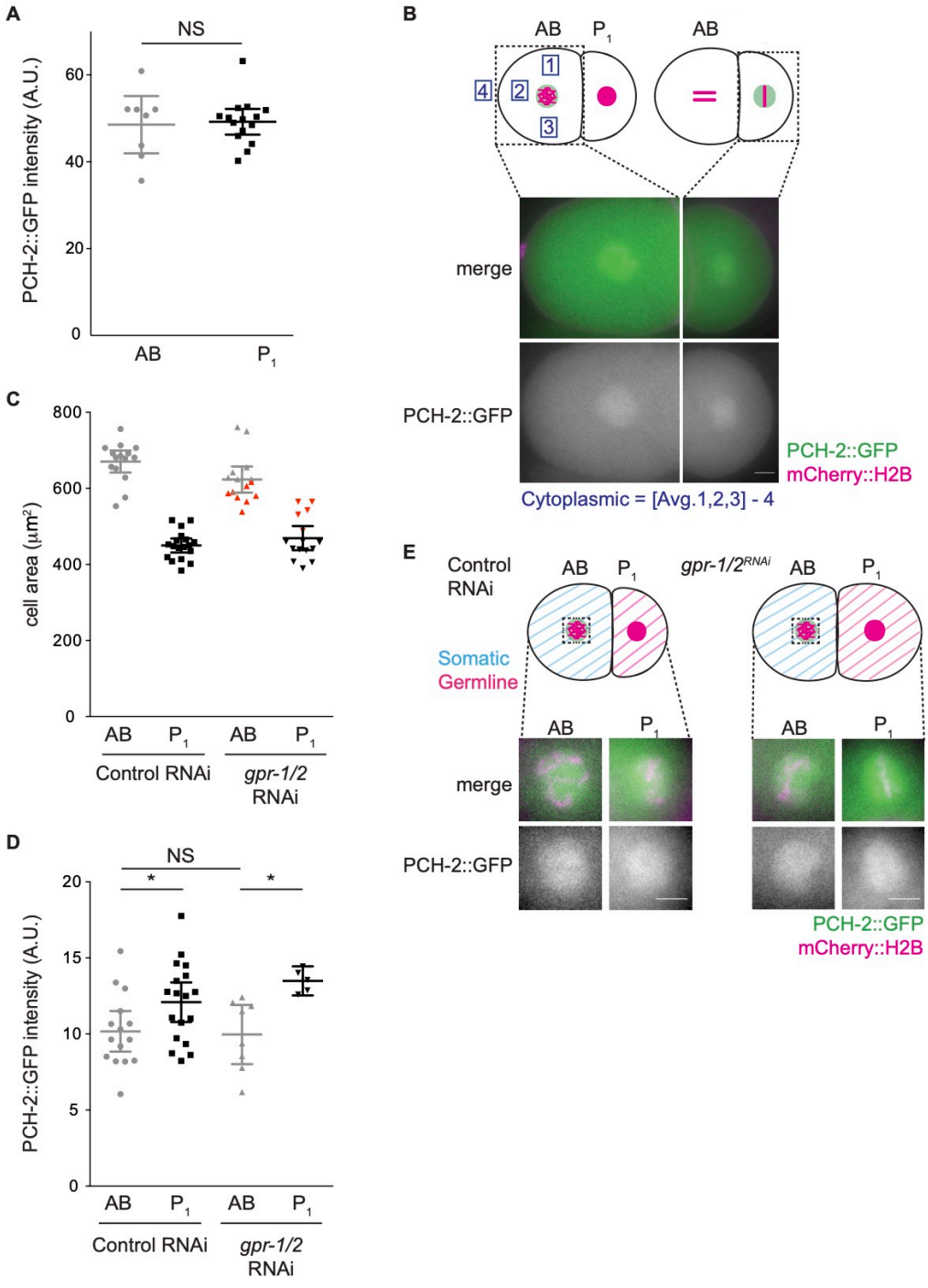
A
NS
PCH-2::GFP intensity (A.U.)
60
40
20
0
AB
P1
B
AB
P1
AB
1
2
3
4
=
merge
PCH-2::GFP
PCH-2::GFP
mCherry::H2B
Cytoplasmic = [Avg.1,2,3] - 4
C
cell area (μm²)
800
600
400
200
0
AB
P1
AB
P1
Control RNAi
gpr-1/2
RNAi
D
NS
*
*
PCH-2::GFP intensity (A.U.)
20
15
10
5
0
AB
P1
AB
P1
Control RNAi
gpr-1/2
RNAi
E
Control
RNAi
AB
P1
gpr-1/2RNAi
AB
P1
Somatic
Germline
AB
P1
AB
P1
merge
PCH-2::GFP
PCH-2::GFP
mCherry::H2B

volume of P_1 cells by quantifying PCH-2::GFP fluorescence in *gpr-1/2*^{RNAi} embryos. This double knockdown equalizes the size of AB and P_1 cells without affecting their cell fate (Colombo et al., 2003; Gotta et al., 2003; Srinivasan et al., 2003). RNAi of *gpr-1/2* showed variability in the effect on AB and P_1 cell size (Figure 21C). However, when we limited our analysis of PCH-2::GFP fluorescence to embryos in which AB and P_1 cells were of similar area (red symbols in Figure 21C), we observed a similar enrichment of PCH-2::GFP in P_1 cells as control embryos (Figures 21D and E).

To better understand the relationship between PCH-2 enrichment in P_1 cells and cell fate, we abrogated the asymmetry of the 2-cell embryo by performing RNAi against the essential polarity factors, PAR-1 (Guo and Kemphues, 1995) and PAR-6 (Hung and Kemphues, 1999). These factors antagonize each other, with PAR-6 at the anterior cortex and PAR-1 at the posterior cortex of early embryos, to establish asymmetries during the first two embryonic divisions (Goldstein and Macara, 2007). In both *par-1*^{RNAi} and *par-6*^{RNAi} mutant embryos, AB and P_1 cells exhibit similar checkpoint strength (Gerhold *et al.*, 2018), indicating that the stronger spindle checkpoint response in P_1 cells depends on this asymmetric division. Despite the loss of cell fate in *par-1*^{RNAi} and *par-6*^{RNAi} embryos, we will refer to the anterior blastomere as "AB" and the posterior as "P_1". We verified the efficiency of *par-1* and

Figure 22: PCH-2's enrichment around mitotic chromosomes in P1 cells depends on PAR-6.

(A and B) Quantification of cell area in AB and P1 cells of control RNAi, par-1RNAi and par-6RNAi 2-cell embryos. (C) Cartoon and images of PCH-2::GFPRNAi localization around mitotic chromosomes in AB and P1 cells of control RNAi and par-6 2-cell embryos. Scale bars indicate 5 µm. (D) Quantification of PCH-2::GFP fluorescence in AB and P1 cells of control RNAi and par-6RNAi embryos. Error bars are 95% confidence intervals. NS indicates not significant.

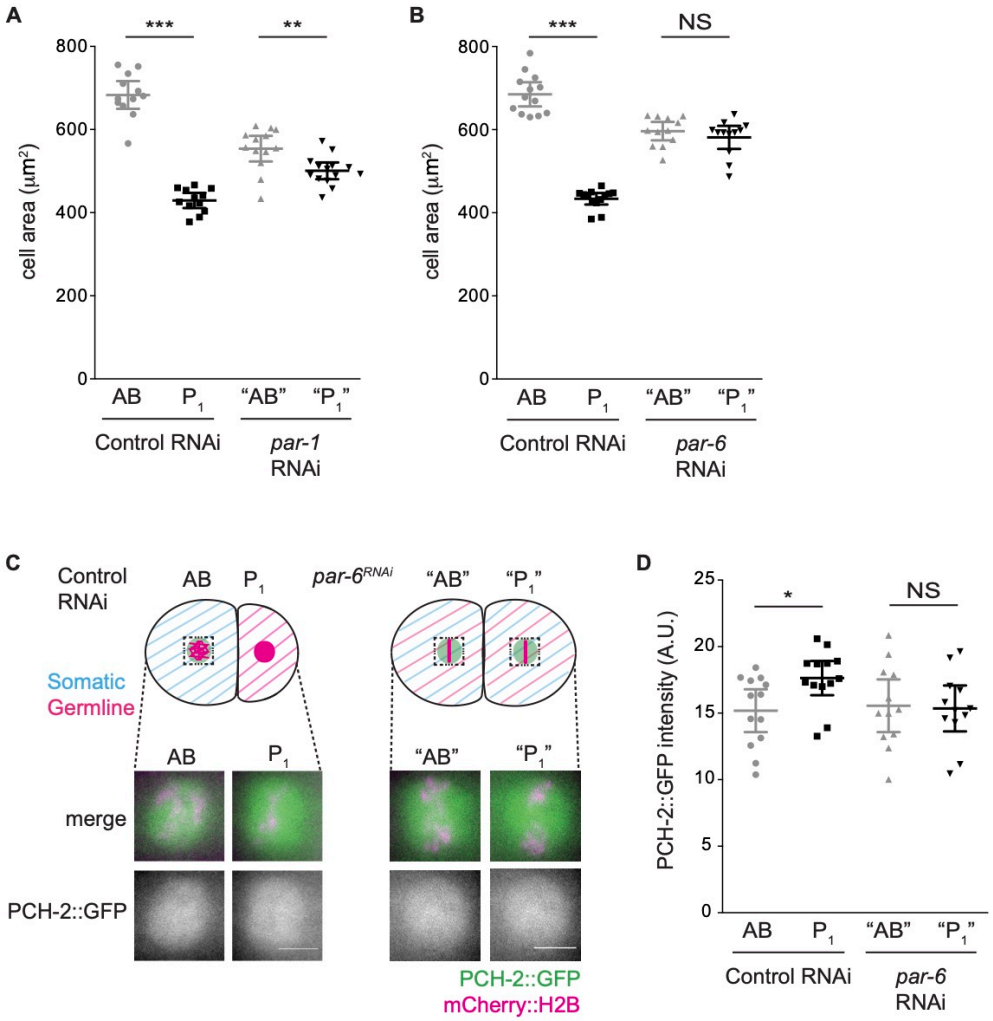

par-6 RNAi by measuring cell area and found that AB and P_1 cells approached similar sizes in both conditions (Figures 22A and B), although AB cells were still significantly larger than P_1 cells in *par-1*^{RNAi} mutant embryos (Figure 22A). We quantified PCH-2::GFP fluorescence in the area around chromosomes in AB and P_1 cells after *par-1* RNAi and observed that the fluorescence of PCH-2::GFP, despite being slightly lower in P_1 cells, was not significantly different between AB and P_1 cells, unlike what we observed in embryos exposed to control RNAi (Figures 18D and E). AB and P_1 cells treated with *par-6* RNAi showed equal PCH-2::GFP fluorescence (Figures 22C and D). Therefore, PCH-2::GFP's enrichment around mitotic chromosomes in P_1 cells depends on the conserved factors that induce embryonic asymmetry and germline cell fate, PAR-1 and PAR-6.

The stronger checkpoint in P_1 cells depends on CMT-1

In vitro, the *C. elegans* ortholog of p31^{comet}, CMT-1, is required for PCH-2 to bind and remodel Mad2 (Ye *et al.*, 2015). In addition to this role, CMT-1 is also required to localize PCH-2 to unattached kinetochores and generate a robust spindle checkpoint response in AB cells (Nelson *et al.*, 2015). Therefore, we reasoned that CMT-1 might also be required for the stronger checkpoint in P_1 cells.

To test this possibility, we first performed double knockdown of *ani-2* and *zyg-1* in *cmt-1* mutants and monitored the length of the spindle checkpoint response as AB and

Figure 23: The stronger checkpoint in P1 cells depends on CMT-1

(A) Mitotic timing, as measured from nuclear envelope breakdown (NEBD) to the onset of cortical contractility (OCC), in AB and P1 cells plotted against cell volume in cmt-1;ani-2RNAi;zyg-1RNAi embryos. Lines represent least-squares regression models with 95% confidence intervals (gray shaded areas) for each set of data. The opaque blue line represents the regression model of the control AB data from Figure 1C. Equations and p values indicating whether slopes are significantly non-zero for each model are: cmt-1;ani-2RNAi;zyg-1RNAi AB (dark green): y=-0.713x+7.44 and p = 0.0050; cmt-1;ani-2RNAi;zyg-1RNAi P1 (light green): y=-0.6767x+5.291 and p = 0.0452. (B) Mitotic timing of control, cmt-1 and mad-1 mutant embryos during unperturbed divisions or in the presence of monopolar spindles. (C) Cartoon and images of PCH-2::GFP localization around mitotic chromosomes in AB and P1 cells of cmt-1 mutant embryos. Scale bar indicates 5 μm. (D) Quantification of PCH-2::GFP fluorescence in AB cells of control and cmt-1 mutant embryos. (E) Quantification of PCH-2::GFP fluorescence in AB and P1 cells of cmt-1 mutant embryos. All error bars are 95% confidence intervals. NS indicates not significant.

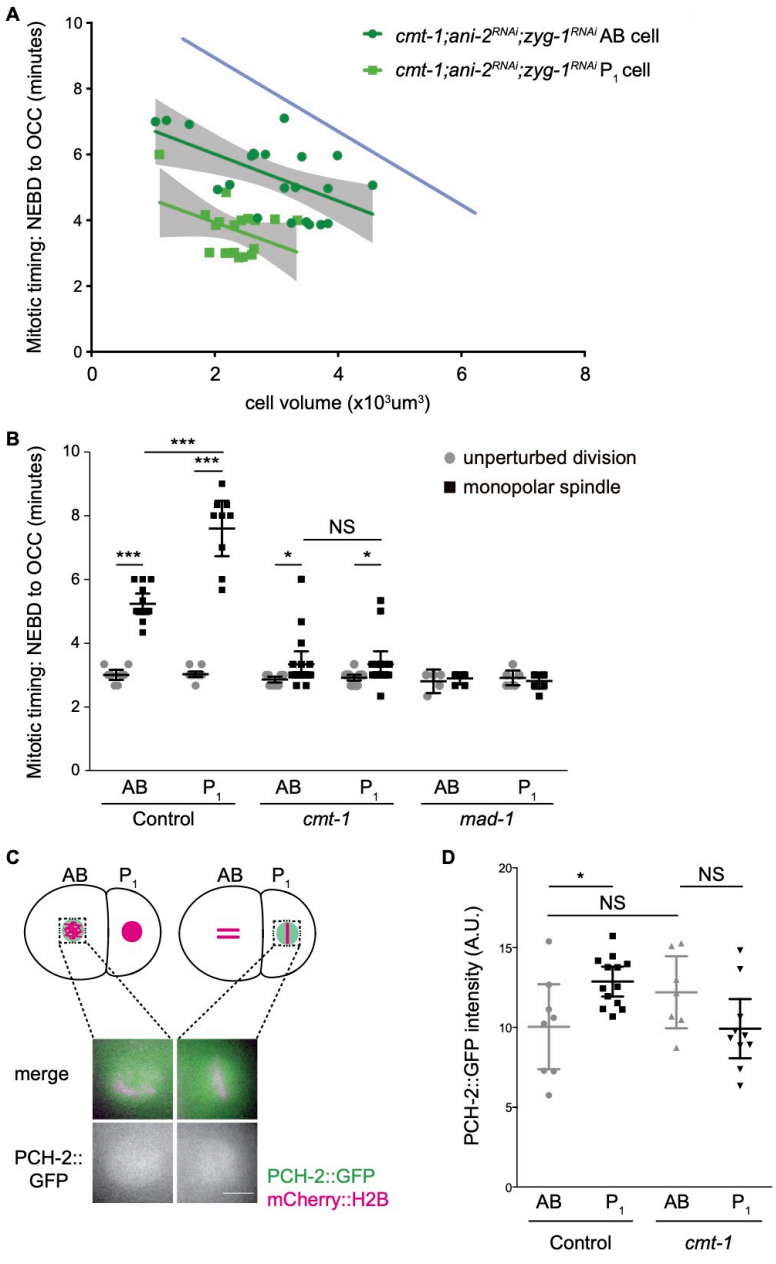
A
Mitotic timing: NEBD to OCC (minutes)
cell volume (x10³um³)
cmt-1;ani-2RNAi;zyg-1RNAi AB cell
cmt-1;ani-2RNAi;zyg-1RNAi P1 cell
B
Mitotic timing: NEBD to OCC (minutes)
unperturbed division
monopolar spindle
***
***
***
*
NS
*
AB
P1
Control
cmt-1
mad-1
C
AB
P1
merge
PCH-2::
GFP
PCH-2::GFP
mCherry::H2B
D
PCH-2::GFP intensity (A.U.)
*
NS
NS
Control
cmt-1

P_1 cells became smaller (Figure 23A, Videos 9-12). When compared to the regression model for control AB cells (opaque blue line in Figure 23A), we saw that *cmt-1* AB cells consistently exhibit a weaker checkpoint at all cell volumes. Similar to *pch-2;ani-2*^{RNAi}*;zyg-1*^{RNAi} mutants (Figure 17B), the stronger spindle checkpoint response in P_1 cells was lost in *cmt-1;ani-2*^{RNAi}*;zyg-1*^{RNAi} mutants and we did not observe any statistical difference between the between the slopes of the regression analysis of P_1 and AB cells (p value = 0.9403). We also observed that cell cycle timing was faster in *cmt-1* P_1 cells that were similar in volume to *cmt-1* AB cells (Figure 23A). Thus, CMT-1 is also essential to promote spindle checkpoint strength in germline precursor cells.

We also performed *zyg-1* RNAi on control and *cmt-1* mutant embryos and monitored mitotic timing in both AB and P_1 cells. AB and P_1 cells of control and *cmt-1* mutant embryos treated with control RNAi had similar mitotic timing. Unlike similar experiments in *pch-2* mutants (Figure 17C), we did not detect a statistically significant difference between cell cycle time in P_1 cells between wildtype and *cmt-1* mutants embryos (Figure 23B), suggesting that *ani-2*^{RNAi}*;zyg-1*^{RNAi} embryos might be more sensitive to subtle perturbations in cell cycle timing. In *zyg-1*^{RNAi} embryos, P_1 cells exhibited a stronger checkpoint response than AB cells (Figure 23B). By contrast, both AB and P_1 cells in *cmt-1*;*zyg-1*^{RNAi} mutant embryos exhibited similar spindle checkpoint delays (Figure 23B). Despite having spindle checkpoint responses that were less robust than that of control *zyg-1*^{RNAi} embryos, AB and P_1 cells in *cmt-1*

mutant embryos treated with *zyg-1* RNAi spent significantly longer in mitosis than *cmt-1* mutant embryos treated with control RNAi (Figure 23B), indicating that they activated a weaker spindle checkpoint response, similar to our published results (Nelson *et al.*, 2015). More importantly, *cmt-1*;*zyg-1*^{RNAi} mutant embryos failed to generate a stronger checkpoint in P_1 cells, consistent with *cmt-1;ani-2*^{RNAi}*;zyg-1*^{RNAi} experiments (Figure 23A).

Aside from localizing PCH-2 to unattached kinetochores (Nelson *et al.*, 2015), we wondered if CMT-1 was required for any other aspects of PCH-2 regulation. Therefore, we tested whether CMT-1 was necessary for PCH-2's asymmetric enrichment in P_1 cells. We quantified PCH-2::GFP fluorescence in prometaphase in the area around chromosomes in both *cmt-1* mutant AB and P_1 cells (Figure 23C). First, we found that PCH-2::GFP fluorescence was slightly higher in AB cells in *cmt-1* mutants than control embryos (Figure 23D). We saw a similar result in our *par-1* RNAi experiments, although in both cases these increases were not statistically significant. However, unlike *par-1*^{RNAi} embryos (Gerhold *et al.*, 2018), this increase in PCH-2::GFP was not accompanied by an increase in checkpoint strength (Figure 23B), consistent with our hypothesis that the weaker checkpoint in *cmt-1* AB cells is a consequence of PCH-2's absence from unattached kinetochores (Nelson *et al.*, 2015). Further, when we compared the quantification of PCH-2::GFP fluorescence in *cmt-1* mutant AB and P_1 cells (Figure 23C), we did not detect a significant difference between the two cells (Figure 23D), unlike our experiment in control embryos

(Figures 18B and C), indicating that CMT-1 contributes to the asymmetric enrichment of PCH-2 in P_1 cells. Thus, CMT-1 promotes spindle checkpoint strength through two mechanisms: localizing PCH-2 to unattached kinetochores and ensuring its enrichment in germline precursor cells.

Discussion

The role of PCH-2, and its mammalian ortholog TRIP13, in the spindle checkpoint has been enigmatic (see Table 1). Originally identified as a checkpoint silencing factor (Alfieri *et al.*, 2018; Brulotte *et al.*, 2017; Eytan *et al.*, 2014; Miniowitz-Shemtov *et al.*, 2015; Wang *et al.*, 2014; Ye *et al.*, 2015), more recent evidence also indicates a role in promoting the checkpoint response (Ma and Poon, 2016; Ma and Poon, 2018; Nelson *et al.*, 2015; Yost *et al.*, 2017). It's clear that the reliance on PCH-2/TRIP13 in checkpoint activation reflects the relative levels and availability of O-Mad2 (Ma and Poon, 2018). We show here that PCH-2 also controls checkpoint strength. Surprisingly, we can uncouple PCH-2's requirement for checkpoint activation, which we detect in both AB and P_1 cells of wildtype sized 2-cell embryos (Nelson *et al.*, 2015) and Figure 16), from the requirement for spindle checkpoint strength, which we observe when we genetically manipulate cell size of 2-cell embryos by *ani-2* RNAi (Figures 9C and 17B). Based on this, we propose that PCH-2 regulates checkpoint strength not only by regulating O-Mad2 availability, but by doing so specifically at and near unattached kinetochores, providing an unanticipated

Figure 24: Model for how PCH-2 regulates checkpoint strength.

(A) A robust spindle checkpoint response in large cells requires the presence of PCH-2 at unattached kinetochores to increase the local concentration O-MAD-2 at and near unattached kinetochores. (B) Reducing cell volume of 2-cell embryos increases the concentration of O-Mad-2 at and near unattached kinetochores, allowing a checkpoint response in the absence of PCH-2. (C) The enrichment of PCH-2 around mitotic chromosomes in P1 cells results in a higher production of O-MAD-2, generating a stronger spindle checkpoint response in these cells.

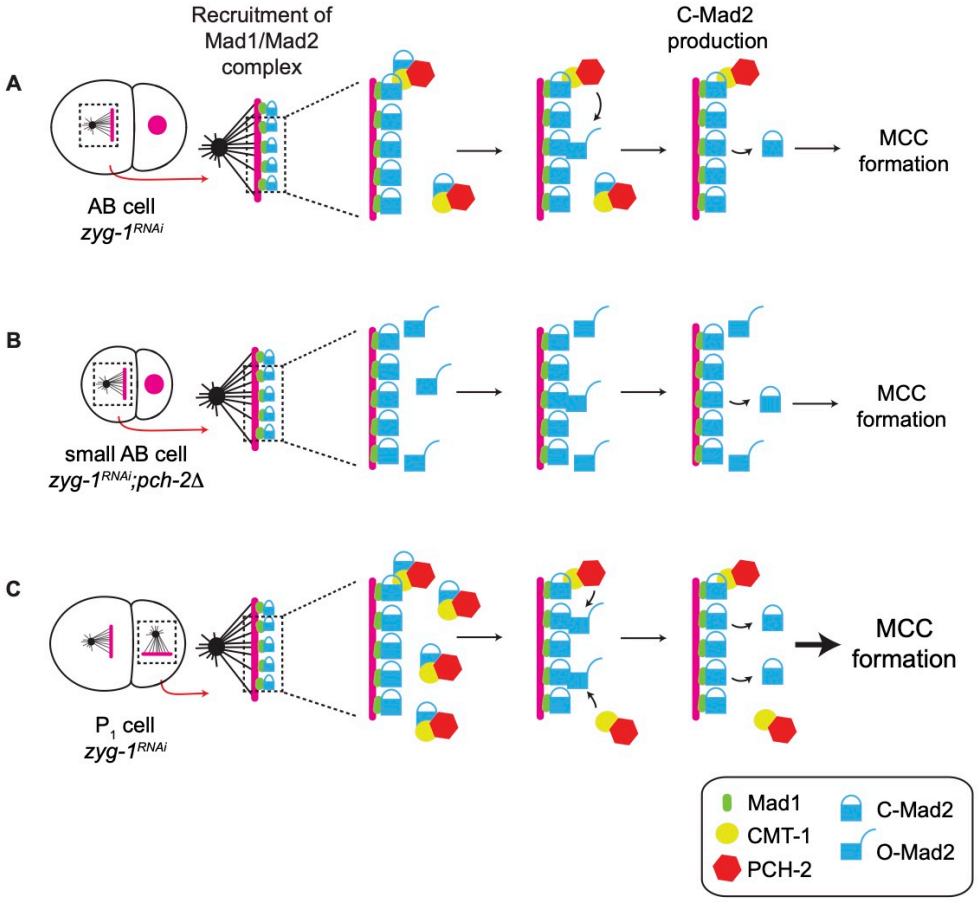

Table 1: Mitotic roles of PCH-2/TRIP13 and CMT-1/p31

Table 1: Mitotic roles of PCH-2/TRIP13 and CMT-1/p31^{comet}

protein	Mitotic roles in *C. elegans*	Mitotic roles in human cells
PCH-2/TRIP13	• promotes checkpoint function (Nelson *et al.*, 2015) • regulates Mad2 at unattached kinetochores (Nelson *et al.*, 2015) • no effect on Mad2 protein levels (Nelson *et al.*, 2015) • no effect on checkpoint silencing (this study) • controls spindle checkpoint strength (this study)	• promotes checkpoint function (Ma and Poon, 2016; Marks *et al.*, 2017; Yost *et al.*, 2017; Ma and Poon, 2018) • regulates Mad2 at unattached kinetochores (Yost *et al.*, 2017) • stabilizes Mad2 protein levels (Ma and Poon, 2016; Marks *et al.*, 2017; Yost *et al.*, 2017) • silences checkpoint (Eytan *et al.*, 2014; Wang *et al.*, 2014; Miniowitz-Shemtov *et al.*, 2015; Ma and Poon, 2016)
CMT-1/p31^{comet}	• promotes checkpoint function (Nelson *et al.*, 2015) • regulates Mad2 at unattached kinetochores (Nelson *et al.*, 2015) • stabilizes Mad2 protein levels (Nelson *et al.*, 2015) • no effect on checkpoint silencing (this study) • required for PCH-2 localization to unattached kinetochores (Nelson *et al.*, 2015) • required for PCH-2 enrichment in germline precursor cells during embryogenesis (this study) • controls spindle checkpoint strength (this study)	• no effect on checkpoint function (Xia *et al.*, 2004; Ma and Poon, 2016) • no effect on Mad2 at kinetochores (Westhorpe *et al.*, 2011) • no effect on Mad2 protein levels (Ma and Poon, 2016) • silences checkpoint (Habu *et al.*, 2002; Xia *et al.*, 2004; Teichner *et al.*, 2011; Westhorpe *et al.*, 2011)

mechanism to explain this phenomenon (Figure 24). Given that *cmt-1* mutants exhibit decreased Mad2 protein levels (Nelson *et al.*, 2015), suggesting that CMT-1's binding to C-Mad2 stabilizes the protein in *C. elegans*, we speculate that PCH-2 is specifically disassembling a C-Mad2/CMT-1 complex to generate this pool of O-Mad2. This role in checkpoint strength appears to be particularly important in large cells, such as oocytes and cells in early embryos, as well as cells that give rise to immortal germ cells.

Our model assumes that 2-cell embryos have a significant amount of O-Mad2 available, even when PCH-2 function is lost (Figure 24), unlike what is reported in human cells (Ma and Poon, 2016). Given that this is a developmental system in which embryos have only undergone a single mitotic division before we perform our assays and newly synthesized Mad2 adopts the open conformation (Kim et al., 2018), we propose that O-Mad2 is not limiting in very early embryos, even in *pch-2* null mutants. In this way, *C. elegans* 2-cell embryos would be analogous to human cells undergoing cell division soon after acute depletion of TRIP13 (Ma and Poon, 2018). Unfortunately, we were unable to directly probe O-Mad2 concentration or its availability at or near unattached kinetochores in small *ani-2*^{RNAi} embryos or germline precursor cells. However, we think that several pieces of data support our model (Figure 24). PCH-2's characterized biochemical activity regulates the availability of O-Mad2 (Alfieri *et al.*, 2018; Brulotte *et al.*, 2017; Ye *et al.*, 2015), making this the likely mechanism through which PCH-2 regulates checkpoint strength. PCH-2 at

unattached kinetochores in AB and P_1 cells (Nelson *et al.*, 2015) and Figure 23B) and its enrichment around mitotic chromosomes in P_1 cells (Figures 17A and 18C) correlates with a stronger checkpoint. The loss of PCH-2 or this enrichment produces similar checkpoint strength between AB and P_1 cells (Gerhold et al., 2018 and Figures 9C, 17B, 18E, 21D, 23A and 23D). Indeed, the equalization of PCH-2::GFP between AB and P_1 cells that we observe in *par-1*^{RNAi} and *par-6*^{RNAi} embryos (Figures 18E and 22D) is entirely consistent with the observation that in these mutants, AB cells more closely resemble P_1 cells in spindle checkpoint strength (Gerhold et al., 2018). Finally, checkpoint strength depends on Mad2 dosage (Figure 11C), particularly in AB cells of 4-cell *pch-2* mutant embryos (Figure 15B).

Another prediction of our model is that overexpression of Mad2 should also make PCH-2 dispensable for spindle checkpoint activation. We've shown that subtle elevations of Mad2 protein levels introduce a cell cycle delay in AB cells of 4-cell embryos treated with nocodazole but not those treated with DMSO (Figure 15B), entirely consistent with our model. However, it's not clear why we do not observe a similar effect in cells of the AB lineage of 16-cell embryos that overexpress Mad2 (Figure 15B). Unfortunately, more dramatic overexpression experiments are technically difficult in *C. elegans*. Further, it's likely that strong overexpression of Mad2 in *C. elegans* embryos will delay normal mitosis, consistent with similar findings in mammalian cells (Marks et al., 2017) and budding yeast (Mariani et al., 2012). In this way, PCH-2's function may provide a useful buffer: Since Mad2

protein levels may need to stay within a narrow range to allow normal mitotic timing, PCH-2's localization at and near unattached kinetochores provide a mechanism to increase O-Mad2's local concentration to promote effective and efficient signaling during checkpoint activation.

The requirement for PCH-2 in spindle checkpoint strength is also seen as AB cells normally decrease in volume during embryogenesis (Figure 15A), although not as dramatically as when we genetically manipulate cell size (Figure 9C). The inconsistency between our *ani-2* and embryogenesis experiments could be explained by a variety of factors. O-Mad2 may eventually become limiting in cells of the AB lineage with successive divisions after the 2-cell stage, resulting in a greater reliance on PCH-2 function. Moreover, it may also suggest that relative levels of O-Mad2 and C-Mad2 are more stringently regulated as embryonic development progresses and the multi-cellular embryo becomes more complex. This possibility is supported by our finding that PCH-2 regulates normal cell cycle timing in P_1 cells, but not AB cells (Figure 17C), which implies that variations in O-Mad2/C-Mad2 ratios influence normal mitotic timing in cells with specific developmental fates. In addition, unlike the nuclei of 2-cell embryos treated with *ani-2*^{RNAi} (Figure 14), nuclear volume scales with cell volume during embryogenesis (Gerhold *et al.*, 2018). Therefore, the concentration of Mad2 may not necessarily increase as cell size decreases in cells of the developing embryo, making direct comparisons between small cells obtained by *ani-2*^{RNAi} treatment and small cells resulting from normal embryogenesis challenging.

Finally, recent reports have indicated that, during embryogenesis in other systems, cell volume may not be a major contributor to spindle checkpoint strength (Chenevert et al., 2019; Vazquez-Diez et al., 2019). Indeed, in *C. elegans*, when only AB cells are monitored during very early embryogenesis (the 2-8 cell stage), they exhibit very minor increases, if any, in checkpoint strength (Galli and Morgan, 2016; Gerhold *et al.*, 2018) and Figure 15). This may suggest that cell fate is generally a more important determinant of spindle checkpoint strength during normal embryogenesis, potentially reconciling reports from a wide array of systems.

Our experiments identify CMT-1, the *C. elegans* ortholog of mammalian $p31^{comet}$, as an important regulator of PCH-2 function and, as a result, checkpoint strength. In addition to its requirement in facilitating PCH-2's ability to interact with its substrate, Mad2 (Alfieri *et al.*, 2018; Brulotte *et al.*, 2017; Miniowitz-Shemtov *et al.*, 2015; Ye *et al.*, 2015), CMT-1 localizes PCH-2 to unattached kinetochores (Nelson *et al.*, 2015) and promotes PCH-2's enrichment in P_1 cells (Figure 23D). We propose that both of these roles contribute to checkpoint strength. In large AB cells, CMT-1 ensures PCH-2's presence at unattached kinetochores, increasing the local concentration of O-Mad2, driving the production of soluble C-Mad2 and MCC and enforcing a robust checkpoint (Figure 24A). In P_1 cells, the combination of PCH-2's localization at kinetochores and its enrichment around chromosomes and near unattached kinetochores produces a checkpoint stronger than somatic cells (Figure 24C). It's striking that, when CMT-1 is absent, AB cells, in which there is more PCH-

2 (Figure 23D), and P_1 cells, which are slightly smaller than AB cells, exhibit similar checkpoint strength (Figure 23B). This indicates that even these cells depend on PCH-2 to be present at unattached kinetochores to increase the local concentration of O-Mad2 and promote checkpoint strength.

P_1 cells in both *pch-2;ani-2^{RNAi};zyg-1^{RNAi}* and *cmt-1;ani-2^{RNAi};zyg-1^{RNAi}* mutants show faster cell cycle timing than similarly sized AB cells of the same genotype (Figures 17B and 23A). However, only *pch-2* mutants significantly affect cell cycle timing in unperturbed P_1 cells, (Figure 17C); P_1 cells in *cmt-1* and *mad-1* mutants show accelerated cell cycle timing but this is not significantly faster than control (Figures 17C and 23B). Further, we don't detect significant acceleration of the cell cycle in P_1 cells of *pch-2;zyg-1^{RNAi}* or *mad-1;zyg-1^{RNAi}* mutant embryos (Figure 16 and 23B). Given the rapidity of cell cycles in these early embryos, it's possible that *ani-2^{RNAi};zyg-1^{RNAi}* experiments provide greater sensitivity to observe subtle accelerations in cell cycle timing and that some subset of spindle checkpoint components, including PCH-2, CMT-1, MAD-1 and MAD-2 regulate normal cell cycle timing in germline precursor cells, similar to the role of MAD-1 and MAD-2 in germline mitotic nuclei (Gerhold *et al.*, 2015). Unfortunately, we cannot test this with MAD-1 or MAD-2 since *mad-1* and *mad-2* mutants abolish the spindle checkpoint response in *ani-2^{RNAi};zyg-1^{RNAi}* embryos (Gerhold *et al.*, 2015) and Figure 9C)**.** An alternative hypothesis that we do not favor is that only PCH-2 regulates cell cycle timing in P_1 cells, in a mechanism independent of other spindle checkpoint proteins.

Evolutionary analysis across phyla have revealed a close co-evolutionary relationship between PCH-2 and its orthologs and HORMA domain containing proteins, including CMT-1 and Mad2 (van Hooff et al., 2017; Vleugel et al., 2012). However, some organisms that rely on the templated conversion of O-Mad2 to C-Mad2 to assemble the MCC, such as budding and fission yeasts (Chao et al., 2012; Nezi et al., 2006) either don't express their PCH-2 ortholog during mitosis (budding yeast) (San-Segundo and Roeder, 1999) or don't have a PCH-2 ortholog in their genome (fission yeast) (Wu and Burgess, 2006). This is potentially explained by cell volume: Both budding and fission yeasts are two orders of magnitude smaller than mammalian cells and *C. elegans* embryos. They also undergo closed mitosis, in which the nuclear envelope does not break down, providing an additional opportunity to concentrate factors required for mitosis. We propose that recruiting O-Mad2 to unattached kinetochores may not present as great a challenge in these significantly smaller cells, making a factor required to increase the local concentration of O-Mad2 at unattached kinetochores unnecessary.

An obvious question our experiments raise is how PCH-2 is enriched in P_1 cells. Germline precursor cells are transcriptionally silent until gastrulation (Seydoux et al., 1996) and sequencing of mRNA in early embryos shows that both CMT-1 and PCH-2 mRNA are not enriched in germline precursor cells (Tintori *et al.*, 2016), indicating that enrichment of PCH-2 is likely to occur at the level of protein regulation.

Understanding this regulation, its control by developmental events and its effect on the relative levels of O-Mad2 and C-Mad2 in different cell types promises to be an exciting area of investigation.

Materials and Methods

Worms strains

The *C. elegans* Bristol N2 (Brenner, 1974) was used as the wild-type strain. Most strains were maintained at 20°C, except for *zyg-1(or297)* strains, which were maintained at 15°C. See Table S1 for the list of all the strains used in this study.

Immunostaining

Immunostaining was performed on adult worms 48h after L4, as described in (Bhalla and Dernburg, 2005). The antibodies used were rabbit anti-MAD-2 (1/500; (Essex *et al.*, 2009) and mouse anti-MAb414 (1/400; (Davis and Blobel, 1986). Secondary antibodies were Alexa Fluor 488 anti-rabbit (Invitrogen) and Cy3 anti-mouse (Jackson ImmunoResearch Laboratories, Inc.) diluted at 1:500. Antibody against MAD-2 was a gift from A. Desai (Ludwig Institute/University of California, San Diego, La Jolla, CA).

Images were acquired on a DeltaVision Personal DV microscope (GE Healthcare) equipped with a 100× NA 1.40 oil-immersion objective (Olympus), a short ARC xenon lamp (GE Healthcare) and using a CoolSNAP charge-coupled camera (Roper

Scientific). Z-stacks were collected at 0.2 μm Z-spacing and processed by constrained, iterative deconvolution. Imaging, image scaling, and analysis were performed using functions in the softWoRx software package (GE Healthcare). Projections were calculated by a maximum intensity algorithm. Composite images were assembled and some false coloring was performed with Fiji.

Live imaging of 2-cell embryos

For live imaging of 2-cell embryos, worms were dissected on glass coverslips in egg buffer and then mounted on 2% agar pads. Images were acquired every 1 minute or 20 seconds on a DeltaVision Personal DV microscope as described in the previous section; except that the distance between two planes was 2 μm. Mitotic timing was measured from NEBD to OCC as described in (Nelson *et al.*, 2015). Cell volumes were measured as described in (Galli and Morgan, 2016). To measure the nuclear area, a sum projection of the embryo was generated 1 minute before chromosomes began to condense and the area was measured with Fiji (Figure 14A).

Live imaging of embryogenesis

After treatment with *perm-1*^{RNAi} (see below), worms were dissected onto a coverslip with egg salt buffer (118 mM NaCl, 48 mM KCl) supplemented with 10 mM PIPES pH 7.3, 1 mM ATP and 10 mM sucrose. Embryos and adult carcasses were transferred into a well of an 8-well plate (ibidi 1 μ-Slide 8 Well Glass bottom) that had been freshly coated with 0.1% Poly-L-Lysine solution (Sigma P8920) and

extensively washed. Time-lapse videos were acquired with a Solamere spinning disk confocal system piloted by μManager software (Edelstein et al., 2014) and equipped with a Yokogawa CSUX-1 scan head, a Nikon (Garden City, NY) TE2000-E inverted stand, a Hamamatsu ImageEM ×2 camera, LX/MAS 489 nm and LS/MAS 561 nm laser, and Plan Apo ×60/1.4 numerical aperture oil objective. Acquisition times per frame were 50 ms using 5% of the lasers power for both channels, and images were obtained as stacks of planes at 2 μm intervals taken every 1 minute. Nocodazole was added from a 5X stock to a final concentration of 50 μM after the first time point. Mitotic timing was measured from NEBD to DECON as described in (Essex *et al.*, 2009).

To image embryogenesis in *zyg-1(or297)* mutants, images were generated under the same conditions as previously described for the live imaging of 2-cell embryos with a few modifications: Images were acquired every 20 seconds on a DeltaVision Personal DV microscope in a room heated to 26°C. Mitotic timing was measured from NEBD to DECON as described in (Essex *et al.*, 2009).

Quantification of fluorescence intensity

To quantify GFP::MAD-2 and PCH-2::GFP levels, images were generated under the same conditions as previously described for the live imaging of 2-cell embryos with a few modifications: only the area defined by the GFP cloud and mitotic chromosomes was imaged, the interval between the four planes was 1 μm and images were collected

every 20 seconds. Quantification of fluorescence at kinetochores was performed in Fiji as described in (Moyle et al., 2014; Nelson *et al.*, 2015). Briefly, maximum intensity projections of both mCh::H2B and GFP fusion proteins were made after the pseudo-metaphase plate was generated. The image was rotated so the metaphase plate was vertical, channels were split, and the maximum GFP pixel was identified using the process function within a box on the unattached side of the metaphase plate. In the same x-plane, the maximum mCh::H2B pixel was found. The width was changed to 12 pixels and the maximum GFP signal intensity was recorded in this 12 pixel window centered at the mCherry maxima. The background GFP signal was calculated by taking the average GFP intensity of a 4 pixel box in the same x-plane, 8 pixels away from the maximum mCherry on the opposite side of the pseudo-metaphase plate to the maximum GFP (i.e. the attached side). This background GFP was then subtracted from the maximum to measure the kinetochore bound GFP fusion intensity. Fluorescence around mitotic chromosomes was quantified as described in (Galli and Morgan, 2016). Sum intensity projections were generated and fluorescence in the area around mitotic chromosomes was measured in Fiji. Background fluorescence was measured in a 30 pixel band around this "cloud" and subtracted from the initial fluorescence intensity to determine the final fluorescence value. In some of our movies, identifying a clear metaphase plate was more difficult in AB than P_1 cells. Therefore, to ensure that we were quantifying PCH-2::GFP fluorescence around mitotic chromosomes at the same stage in mitosis in these two cell types, PCH-2::GFP was quantified in frames that were normalized relative to NEBD and

mitotic exit. To measure the cell volume, one Z-stack of the entire cell was taken at NEBD at 2 µm Z-spacing.

Feeding RNA interference (RNAi)

C. elegans strains were fed HT115 bacteria expressing the desired dsRNA after IPTG induction. Bacterial strains containing RNAi vectors were cultured overnight at 37°C, centrifuged, and the pellet was resuspended in 1/50 of the original volume. 100 µl of concentrated culture was spotted onto a nematode growth medium (NGM) plate containing 1 mM IPTG and 50 µg/µl of kanamycin or carbenicillin and the plate was incubated overnight at 37°C.

For *ani-2* RNAi, gravid adults were bleached onto the RNAi plate and their progeny was allowed to develop at 20°C during 2.5 days. Then, L4s were transferred to a fresh plate containing OP50 or *zyg-1* RNAi bacteria.

For *zyg-1* RNAi, L4s were transferred (from an OP50 or *ani-2* RNAi plate) onto a *zyg-1* RNAi plate and cultured 1.5 days at 20°C.

For *perm-1* RNAi, young adults (8h post L4) were incubated onto *perm-1* RNAi plates for 16-20 hours at 15°C.

For *par-1, par-6* and *gpr-1/2* RNAi, gravid adults were bleached onto control RNAi (L4440) plates and their progeny were allowed to develop at 15°C for 3 days. L4s were then transferred onto *par-1, par-6, gpr-1/2* RNAi or control RNAi plates and incubated at 15°C for 3 days. For *gpr-1/2* RNAi, "small" AB cells were identified by whether their area was at least one standard deviation lower than the average of control AB cells and "large" P_1 cells were identified by whether their area was at least one standard deviation higher than the average of control P_1 cells.

Statistical Analysis

All statistical analysis was performed using GraphPad Prism version 6 for Macintosh, including linear regression analysis and assessing significance of this data (Figures 9C, 11B, 13C, 17A, 17B, 23A, 10C, and 10D). For comparing two means, significance was assessed by performing two-tailed t-tests (Figures 18C, 19B, 19D, 20B, 20C, 20D, and 21A). In graphs in which multiple means were tested, we performed ANOVA analysis with the Sidak post-hoc test (Figures 9D, 17C, 18A, 18E, 23B, 23D, 16A, 22A, 22B, and 22D). In all graphs, a * indicates a p value < 0.05, ** indicates a p value < 0.01 and *** a p value < 0.0001.

Bibliography

Alfieri, C., Chang, L., and Barford, D. (2018). Mechanism for remodelling of the cell cycle checkpoint protein MAD2 by the ATPase TRIP13. Nature *559*, 274-278. 10.1038/s41586-018-0281-1.

Aravind, L., and Koonin, E.V. (1998). The HORMA domain: a common structural denominator in mitotic checkpoints, chromosome synapsis and DNA repair. Trends Biochem Sci *23*, 284-286.

Arribere, J.A., Bell, R.T., Fu, B.X., Artiles, K.L., Hartman, P.S., and Fire, A.Z. (2014). Efficient marker-free recovery of custom genetic modifications with CRISPR/Cas9 in Caenorhabditis elegans. Genetics *198*, 837-846. 10.1534/genetics.114.169730.

Bhalla, N., and Dernburg, A.F. (2005). A conserved checkpoint monitors meiotic chromosome synapsis in Caenorhabditis elegans. Science *310*, 1683-1686. 10.1126/science.1117468.

Bhalla, N., Wynne, D.J., Jantsch, V., and Dernburg, A.F. (2008). ZHP-3 acts at crossovers to couple meiotic recombination with synaptonemal complex disassembly and bivalent formation in C. elegans. PLoS Genet *4*, e1000235. 10.1371/journal.pgen.1000235.

Bohr, T., Nelson, C.R., Giacopazzi, S., Lamelza, P., and Bhalla, N. (2018). Shugoshin Is Essential for Meiotic Prophase Checkpoints in C. elegans. Curr Biol *28*, 3199-3211.e3193. 10.1016/j.cub.2018.08.026.

Bohr, T., Nelson, C.R., Klee, E., and Bhalla, N. (2015). Spindle assembly checkpoint proteins regulate and monitor meiotic synapsis in C. elegans. J Cell Biol *211*, 233-242. 10.1083/jcb.201409035.

Brenner, S. (1974). The genetics of Caenorhabditis elegans. Genetics *77*, 71-94.

Brulotte, M.L., Jeong, B.C., Li, F., Li, B., Yu, E.B., Wu, Q., Brautigam, C.A., Yu, H., and Luo, X. (2017). Mechanistic insight into TRIP13-catalyzed Mad2 structural transition and spindle checkpoint silencing. Nat Commun *8*, 1956. 10.1038/s41467-017-02012-2.

Börner, G.V., Barot, A., and Kleckner, N. (2008). Yeast Pch2 promotes domainal axis organization, timely recombination progression, and arrest of defective recombinosomes during meiosis. Proc Natl Acad Sci U S A *105*, 3327-3332. 10.1073/pnas.0711864105.

Carvalho, A., Olson, S.K., Gutierrez, E., Zhang, K., Noble, L.B., Zanin, E., Desai, A., Groisman, A., and Oegema, K. (2011). Acute drug treatment in the early C. elegans embryo. PLoS One *6*, e24656. 10.1371/journal.pone.0024656.

Caryl, A.P., Armstrong, S.J., Jones, G.H., and Franklin, F.C. (2000). A homologue of the yeast HOP1 gene is inactivated in the Arabidopsis meiotic mutant asy1. Chromosoma *109*, 62-71. 10.1007/s004120050413.

Chao, W.C., Kulkarni, K., Zhang, Z., Kong, E.H., and Barford, D. (2012). Structure of the mitotic checkpoint complex. Nature *484*, 208-213. 10.1038/nature10896.

Chen, C., Jomaa, A., Ortega, J., and Alani, E.E. (2014). Pch2 is a hexameric ring ATPase that remodels the chromosome axis protein Hop1. Proc Natl Acad Sci U S A *111*, E44-53. 10.1073/pnas.1310755111.

Chen, R.H., Shevchenko, A., Mann, M., and Murray, A.W. (1998). Spindle checkpoint protein Xmad1 recruits Xmad2 to unattached kinetochores. J Cell Biol *143*, 283-295.

Chen, R.H., Waters, J.C., Salmon, E.D., and Murray, A.W. (1996). Association of spindle assembly checkpoint component XMAD2 with unattached kinetochores. Science *274*, 242-246.

Chenevert, J., Roca, M., Besnardeau, L., Ruggiero, A., Nabi, D., McDougall, A., Copley, R.R., Christians, E., and Castagnetti, S. (2019). The spindle assembly checkpoint functions during early development in non-chordate embryos. bioRxiv. https://doi.org/10.1101/582759.

Cheng, C.H., Lo, Y.H., Liang, S.S., Ti, S.C., Lin, F.M., Yeh, C.H., Huang, H.Y., and Wang, T.F. (2006). SUMO modifications control assembly of synaptonemal complex and polycomplex in meiosis of Saccharomyces cerevisiae. Genes Dev *20*, 2067-2081. 10.1101/gad.1430406.

Collin, P., Nashchekina, O., Walker, R., and Pines, J. (2013). The spindle assembly checkpoint works like a rheostat rather than a toggle switch. Nat Cell Biol *15*, 1378-1385. 10.1038/ncb2855.

Colombo, K., Grill, S.W., Kimple, R.J., Willard, F.S., Siderovski, D.P., and Gonczy, P. (2003). Translation of polarity cues into asymmetric spindle positioning in Caenorhabditis elegans embryos. Science *300*, 1957-1961. 10.1126/science.1084146.

Couteau, F., and Zetka, M. (2005). HTP-1 coordinates synaptonemal complex assembly with homolog alignment during meiosis in C. elegans. Genes Dev *19*, 2744-2756. 10.1101/gad.1348205.

Couteau, F., and Zetka, M. (2011). DNA damage during meiosis induces chromatin remodeling and synaptonemal complex disassembly. Dev Cell *20*, 353-363. 10.1016/j.devcel.2011.01.015.

Date, D.A., Burrows, A.C., and Summers, M.K. (2014). Phosphorylation regulates the p31Comet-mitotic arrest-deficient 2 (Mad2) interaction to promote spindle assembly checkpoint (SAC) activity. J Biol Chem *289*, 11367-11373. 10.1074/jbc.M113.520841.

Davis, L.I., and Blobel, G. (1986). Identification and characterization of a nuclear pore complex protein. Cell *45*, 699-709. 10.1016/0092-8674(86)90784-1.

De Antoni, A., Pearson, C.G., Cimini, D., Canman, J.C., Sala, V., Nezi, L., Mapelli, M., Sironi, L., Faretta, M., Salmon, E.D., and Musacchio, A. (2005). The Mad1/Mad2 complex as a template for Mad2 activation in the spindle assembly checkpoint. Current biology : CB *15*, 214-225. 10.1016/j.cub.2005.01.038.

Dernburg, A.F., McDonald, K., Moulder, G., Barstead, R., Dresser, M., and Villeneuve, A.M. (1998). Meiotic recombination in C. elegans initiates by a conserved mechanism and is dispensable for homologous chromosome synapsis. Cell *94*, 387-398. 10.1016/s0092-8674(00)81481-6.

Deshong, A.J., Ye, A.L., Lamelza, P., and Bhalla, N. (2014). A quality control mechanism coordinates meiotic prophase events to promote crossover assurance. PLoS Genet *10*, e1004291. 10.1371/journal.pgen.1004291.

Dick, A.E., and Gerlich, D.W. (2013). Kinetic framework of spindle assembly checkpoint signalling. Nat Cell Biol *15*, 1370-1377. 10.1038/ncb2842.

Edelstein, A.D., Tsuchida, M.A., Amodaj, N., Pinkard, H., Vale, R.D., and Stuurman, N. (2014). Advanced methods of microscope control using muManager software. J Biol Methods *1*. 10.14440/jbm.2014.36.

Essex, A., Dammermann, A., Lewellyn, L., Oegema, K., and Desai, A. (2009). Systematic analysis in Caenorhabditis elegans reveals that the spindle checkpoint is composed of two largely independent branches. Mol Biol Cell *20*, 1252-1267. 10.1091/mbc.E08-10-1047.

Eytan, E., Wang, K., Miniowitz-Shemtov, S., Sitry-Shevah, D., Kaisari, S., Yen, T.J., Liu, S.T., and Hershko, A. (2014). Disassembly of mitotic checkpoint complexes by the joint action of the AAA-ATPase TRIP13 and p31(comet). Proc Natl Acad Sci U S A *111*, 12019-12024. 10.1073/pnas.1412901111.

Fava, L.L., Kaulich, M., Nigg, E.A., and Santamaria, A. (2011). Probing the in vivo function of Mad1:C-Mad2 in the spindle assembly checkpoint. EMBO J *30*, 3322-3336. 10.1038/emboj.2011.239.

Fukuda, T., Daniel, K., Wojtasz, L., Toth, A., and Höög, C. (2010). A novel mammalian HORMA domain-containing protein, HORMAD1, preferentially associates with unsynapsed meiotic chromosomes. Exp Cell Res *316*, 158-171. 10.1016/j.yexcr.2009.08.007.

Galli, M., and Morgan, D.O. (2016). Cell Size Determines the Strength of the Spindle Assembly Checkpoint during Embryonic Development. Dev Cell *36*, 344-352. 10.1016/j.devcel.2016.01.003.

Gerhold, A.R., Poupart, V., Labbe, J.C., and Maddox, P.S. (2018). Spindle assembly checkpoint strength is linked to cell fate in the Caenorhabditis elegans embryo. Mol Biol Cell *29*, 1435-1448. 10.1091/mbc.E18-04-0215.

Gerhold, A.R., Ryan, J., Vallee-Trudeau, J.N., Dorn, J.F., Labbe, J.C., and Maddox, P.S. (2015). Investigating the regulation of stem and progenitor cell mitotic progression by in situ imaging. Curr Biol *25*, 1123-1134. 10.1016/j.cub.2015.02.054.

Giacopazzi, S., Vong, D., Devigne, A., and Bhalla, N. (2020). PCH-2 collaborates with CMT-1 to proofread meiotic homolog interactions. PLoS Genet *16*, e1008904. 10.1371/journal.pgen.1008904.

Goldstein, B., and Macara, I.G. (2007). The PAR proteins: fundamental players in animal cell polarization. Dev Cell *13*, 609-622. 10.1016/j.devcel.2007.10.007.

Goodyer, W., Kaitna, S., Couteau, F., Ward, J.D., Boulton, S.J., and Zetka, M. (2008). HTP-3 links DSB formation with homolog pairing and crossing over during C. elegans meiosis. Dev Cell *14*, 263-274. 10.1016/j.devcel.2007.11.016.

Gotta, M., Dong, Y., Peterson, Y.K., Lanier, S.M., and Ahringer, J. (2003). Asymmetrically distributed C. elegans homologs of AGS3/PINS control spindle position in the early embryo. Curr Biol *13*, 1029-1037.

Guo, S., and Kemphues, K.J. (1995). par-1, a gene required for establishing polarity in C. elegans embryos, encodes a putative Ser/Thr kinase that is asymmetrically distributed. Cell *81*, 611-620. 10.1016/0092-8674(95)90082-9.

Hassold, T., and Hunt, P. (2001). To err (meiotically) is human: the genesis of human aneuploidy. Nat Rev Genet *2*, 280-291. 10.1038/35066065.

Hollingsworth, N.M., Goetsch, L., and Byers, B. (1990). The HOP1 gene encodes a meiosis-specific component of yeast chromosomes. Cell *61*, 73-84. 10.1016/0092-8674(90)90216-2.

Hung, T.J., and Kemphues, K.J. (1999). PAR-6 is a conserved PDZ domain-containing protein that colocalizes with PAR-3 in Caenorhabditis elegans embryos. Development *126*, 127-135.

Jantsch, V., Pasierbek, P., Mueller, M.M., Schweizer, D., Jantsch, M., and Loidl, J. (2004). Targeted gene knockout reveals a role in meiotic recombination for ZHP-3, a Zip3-related protein in Caenorhabditis elegans. Mol Cell Biol *24*, 7998-8006. 10.1128/MCB.24.18.7998-8006.2004.

Joshi, N., Barot, A., Jamison, C., and Börner, G.V. (2009). Pch2 links chromosome axis remodeling at future crossover sites and crossover distribution during yeast meiosis. PLoS Genet *5*, e1000557. 10.1371/journal.pgen.1000557.

Kim, D.H., Han, J.S., Ly, P., Ye, Q., McMahon, M.A., Myung, K., Corbett, K.D., and Cleveland, D.W. (2018). TRIP13 and APC15 drive mitotic exit by turnover of interphase- and unattached kinetochore-produced MCC. Nat Commun *9*, 4354. 10.1038/s41467-018-06774-1.

Kim, Y., Kostow, N., and Dernburg, A.F. (2015). The Chromosome Axis Mediates Feedback Control of CHK-2 to Ensure Crossover Formation in C. elegans. Dev Cell *35*, 247-261. 10.1016/j.devcel.2015.09.021.

Kim, Y., Rosenberg, S.C., Kugel, C.L., Kostow, N., Rog, O., Davydov, V., Su, T.Y., Dernburg, A.F., and Corbett, K.D. (2014). The chromosome axis controls meiotic events through a hierarchical assembly of HORMA domain proteins. Dev Cell *31*, 487-502. 10.1016/j.devcel.2014.09.013.

Kitagawa, R., and Rose, A.M. (1999). Components of the spindle-assembly checkpoint are essential in Caenorhabditis elegans. Nat Cell Biol *1*, 514-521. 10.1038/70309.

Kyogoku, H., and Kitajima, T.S. (2017). Large Cytoplasm Is Linked to the Error-Prone Nature of Oocytes. Dev Cell *41*, 287-298 e284. 10.1016/j.devcel.2017.04.009.

Lambing, C., Osman, K., Nuntasoontorn, K., West, A., Higgins, J.D., Copenhaver, G.P., Yang, J., Armstrong, S.J., Mechtler, K., Roitinger, E., and Franklin, F.C. (2015). Arabidopsis PCH2 Mediates Meiotic Chromosome Remodeling and Maturation of Crossovers. PLoS Genet *11*, e1005372. 10.1371/journal.pgen.1005372.

Lara-Gonzalez, P., Moyle, M.W., Budrewicz, J., Mendoza-Lopez, J., Oegema, K., and Desai, A. (2019). The G2-to-M Transition Is Ensured by a Dual Mechanism that Protects Cyclin B from Degradation by Cdc20-Activated APC/C. Dev Cell *51*, 313-325 e310. 10.1016/j.devcel.2019.09.005.

Lawrence, K.S., Chau, T., and Engebrecht, J. (2015). DNA damage response and spindle assembly checkpoint function throughout the cell cycle to ensure genomic integrity. PLoS Genet *11*, e1005150. 10.1371/journal.pgen.1005150.

Li, Y., and Benezra, R. (1996). Identification of a human mitotic checkpoint gene: hsMAD2. Science *274*, 246-248. 10.1126/science.274.5285.246.

Lorenz, A., Wells, J.L., Pryce, D.W., Novatchkova, M., Eisenhaber, F., McFarlane, R.J., and Loidl, J. (2004). S. pombe meiotic linear elements contain proteins related to synaptonemal complex components. J Cell Sci *117*, 3343-3351. 10.1242/jcs.01203.

Luo, X., Tang, Z., Rizo, J., and Yu, H. (2002). The Mad2 spindle checkpoint protein undergoes similar major conformational changes upon binding to either Mad1 or Cdc20. Mol Cell *9*, 59-71.

Luo, X., Tang, Z., Xia, G., Wassmann, K., Matsumoto, T., Rizo, J., and Yu, H. (2004). The Mad2 spindle checkpoint protein has two distinct natively folded states. Nat Struct Mol Biol *11*, 338-345. 10.1038/nsmb748.

Ma, H.T., and Poon, R.Y. (2016). TRIP13 Regulates Both the Activation and Inactivation of the Spindle-Assembly Checkpoint. Cell Rep *14*, 1086-1099. 10.1016/j.celrep.2016.01.001.

Ma, H.T., and Poon, R.Y.C. (2018). TRIP13 Functions in the Establishment of the Spindle Assembly Checkpoint by Replenishing O-MAD2. Cell Rep *22*, 1439-1450. 10.1016/j.celrep.2018.01.027.

MacQueen, A.J., Colaiácovo, M.P., McDonald, K., and Villeneuve, A.M. (2002). Synapsis-dependent and -independent mechanisms stabilize homolog pairing during meiotic prophase in C. elegans. Genes Dev *16*, 2428-2442. 10.1101/gad.1011602.

MacQueen, A.J., Phillips, C.M., Bhalla, N., Weiser, P., Villeneuve, A.M., and Dernburg, A.F. (2005). Chromosome sites play dual roles to establish homologous synapsis during meiosis in C. elegans. Cell *123*, 1037-1050. 10.1016/j.cell.2005.09.034.

Maddox, A.S., Habermann, B., Desai, A., and Oegema, K. (2005). Distinct roles for two C. elegans anillins in the gonad and early embryo. Development *132*, 2837-2848. 10.1242/dev.01828.

Mariani, L., Chiroli, E., Nezi, L., Muller, H., Piatti, S., Musacchio, A., and Ciliberto, A. (2012). Role of the Mad2 dimerization interface in the spindle assembly checkpoint independent of kinetochores. Curr Biol *22*, 1900-1908. 10.1016/j.cub.2012.08.028.

Marks, D.H., Thomas, R., Chin, Y., Shah, R., Khoo, C., and Benezra, R. (2017). Mad2 Overexpression Uncovers a Critical Role for TRIP13 in Mitotic Exit. Cell Rep *19*, 1832-1845. 10.1016/j.celrep.2017.05.021.

Martinez-Perez, E., Schvarzstein, M., Barroso, C., Lightfoot, J., Dernburg, A.F., and Villeneuve, A.M. (2008). Crossovers trigger a remodeling of meiotic chromosome axis composition that is linked to two-step loss of sister chromatid cohesion. Genes Dev *22*, 2886-2901. 10.1101/gad.1694108.

Martinez-Perez, E., and Villeneuve, A.M. (2005). HTP-1-dependent constraints coordinate homolog pairing and synapsis and promote chiasma formation during C. elegans meiosis. Genes Dev *19*, 2727-2743. 10.1101/gad.1338505.

McKim, K.S., Green-Marroquin, B.L., Sekelsky, J.J., Chin, G., Steinberg, C., Khodosh, R., and Hawley, R.S. (1998). Meiotic synapsis in the absence of recombination. Science *279*, 876-878. 10.1126/science.279.5352.876.

Meraldi, P., Draviam, V.M., and Sorger, P.K. (2004). Timing and checkpoints in the regulation of mitotic progression. Dev Cell *7*, 45-60. 10.1016/j.devcel.2004.06.006.

Miniowitz-Shemtov, S., Eytan, E., Kaisari, S., Sitry-Shevah, D., and Hershko, A. (2015). Mode of interaction of TRIP13 AAA-ATPase with the Mad2-binding protein p31comet and with mitotic checkpoint complexes. Proc Natl Acad Sci U S A *112*, 11536-11540. 10.1073/pnas.1515358112.

Moyle, M.W., Kim, T., Hattersley, N., Espeut, J., Cheerambathur, D.K., Oegema, K., and Desai, A. (2014). A Bub1-Mad1 interaction targets the Mad1-Mad2 complex to unattached kinetochores to initiate the spindle checkpoint. J Cell Biol *204*, 647-657. 10.1083/jcb.201311015.

Nadarajan, S., Lambert, T.J., Altendorfer, E., Gao, J., Blower, M.D., Waters, J.C., and Colaiácovo, M.P. (2017). Polo-like kinase-dependent phosphorylation of the

synaptonemal complex protein SYP-4 regulates double-strand break formation through a negative feedback loop. Elife *6*. 10.7554/eLife.23437.

Nelson, C.R., Hwang, T., Chen, P.H., and Bhalla, N. (2015). TRIP13PCH-2 promotes Mad2 localization to unattached kinetochores in the spindle checkpoint response. J Cell Biol *211*, 503-516. 10.1083/jcb.201505114.

Nezi, L., Rancati, G., De Antoni, A., Pasqualato, S., Piatti, S., and Musacchio, A. (2006). Accumulation of Mad2-Cdc20 complex during spindle checkpoint activation requires binding of open and closed conformers of Mad2 in Saccharomyces cerevisiae. J Cell Biol *174*, 39-51. 10.1083/jcb.200602109.

Nguyen, H., Labella, S., Silva, N., Jantsch, V., and Zetka, M. (2018). C. elegans ZHP-4 is required at multiple distinct steps in the formation of crossovers and their transition to segregation competent chiasmata. PLoS Genet *14*, e1007776. 10.1371/journal.pgen.1007776.

Nystul, T.G., Goldmark, J.P., Padilla, P.A., and Roth, M.B. (2003). Suspended animation in C. elegans requires the spindle checkpoint. Science *302*, 1038-1041. 10.1126/science.1089705.

O'Connell, K.F., Caron, C., Kopish, K.R., Hurd, D.D., Kemphues, K.J., Li, Y., and White, J.G. (2001). The C. elegans zyg-1 gene encodes a regulator of centrosome duplication with distinct maternal and paternal roles in the embryo. Cell *105*, 547-558.

O'Rourke, S.M., Carter, C., Carter, L., Christensen, S.N., Jones, M.P., Nash, B., Price, M.H., Turnbull, D.W., Garner, A.R., Hamill, D.R., et al. (2011). A survey of new temperature-sensitive, embryonic-lethal mutations in C. elegans: 24 alleles of thirteen genes. PLoS One *6*, e16644. 10.1371/journal.pone.0016644.

Page, S.L., and Hawley, R.S. (2003). Chromosome choreography: the meiotic ballet. Science *301*, 785-789. 10.1126/science.1086605.

Paix, A., Folkmann, A., Rasoloson, D., and Seydoux, G. (2015). High Efficiency, Homology-Directed Genome Editing in Caenorhabditis elegans Using CRISPR-Cas9 Ribonucleoprotein Complexes. Genetics *201*, 47-54. 10.1534/genetics.115.179382.

Phillips, C.M., Wong, C., Bhalla, N., Carlton, P.M., Weiser, P., Meneely, P.M., and Dernburg, A.F. (2005). HIM-8 binds to the X chromosome pairing center and mediates chromosome-specific meiotic synapsis. Cell *123*, 1051-1063. 10.1016/j.cell.2005.09.035.

Raina, V.B., and Vader, G. (2020). Homeostatic Control of Meiotic Prophase Checkpoint Function by Pch2 and Hop1. Curr Biol *30*, 4413-4424.e4415. 10.1016/j.cub.2020.08.064.

Reynolds, A., Qiao, H., Yang, Y., Chen, J.K., Jackson, N., Biswas, K., Holloway, J.K., Baudat, F., de Massy, B., Wang, J., et al. (2013). RNF212 is a dosage-sensitive regulator of crossing-over during mammalian meiosis. Nat Genet *45*, 269-278. 10.1038/ng.2541.

Rodriguez-Bravo, V., Maciejowski, J., Corona, J., Buch, H.K., Collin, P., Kanemaki, M.T., Shah, J.V., and Jallepalli, P.V. (2014). Nuclear pores protect genome integrity by assembling a premitotic and Mad1-dependent anaphase inhibitor. Cell *156*, 1017-1031. 10.1016/j.cell.2014.01.010.

Rose, L., and Gonczy, P. (2014). Polarity establishment, asymmetric division and segregation of fate determinants in early C. elegans embryos. WormBook, 1-43. 10.1895/wormbook.1.30.2.

Rosenberg, S.C., and Corbett, K.D. (2015). The multifaceted roles of the HORMA domain in cellular signaling. J Cell Biol *211*, 745-755. 10.1083/jcb.201509076.

San-Segundo, P.A., and Roeder, G.S. (1999). Pch2 links chromatin silencing to meiotic checkpoint control. Cell *97*, 313-324.

Sato-Carlton, A., Nakamura-Tabuchi, C., Chartrand, S.K., Uchino, T., and Carlton, P.M. (2018). Phosphorylation of the synaptonemal complex protein SYP-1 promotes meiotic chromosome segregation. J Cell Biol *217*, 555-570. 10.1083/jcb.201707161.

Seydoux, G., Mello, C.C., Pettitt, J., Wood, W.B., Priess, J.R., and Fire, A. (1996). Repression of gene expression in the embryonic germ lineage of C. elegans. Nature *382*, 713-716. 10.1038/382713a0.

Silva, N., Ferrandiz, N., Barroso, C., Tognetti, S., Lightfoot, J., Telecan, O., Encheva, V., Faull, P., Hanni, S., Furger, A., et al. (2014). The fidelity of synaptonemal complex assembly is regulated by a signaling mechanism that controls early meiotic progression. Dev Cell *31*, 503-511. 10.1016/j.devcel.2014.10.001.

Simonetta, M., Manzoni, R., Mosca, R., Mapelli, M., Massimiliano, L., Vink, M., Novak, B., Musacchio, A., and Ciliberto, A. (2009). The influence of catalysis on mad2 activation dynamics. PLoS Biol *7*, e10. 10.1371/journal.pbio.1000010.

Sironi, L., Mapelli, M., Knapp, S., De Antoni, A., Jeang, K.T., and Musacchio, A. (2002). Crystal structure of the tetrameric Mad1-Mad2 core complex: implications of a 'safety belt' binding mechanism for the spindle checkpoint. EMBO J *21*, 2496-2506. 10.1093/emboj/21.10.2496.

Sironi, L., Melixetian, M., Faretta, M., Prosperini, E., Helin, K., and Musacchio, A. (2001). Mad2 binding to Mad1 and Cdc20, rather than oligomerization, is required for the spindle checkpoint. EMBO J *20*, 6371-6382. 10.1093/emboj/20.22.6371.

Srinivasan, D.G., Fisk, R.M., Xu, H., and van den Heuvel, S. (2003). A complex of LIN-5 and GPR proteins regulates G protein signaling and spindle function in C elegans. Genes Dev *17*, 1225-1239. 10.1101/gad.1081203.

Stamper, E.L., Rodenbusch, S.E., Rosu, S., Ahringer, J., Villeneuve, A.M., and Dernburg, A.F. (2013). Identification of DSB-1, a protein required for initiation of meiotic recombination in Caenorhabditis elegans, illuminates a crossover assurance checkpoint. PLoS Genet *9*, e1003679. 10.1371/journal.pgen.1003679.

Stein, K.K., Davis, E.S., Hays, T., and Golden, A. (2007). Components of the spindle assembly checkpoint regulate the anaphase-promoting complex during meiosis in Caenorhabditis elegans. Genetics *175*, 107-123. 10.1534/genetics.106.059105.

Sudakin, V., Chan, G.K., and Yen, T.J. (2001). Checkpoint inhibition of the APC/C in HeLa cells is mediated by a complex of BUBR1, BUB3, CDC20, and MAD2. J Cell Biol *154*, 925-936. 10.1083/jcb.200102093.

Tintori, S.C., Osborne Nishimura, E., Golden, P., Lieb, J.D., and Goldstein, B. (2016). A Transcriptional Lineage of the Early C. elegans Embryo. Dev Cell *38*, 430-444. 10.1016/j.devcel.2016.07.025.

Tipton, A.R., Wang, K., Oladimeji, P., Sufi, S., Gu, Z., and Liu, S.T. (2012). Identification of novel mitosis regulators through data mining with human centromere/kinetochore proteins as group queries. BMC Cell Biol *13*, 15. 10.1186/1471-2121-13-15.

Vader, G. (2015). Pch2(TRIP13): controlling cell division through regulation of HORMA domains. Chromosoma *124*, 333-339. 10.1007/s00412-015-0516-y.

van Hooff, J.J., Tromer, E., van Wijk, L.M., Snel, B., and Kops, G.J. (2017). Evolutionary dynamics of the kinetochore network in eukaryotes as revealed by comparative genomics. EMBO Rep. 10.15252/embr.201744102.

Vazquez-Diez, C., Paim, L.M.G., and FitzHarris, G. (2019). Cell-Size-Independent Spindle Checkpoint Failure Underlies Chromosome Segregation Error in Mouse Embryos. Curr Biol *29*, 865-873 e863. 10.1016/j.cub.2018.12.042.

Vleugel, M., Hoogendoorn, E., Snel, B., and Kops, G.J. (2012). Evolution and function of the mitotic checkpoint. Dev Cell *23*, 239-250. 10.1016/j.devcel.2012.06.013.

Wang, K., Sturt-Gillespie, B., Hittle, J.C., Macdonald, D., Chan, G.K., Yen, T.J., and Liu, S.T. (2014). Thyroid hormone receptor interacting protein 13 (TRIP13) AAA-ATPase is a novel mitotic checkpoint-silencing protein. J Biol Chem *289*, 23928-23937. 10.1074/jbc.M114.585315.

Wickham, H. (2016). ggplot2: Elegant Graphics for Data Analysis. Springer-Verlag.

Woglar, A., Daryabeigi, A., Adamo, A., Habacher, C., Machacek, T., La Volpe, A., and Jantsch, V. (2013). Matefin/SUN-1 phosphorylation is part of a surveillance mechanism to coordinate chromosome synapsis and recombination with meiotic progression and chromosome movement. PLoS Genet *9*, e1003335. 10.1371/journal.pgen.1003335.

Wojtasz, L., Daniel, K., Roig, I., Bolcun-Filas, E., Xu, H., Boonsanay, V., Eckmann, C.R., Cooke, H.J., Jasin, M., Keeney, S., et al. (2009). Mouse HORMAD1 and HORMAD2, two conserved meiotic chromosomal proteins, are depleted from synapsed chromosome axes with the help of TRIP13 AAA-ATPase. PLoS Genet *5*, e1000702. 10.1371/journal.pgen.1000702.

Wu, H.Y., and Burgess, S.M. (2006). Two distinct surveillance mechanisms monitor meiotic chromosome metabolism in budding yeast. Curr Biol *16*, 2473-2479. 10.1016/j.cub.2006.10.069.

Xia, G., Luo, X., Habu, T., Rizo, J., Matsumoto, T., and Yu, H. (2004). Conformation-specific binding of p31(comet) antagonizes the function of Mad2 in the spindle checkpoint. EMBO J *23*, 3133-3143. 10.1038/sj.emboj.7600322.

Ye, Q., Rosenberg, S.C., Moeller, A., Speir, J.A., Su, T.Y., and Corbett, K.D. (2015). TRIP13 is a protein-remodeling AAA+ ATPase that catalyzes MAD2 conformation switching. eLife *4*. 10.7554/eLife.07367.

Yokoo, R., Zawadzki, K.A., Nabeshima, K., Drake, M., Arur, S., and Villeneuve, A.M. (2012). COSA-1 reveals robust homeostasis and separable licensing and reinforcement steps governing meiotic crossovers. Cell *149*, 75-87. 10.1016/j.cell.2012.01.052.

Yost, S., de Wolf, B., Hanks, S., Zachariou, A., Marcozzi, C., Clarke, M., de Voer, R.M., Etemad, B., Uijttewaal, E., Ramsay, E., et al. (2017). Biallelic TRIP13 mutations predispose to Wilms tumor and chromosome missegregation. Nat Genet. 10.1038/ng.3883.

Zetka, M.C., Kawasaki, I., Strome, S., and Müller, F. (1999). Synapsis and chiasma formation in Caenorhabditis elegans require HIM-3, a meiotic chromosome core component that functions in chromosome segregation. Genes Dev *13*, 2258-2270. 10.1101/gad.13.17.2258.

Zhang, L., Köhler, S., Rillo-Bohn, R., and Dernburg, A.F. (2018). A compartmentalized signaling network mediates crossover control in meiosis. Elife *7*. 10.7554/eLife.30789.